2015

# Exploring Superconductivity in Chiral Structured AuBe

Drew Jared Rebar
*Louisiana State University and Agricultural and Mechanical College*, drebar1@lsu.edu

# EXPLORING SUPERCONDUCTIVITY IN CHIRAL STRUCTURED AUBE

A Dissertation

Submitted to the Graduate Faculty of the
Louisiana State University and
Agricultural and Mechanical College
in partial fulfillment of the
requirements for the degree of
Doctor of Philosophy

in

The Department of Physics and Astronomy

by
Drew Jared Rebar
B.S., Bob Jones University, 2004
M.S., University of South Florida, 2006
December 2015

To Mom and Dad, with love

## Acknowledgements

My journey through graduate school has been in the company of mentors, collaborators, and friends. As this journey comes to a close, I would like to acknowledge and express gratitude to the following people and groups. First, I must acknowledge the work of Jesus Christ in my life. When I came to the end of myself, I found hope, purpose, and the will to continue in Him. May any excellence in my work be to His glory. Next, I must thank my parents for their love and encouragement along this journey in graduate school and all times previous. The dedication of this dissertation to you is but a small return on your very large investment in my life. Next, I thank my advisor, Dr. John F. DiTusa, for his mentorship, guidance, patience, and funding for my time at LSU. I would also like to thank my dissertation committee consisting of my advisor, Dr. Philip Adams, Dr. Dana Browne, Dr. Philip Sprunger, Dr. Jon Dowling, Dr. Hwang Lee, and Dr. William Adkins. Thank you for all your support, patience, and guidance. It has all been very much appreciated! I must express much gratitude to the following group of collaborators. I thank Dr. Philip Adams for discussion of many questions, providing specific heat measurements, providing Cr deposition along with resistivity measurements, etc. With Dr. Adams, I thank the members of his group who assisted which include Dr. Joseph Prestigiacomo and Dr. Abhishek Pandey. I thank Dr. Julia Chan who performed powder XRD on my samples. I also thank Dr. Chan for counsel and encouragement during some difficult times of graduate school. I thank Dr. David Young for his help with synthesis and access to his equipment. With Dr. Young, I thank his student Mojammel Khan for assistance in the lab. I thank Dr. Dana Browne for band structure calculations and Fermi surface renderings. With Dr. Browne, I thank his student Jordan Ball for assistance in performing the calculations. I thank Dr. Ilya Vekhter for his insight and input on the theory side of this project.

Many thanks go to Dr. John Singleton of the National High Magnetic Field Laboratory at Los Alamos National Laboratory for the opportunity to characterize AuBe at Los Alamos which included his help, time, and financial support. With Dr. Singleton, I thank Dr. Brian Scott who provided a quick single-crystal characterization, Dr. Vivien Zapf who assisted with measurements when Dr. Singleton had to be away, and a number of postdocs and other staff members who helped at random times and answered many questions. Next, I would like to express gratitude for a number of people who have provided assistance with this project. From the lab of Dr. Shane Stadler, I thank Dr. Tapas Samanta for help with the arc-melter and Ahmad Us Saleheen for quick powder XRD measurements. I thank Dr. Rongying Jin and her student Zhenyu Diao for their time and expertise in their attempt at AuBe single crystal synthesis with their floating zone furnace. From the LSU Shared Instrumentation Facility, I thank Dr. Dongmei Cao for training and assistance with the FIB/SEM, Dr. Hollie Hale-Donze for training and assistance with the confocal microscope and other optical microscopes, and Dr. Clayton Loehn for access to the facility. From the LSU Center for Advanced Microstructures and Devices, I thank Dr. Varshni Singh for access and assistance with various equipment including the SEM. From the LSU School of Veterinary Medicine, I thank Dr. Xiaochu Wu for access to the Vet School's confocal microscope. From the LSU Geology Department, I thank Dr. Xiaogang Xie for access and training on their SEM. From the LSU Physics Electronic Shop, I thank Randy Gould, Brad Ellison, and Marcus Nauman for assistance with numerous projects, training on electronics assembly, and answers to numerous questions. From the LSU Machine Shop, I thank Brandon Amos, Vincent Vaughn, Donnie Olano, and George Gascon for machine work on numerous projects and insight on proper design for machining. From the LSU Chemistry Department, I thank Dr. Evgueni Nesterov and his graduate

students for access, help, and use of their lab on a different research project. I thank my lab mates for random help around the lab which include Jessica Hebert and Yan Wu. I also thank the many past lab mates for random help around the lab particularly Josh Mendez Plaskus for his efforts in construction of a shutter mechanism for the thermal metal evaporator. In this list of acknowledgements, I certainly cannot leave off gratitude to the LSU physics office staff whose efforts have allowed my efforts to continue unhindered. I am particularly grateful to Arnell Nelson, Shemeka Law, and Ophelia Dudley who have performed much behind-the-scenes work with forms, purchasing, travel, etc. This long list of people is certainly not exhaustive, and I express my gratitude and apologies to any who might have been missed. To conclude this section, I acknowledge and am grateful for funding received from the National Science Foundation (NSF) and the Louisiana Alliance for Simulation-Guided Materials Applications (LA-SiGMA).

# Table of Contents

## Abstract

AuBe is a noncentrosymmetric superconductor with the *B20* FeSi-type structure. Noncentrosymmetric superconductors are expected to give rise to unconventional superconductivity due to spin orbit coupling and a mixed spin-singlet, spin-triplet state. The *B20* structure of AuBe is particularly interesting since this is one of the only known crystal structures for bulk magnetic skyrmions in materials such as MnSi and $Cu_2OSeO_3$. The superconducting state was characterized by specific heat, dc magnetization, ac susceptibility, and resistivity. Specific heat revealed AuBe to host an isotropic gap characteristic of predominantly *s*-wave spin-singlet pairing in the weak coupling limit. Magnetization and susceptibility measurements revealed a critical temperature of 3.2 K and a crossover from Type I to Type II superconductivity at approximately 1.2 K. Resistivity characterization of the superconducting transition revealed significantly higher critical fields at lower temperature. The robust critical fields as measured in the resistivity are attributed to either a surface superconducting state that is robust against the deposition of magnetic thin films, or a filamentary superconductivity at twin boundaries enhanced by spin orbit coupling.

# Chapter 1: Introduction to Noncentrosymmetric Superconductors and AuBe

## 1.1 Introduction

Does AuBe exhibit novel superconductivity? The investigation of this question is the topic of this dissertation and represents a small part of a broader effort to explore and understand unconventional mechanisms of superconductivity. This chapter provides definition and qualification of the proposed question and our motivation for pursuing this line of research. Section 1.2 gives definition for what it means to be a superconductor. Section 1.3 discusses the meaning of "novel" with context to our investigation and describes specific phenomena to be used as a metric for novel superconductivity. Section 1.4 ends the chapter with background information on AuBe and discussion of our motivation for studying this material.

## 1.2 Superconductivity

The superconducting state was discovered in 1911 by Kamerlingh Onnes after he discovered how to liquefy helium[1]. The onset of the superconducting state begins at a critical temperature, $T_c$, wherein a pairing attraction between conduction electrons forms bosonic particles termed Cooper pairs. This radical transformation of the electronic behavior gives a material the extraordinary qualities of zero resistance (hence the name superconductivity) and perfect diamagnetism termed the Meissner effect [2]. In the paragraphs to follow, these qualities of superconductivity will be discussed in further detail.

The onset of zero resistance at the superconducting transition implies a drastic change in the electronic structure of a material since elastic and inelastic scattering mechanisms no longer impede the propagation of electrons. Thus in the superconducting state, Ohm's Law, V = IR, no

longer applies and new equations describing electron motion are needed. One of these new equations, published by F. and H. London in 1935 [3], is the following:

$$\vec{E} = \frac{\partial}{\partial t}(\Lambda \vec{J}_s).$$

$J_s$ is the current density in the superconducting state, and the phenomenological parameter, $\Lambda$, is described as follows:

$$\Lambda = \frac{4\pi\lambda^2}{c^2} = \frac{m}{n_s e^2}.$$

m is the effective electron mass, $n_s$ is the electron density in the superconducting state, and $\lambda$ is a characteristic length. This first London equation describes the departure from Ohm's Law in that an applied electric field accelerates charge with no dissipation in the response [2].

The onset of perfect diamagnetism termed the Meissner effect at the critical temperature, $T_c$, means that a superconductor acquires a magnetic response that is equal and opposite to an applied magnetic field ($\chi$ = -1 in SI units). While a temperature higher than $T_c$ will terminate the superconducting state, a critical value of field, $H_c$, achieves the same effect. One of the earliest treatments of applied field was the second London equation describing the relationship of applied magnetic field and current density. This equation is the following with $\Lambda$ defined from the last paragraph:

$$\vec{h} = -c\boldsymbol{\nabla} \times \Lambda \vec{J}_s.$$

**h** is defined as the microscopic flux density. This second equation requires further refinement for understanding its purpose, and it requires a definition of $\lambda$. The current density, $\mathbf{J}_s$ can be

substituted with a Maxwell formula, and the second London equation can be rewritten in terms of **h** alone. This Maxwell equation and the rewritten second London equation are as follows, respectively:

$$\boldsymbol{\nabla} \times \vec{h} = \frac{4\pi}{c}\vec{J},$$

$$\nabla^2\vec{h} = \frac{1}{\lambda^2}\vec{h}.$$

The solution for **h** is an exponential function giving the picture that applied magnetic field decays quickly upon penetration of the superconductor surface with characteristic decay length, $\lambda$, termed the penetration depth. The penetration depth, $\lambda$, defined from the above definition for $\Lambda$ is the following:

$$\lambda_L = \sqrt{\frac{mc^2}{4\pi n_s e^2}}.$$

The subscript, L, denotes this definition for penetration depth as originating from the London equations. Later definitions for the penetration depth incorporated temperature dependence [2]. One of the more prevalent definitions came from the theory of Gorter and Casimir [4] who treated the superconducting state as a two-fluid model of normal and superconducting electrons. Their definition is as follows:

$$\lambda(T) \approx \lambda(0)[1 - (T/T_c)]^4.$$

While the Meissner effect in superconductors gives it the quality of a perfect diamagnetic material, the Meissner effect cannot entirely be defined in terms of a perfect conductor.

Examination of the superconducting transition in heat capacity highlights this difference. When an applied magnetic field is present, the heat capacity reveals a first order transition with characteristic latent heat at the superconducting transition. In the absence of any applied field, a superconductor still exhibits the Meissner effect at $T_c$ but instead displays a second order transition. Figure 1.1 displays a drawing of the superconducting transition at zero magnetic field as measured by heat capacity. The landmark theory of Bardeen, Cooper, and Schrieffer (BCS theory) describes universal behavior of the transition and form for the superconducting state. First, the ratio of the jump in heat capacity at the transition to the heat capacity in the normal state above the transition is given as $\Delta C/C_{en} = 1.43$. A smaller value of the ratio could indicate that the sample was not completely superconducting while a larger value could indicate a departure from the weak-coupling approximation assumed in BCS theory. Second, the form of the curve below $T_c$ follows an exponential function, $C_{es} \sim e^{-\Delta/k_B T}$. This activated form of the heat capacity in BCS theory arises from the energy gap that opens across the Fermi surface. BCS theory defines the gap as $E_g$(T=0 K) = $2\Delta$(T = 0) = $3.528 k_B T_c$ which is the energy required to separate the paired conduction electrons [2,5]. A last thermodynamic relationship to be considered is the energy saving of the superconducting state calculated in BCS theory. Again, the weak-coupling approximation in

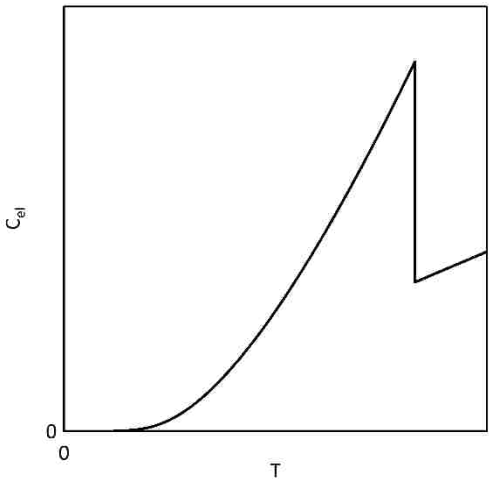


Figure 1.1: BCS form of the superconducting transition observed in electron heat capacity.

addition to the BCS ground state wavefunction was used to determine the following difference in internal energy, U(T):

$$U_s(0) - U_n(0) = -\frac{1}{2}N(0)\Delta^2(0).$$

N(0) is the density of states per unit energy at the Fermi level and Δ is defined above from BCS theory. When considering the difference in free energy from the change in magnetic state due to perfect diamagnetism ($\chi = -1/4\pi$, cgs units), the following relation can be defined:

$$F_{en}(T) - F_{es}(T) = \frac{H_c^2}{8\pi}.$$

The subscripts *es* and *en* refer to the electronic contributions to free energy in the superconducting and normal states, respectively. $H_c$ is defined as the thermodynamic critical field. When combining the expressions for energy difference from BCS theory and the thermodynamic treatment of the Meissner effect (perfect diamagnetism), the following equation relates the critical values for field and temperature allowing for an estimate for the critical field at zero temperature from measurement of the critical temperature:

$$\frac{H_c^2(0)}{8\pi} = \frac{1}{2}N(0)\Delta^2(0) = \frac{1}{2}N(0)[1.764T_c]^2.$$

Implicit to this formula are the assumptions that the superconducting state is entirely an electronic phenomena and that the perfect diamagnetism of the Meissner effect is the expression of the superconducting state [2,6].

Discussion of the Meissner effect revealed a characteristic length, λ, which was defined as the penetration depth of applied field at the surface of a superconductor. Discrepancy

between the London penetration depth and measurements of penetration depth in doped elemental superconductors led Pippard to deduce another characteristic length which he described as the distance over which electrons experienced an interaction giving them coherent behavior. His estimate for this coherence length was the following:

$$\xi_o = a\frac{\hbar v_F}{k_B T_c}.$$

$v_F$ is the Fermi velocity, and *a* is a proportionality constant Pippard determined to be 0.15 and BCS theory later set at 0.18. In related work, Ginzburg and Landau (GL) defined a coherence length, $\xi(T)$, based on the spatial variation of the order parameter, $\psi(r)$, used in their theory to determine the superconducting electron density, $n_s$. The relationship of the GL coherence length to the Pippard (and BCS) coherence length, $\xi_o$, is given as follows:

$$\xi(T) = 0.74\frac{\xi_o}{\sqrt{1 - T/T_c}}.$$

This formula describes the coherence length in the limit for no disorder. Ginzburg and Landau also defined a dimensionless parameter, $\kappa$, used for comparison and categorization of superconductors. This parameter is given as follows:

$$\kappa = 0.96\frac{\lambda_L(0)}{\xi_o}.$$

This GL parameter is typically defined simply as $\kappa = \lambda/\xi$ and as previously for $\xi$, is defined in the pure limit [2]. The categorization of superconductors by $\kappa$ and the description of the categories is to be discussed next.

The theoretical description of two types of superconductors was achieved by Abrikosov [7] in 1957 with his extension of GL theory. The types of superconductors are divided into categories defined by the sign of their surface energy. The GL parameter, $\kappa$, serves as a measure of the surface energy sign with positive surface energy corresponding to $\kappa < 1/\sqrt{2}$ and negative surface energy corresponding to $\kappa > 1/\sqrt{2}$. Superconductors with positive surface energy are called Type I superconductors while those with negative surface energy are called Type II superconductors. Type I superconductors possess the qualities of superconductivity as discussed above. The positive surface energy influences the entrance or exit of magnetic flux at the surface with sharp transitions and hysteresis termed supercooling. Type II superconductors possess modifications of the superconducting qualities presented in this section. The negative surface energy allows the inclusion of magnetic flux in the superconducting state by the formation of vortices with circulating Cooper pairs surrounding electrons in the normal state. Motion of the vortices gives rise to resistance in the superconducting state which is minimized by pinning. Incorporation of field partially destroys the Meissner effect. Thus while Type I superconductors possess a sharp first order transition into the superconducting state with decreasing magnetic field, Type II superconductors possess a second order transition which includes a mixed state consisting of superconducting and normal domains. The mixed state of Type II superconductors is defined by two critical fields with the upper critical field, $H_{c2}$, describing the onset of superconductivity with decreasing magnetic field and a lower critical field, $H_{c1}$, describing the onset of a full Meissner effect. The superconducting transition is broader and characteristically has no hysteresis consistent with the nature of the second order transition. The upper critical field, $H_{c2}$, is defined in GL theory as the following:

$$H_{c2} = \sqrt{2}\kappa H_c.$$

$H_c$ for type II superconductors is the thermodynamic critical field defined previously [2]. Of note with both types of superconductors is the existence of a surface sheath of superconductivity which manifests itself as a higher surface critical field for Type II superconductors and a lower surface critical field for Type I superconductors (the limiting critical field for supercooling). The limiting value for the surface critical field, $H_{c3}$, was determined by Saint-James and de Gennes [8] to be the following [2]:

$$H_{c3} = 1.695H_{c2} = 1.695\left(\sqrt{2}\kappa H_c\right).$$

With the basic characteristics established for the superconducting types, the last topic for this section is discussion on the meaning of conventional superconductivity.

The description of conventional superconductivity comes from the qualifications of the two-particle wavefunction presented in BCS theory. This two-particle wavefunction is the following:

$$\psi_o(\overrightarrow{r_1} - \overrightarrow{r_2}) = \left[\sum_{k>k_F} g_k \cos\left[\vec{k} \cdot (\overrightarrow{r_1} - \overrightarrow{r_2})\right]\right](\alpha_1\beta_2 - \beta_1\alpha_2).$$

The wavefunction follows from the Bloch theorem description of a normal state electron wavefunction in a crystal lattice. Qualifications of this wavefunction are the following. First, the momentum of the two electrons is considered to be equal and opposite. Second, cosine was chosen to describe the plane waves. To preserve antisymmetric exchange of the wavefunction, the spin singlet state, $(\alpha_1\beta_2 - \beta_1\alpha_2)$, was required where $\alpha_1$ describes the spin up state of

particle 1 and $\beta_1$ describes the corresponding spin down state of particle 1. With these qualification in place, this wavefunction was used in the Schrödinger wave equation to successfully determine the possibility of electron pairing with an attractive (and weak) interaction. This attractive interaction in turn was determined to be an electron-phonon interaction as evidenced by the isotope effect where the critical values, $T_c$ and $H_c$, are proportional to $M^{-1/2}$ (M = isotope mass). A qualification of the wavefunction that resulted from the calculation of the attractive interaction was that the plane wave coefficients, $g_k$, possessed a spherical symmetry with regard to the energy difference between the excited pair state and the Fermi energy. This spherical symmetry indicates an *s*-wave state (zero angular momentum) for a superconductor which is associated with an isotropic gap. Implicit to BCS theory is the assumption of a crystal lattice with inversion symmetry [2,5]. Superconductivity in a crystal without inversion symmetry (noncentrosymmetric) is to be discussed next.

**1.3 Novel Superconductivity**

The term novel with regard to this investigation refers to phenomena occurring outside of the expectations from BCS theory. Noncentrosymmetric superconductors present an exciting opportunity for novel superconductivity since the lack of spatial parity can give rise to a mixed spin-singlet, spin-triplet state [9]. A mechanism that has been observed to influence the expression of the spin-triplet state is Rashba-type antisymmetric spin-orbit coupling described by the following Hamiltonian term:

$$\mathrm{H_{ASOC}} = \sum_{\mathbf{k}} \sum_{s,s'} \mathbf{g_k} \cdot \boldsymbol{\sigma}_{s,s'} c^{\dagger}_{\mathbf{k}s} c_{\mathbf{k}s'}.$$

The function, $\mathbf{g_k}$, defines the antisymmetric spin-orbit coupling as $\mathbf{g_{-k}} = \mathbf{-g_k}$ which gives energy splitting of the Fermi surface of order 10-100 meV. Since this energy splitting is greater than typical superconducting gap energies, modification of the pairing wavefunction is expected [10].

NCS can be grouped into two categories based on the influence of electron correlation in these materials. Highly-correlated NCS possess large effective electron masses (typically $\sim 100 m_o$) usually due to being in proximity to a magnetic quantum critical point as evidenced in some materials by the coexistence of long range magnetic order and superconductivity. Weakly-correlated NCS possess light effective electron masses (typically $\sim m_o$) and no significant long range magnetic order [10]. Examples of both classes will be discussed next.

The group of highly-correlated NCS are mostly Ce-based *f*-electron materials. $CePt_3Si$ ($\gamma$ = 200 mJ/mol·K$^2$) bears some distinction in the group as it is a superconductor ($T_c$ = 0.75 K) at ambient pressure in addition to being an antiferromagnetic (AFM) material ($T_N$ = 2.25 K) $CePt_3Si$ is a Type II superconductor with $\kappa \approx 140$ and a tetragonal *P4mm* structure. The relationship of long range AFM magnetic order to superconductivity is seen clearly in $CePt_3Si$ as a function of the level of chemical substitution of Ge for Si. Figure 1.2 displays a plot of the Neel temperature ($T_N$) and superconducting critical field ($H_c$) as a function of doping and unit cell volume from Bauer, et. al. The increase in pressure of the unit cell depresses $T_N$ until an extrapolated intersection occurs with the superconducting dome. This relationship of magnetism and superconductivity in $CePt_3Si$ points strongly to an unconventional pairing mechanism such as spin fluctuations. Further evidence of unconventional superconductivity in $CePt_3Si$ is observed in the heat capacity

of the superconducting state. As mentioned earlier in this section, a BCS superconductor exhibits an exponential form for heat capacity consistent with an isotropic energy gap. Figure 1.3 displays the heat capacity for $CePt_3Si$ which reveals a $T^2$ dependence at low temperature. This power law behavior represents a departure from an isotropic energy gap in favor of an anisotropic energy gap that coexists with a point or line on the Fermi surface called nodes. The ratio of heat capacity jump to normal state level ($\Delta C/C_n$) was determined to be 0.25. This sub-BCS value was argued to be a result of the pairing mechanism since comparison between polycrystalline and single crystalline measurements yielded similar results [11]. In the next couple paragraphs, NCS superconductors in the absence of strong electron correlation will be discussed.

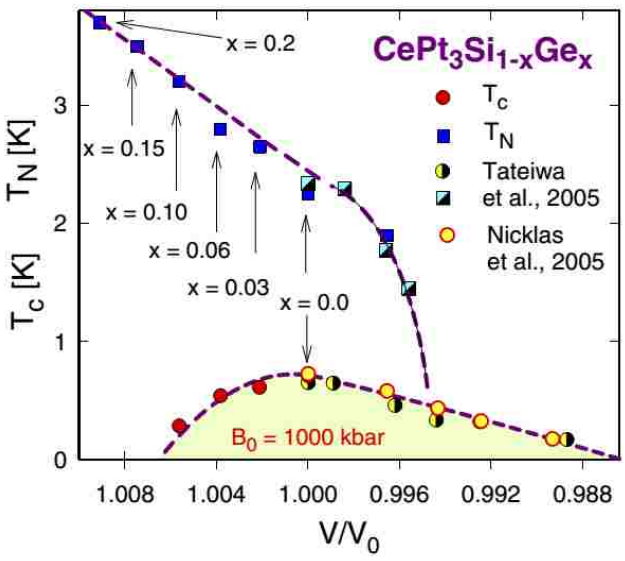


Figure 1.2: Magnetic and superconducting phase diagram of $CePt_3Si$ doped with Ge [11].

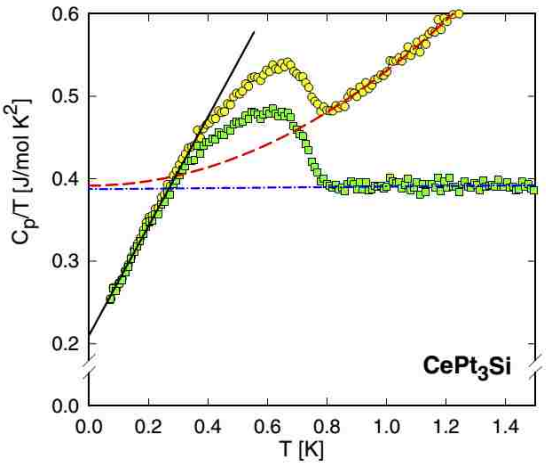


Figure 1.3: Specific heat data for $CePt_3Si$. Yellow spheres represent full specific heat while green squares represent specific heat with a $T^3$ fit (red) subtracted. The linear fit (black) represents $C_{es} \sim T^2$ [11].

The first weakly-correlated NCS to be discussed is $BaPtSi_3$ with $\gamma = 5.7$ mJ/mol·K$^2$. $BaPtSi_3$ has a tetragonal structure with *I4mm* space group and is classified as a Type II superconductor with $T_c = 2.25$ K. Figure 1.4 displays the heat capacity for $BaPtSi_3$ including a fit for the exponential BCS

form of the superconducting state from Bauer, et. al. The data is observed to trend with the BCS fit except at the lowest temperatures where the authors argue the divergence could be due to measurement issues or a small impurity effect. The ratio $\Delta C/C_n$ was determined to be 1.38 which lies close to the BCS value. Thus, the probing of the gap through specific heat indicated a complete, isotropic gap with predominantly spin-singlet pairing in the weak coupling limit as consistent with BCS theory [12]. Conventional BCS superconductivity has been observed in other weakly-correlated NCS such as β'-$Mg_2Al_3$ with $\gamma$ = 6.6 mJ/mol·K$^2$ and cubic $Fd\bar{3}m$ structure, $Ir_2Ga_9$ with $\gamma$ = 6.9 mJ/mol·K$^2$ and monoclinic *Pc* structure, $Cd_2Re_2O_7$ with $\gamma$ = 30 mJ/mol·K$^2$ and (pyrochlore) tetragonal $I\bar{4}m2$ structure, etc [10].

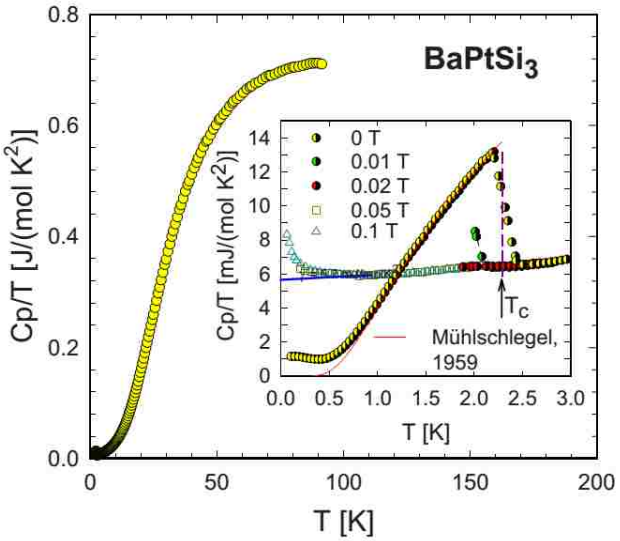

Figure 1.4: Specific heat for $BaPtSi_3$ [12].

While most weakly-coupled NCS seem to be well described by BCS theory, there are a few examples that provide motivation for continued study of this class of NCS. One of the best examples is $Li_2Pt_3B$ which has been compared with $Li_2Pd_3B$ since the two materials are the extrema of an isostructural solid solution series in terms of Pt and Pd. The structure of $Li_2(Pt/Pd)_3B$ is (antiperovskite) cubic *P4₃32*, with weak electron correlation as observed in the electronic specific for $Li_2Pt_3B$ ($\gamma$ = 7 mJ/mol·K$^2$) and $Li_2Pd_3B$ ($\gamma$ = 9 mJ/mol·K$^2$). Figure 1.5a displays the specific heat for $Li_2Pt_3B$, and Figure 1.5b displays the specific heat for $Li_2Pd_3B$. Takeya, et. al concluded from this data that both materials follow the BCS exponential form indicative of an isotropic fully gapped superconducting state. The ratio $\Delta C/C_n$ for $Li_2Pt_3B$ was

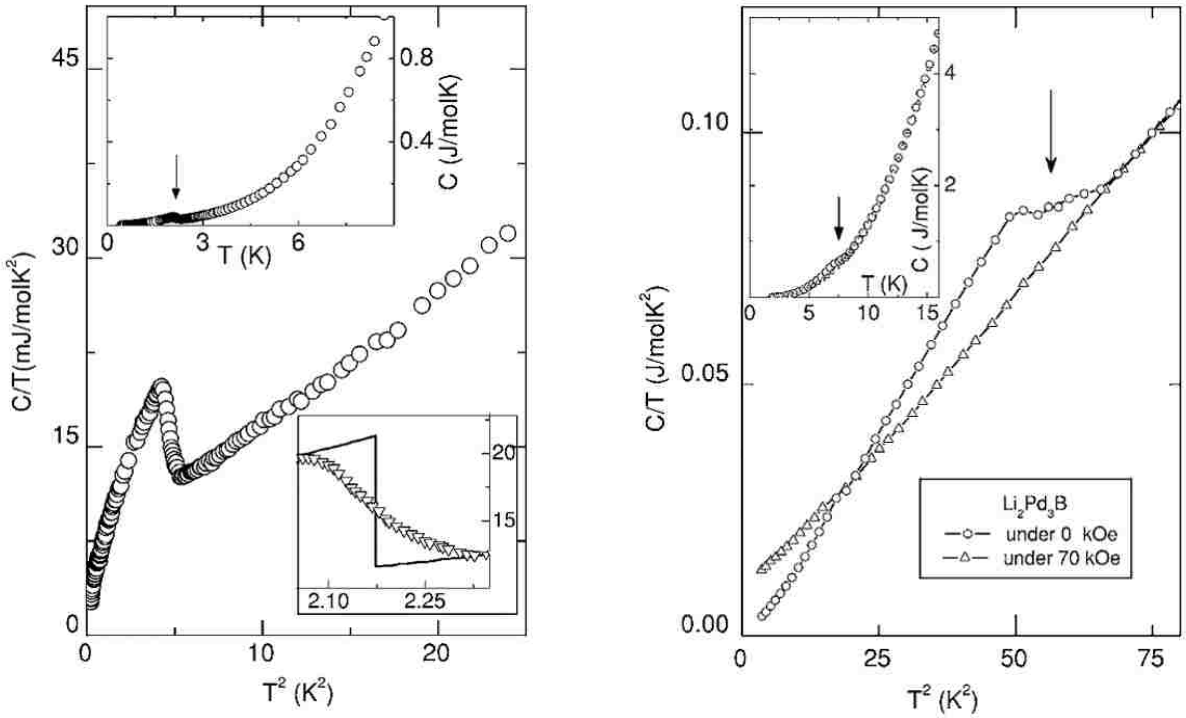


Figure 1.5: (a) Specific heat for $Li_2Pt_3B$. (b) Specific heat for $Li_2Pd_3B$ [13].

determined to be 1.39 which is close to the BCS value in the weak coupling approximation, and for $Li_2Pd_3B$ the ratio was 2.0 which the authors attributed to an intermediate level of coupling [13]. A subsequent paper by Yuan, et. al provided further research that highlighted the unconventional nature of superconductivity in $Li_2Pt_3B$. The authors performed a penetration depth study of $Li_2Pt_3B$ and $Li_2Pd_3B$ via an HF resonance technique. The results are displayed in Figure 1.6 and reveal strikingly different behavior between the two materials. The $Li_2Pd_3B$ sample showed BCS-like behavior in that the penetration depth leveled off as temperature approached 0 K. The $Li_2Pt_3B$ showed distinctly different behavior in that the penetration depth decreased in a linear fashion with no leveling at lowest temperatures. The authors concluded that $Li_2Pt_3B$ is an *s*-wave superconductor with line nodes in the gap. Additionally, they noted that the specific heat data presented in Takeya, et. al would fit better to $C_{es} \sim T^2$. The implications of the studies on $Li_2Pt_3B$ are the following. First, unconventional superconductivity

can arise in a superconductor with an electron-phonon pairing mechanism. This provides an interesting contrast to the highly-correlated NCS where magnetism is connected to unconventional superconductivity. Second, since $Li_2Pd_3B$ was determined to be a BCS-like superconductor in all aspects, the role of Pt in this crystal structure is observed to contribute more to the antisymmetric spin-orbit coupling than Pd since it is more massive. This provides insight that not only is a noncentrosymmetric structure necessary for unconventional superconductivity (in the absence of highly correlated electron phenomena), but also elements that provide a high degree of spin-orbit coupling [14].

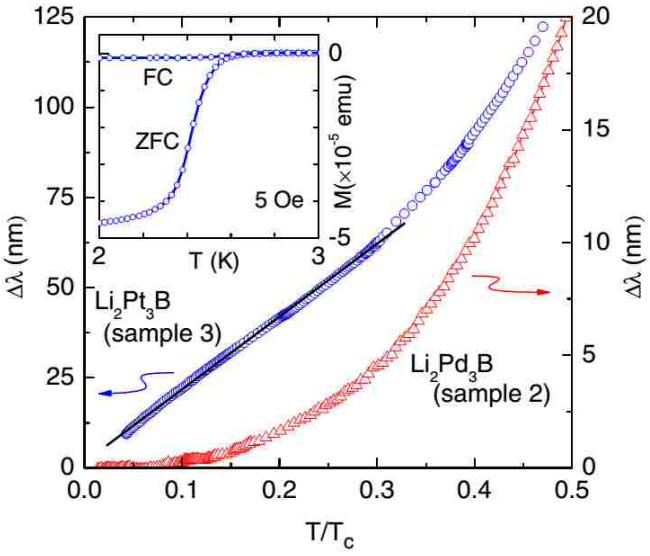


Figure 1.6: Penetration depth study of $Li_2Pt_3B$ (blue) and $Li_2Pd_3B$ (red). Black line is the linear fit to $Li_2Pt_3B$ at low temperatures [14].

To conclude this section, brief discussion will be given on the primary metric available to us for the determination of novel (unconventional) superconductivity in AuBe. Specific heat measurement has been demonstrated for multiple materials to be a probe of the superconducting gap dynamics and gauge of the pair coupling strength. Departure from the exponential form for electronic specific heat in the superconducting state and drastic change in the ratio $\Delta C/C_n$ will be our primary metric for novel superconductivity in AuBe. In addition to specific heat, magnetization (dc/ac) and resistivity will also be used to characterize the critical values for field and temperature for the superconducting phase diagram.

**1.4 AuBe**

The structure of AuBe was first characterized and published by B. D. Cullity in 1947 (predating BCS theory). Cullity found AuBe to best fit the space group $P2_13$ also designated *B20* and FeSi-type [15]. Figure 1.7a,b,c depicts the symmetries described by $P2_13$. The structure is cubic (Figure 1.7a), possesses the symmetry of a two-fold screw axis (Figure1.7b), and possesses the symmetry of a three-fold rotation axis (Figure 1.7c). While not evident in the unit cell, an assembly of unit cells 2x2x2 displayed in Figure 1.8a,b reveals a chiral symmetry along the [1,1,1] axis of the crystal.

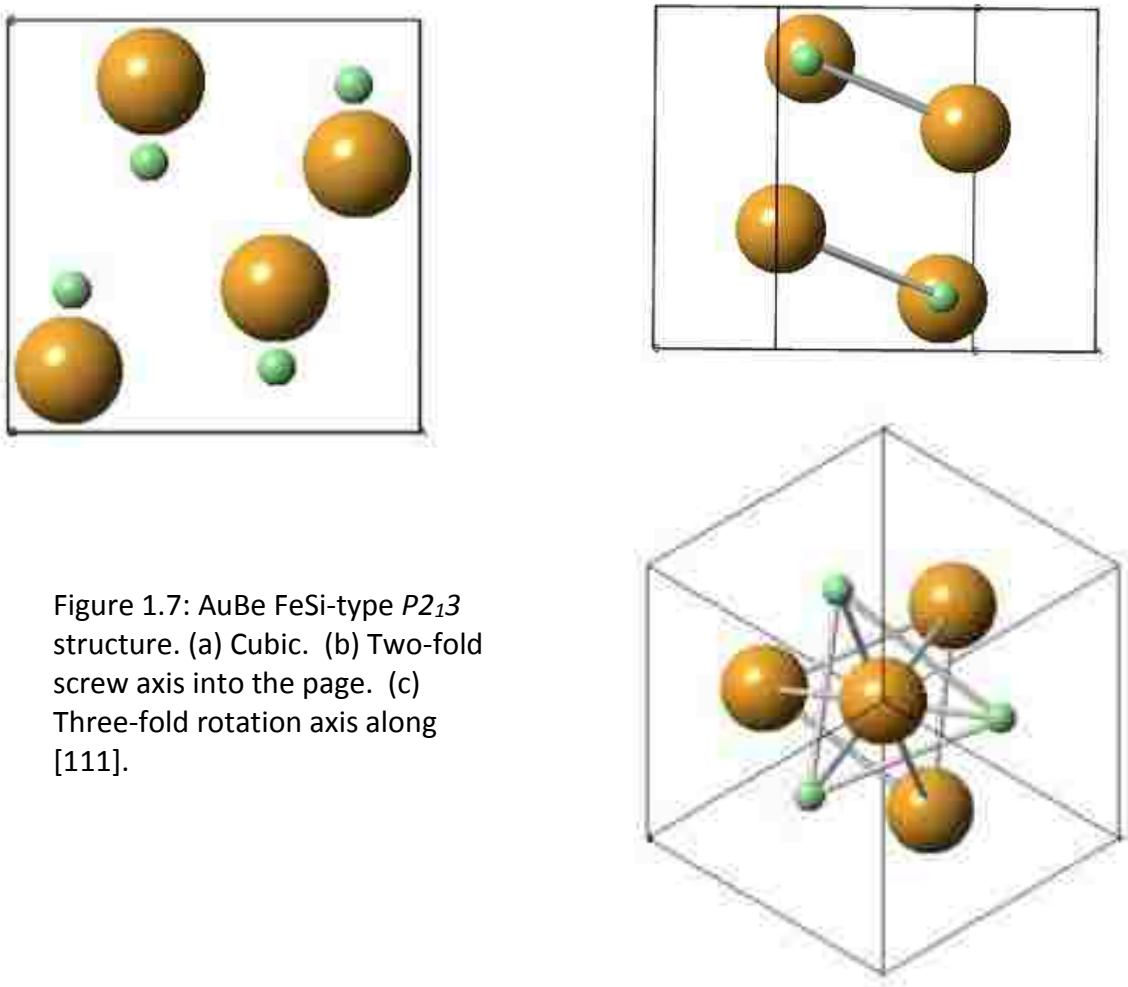

Figure 1.7: AuBe FeSi-type $P2_13$ structure. (a) Cubic. (b) Two-fold screw axis into the page. (c) Three-fold rotation axis along [111].

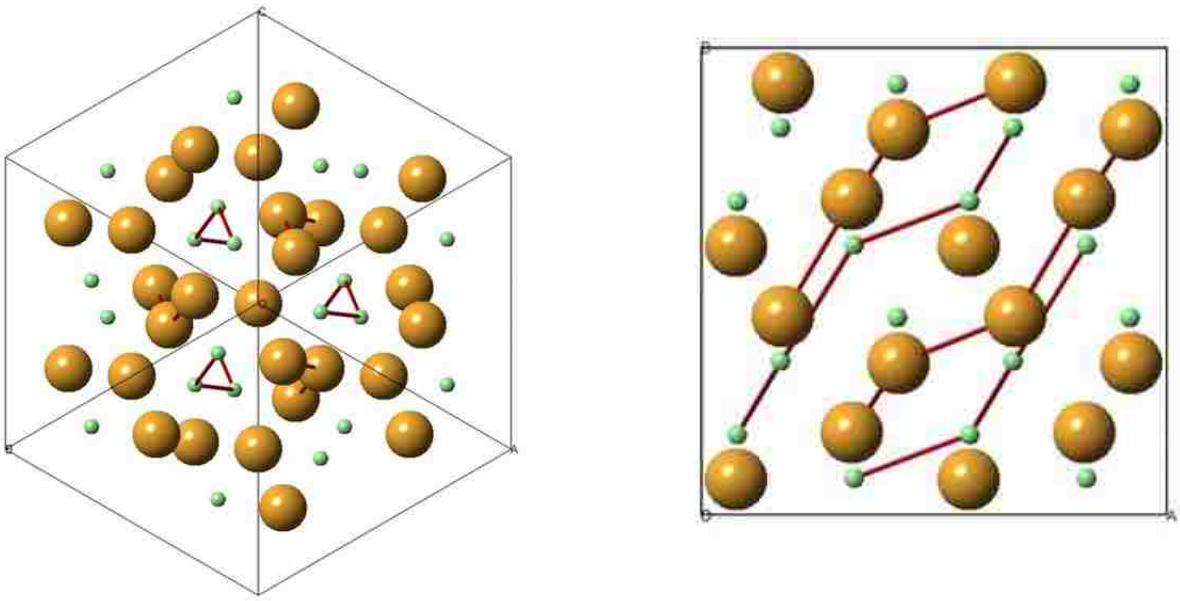

Figure 1.8: AuBe 2x2x2 unit cells. (a) Six chiral axes parallel to [111] (into the page) and the axis for three-fold rotation symmetry. (b) Side view with chiral atom sets shown connected.

The discovery of superconductivity in AuBe was published by B. T. Matthias in 1959 (2 years after BCS theory). In this short paper, the absence of superconductivity in gold and beryllium was noted along with the scarcity of Au alloy superconductors [16]. Beryllium was later found to have a $T_c$ of 0.026 K [17]. The author investigated the gold-rich side of the Au-Be phase diagram finding no superconductivity till a 1:1 stoichiometry (AuBe) was characterized. The synthesis method used was a simple solid state reaction in a quartz tube. The superconducting critical temperature, $T_c$, was found to be 2.64 K. No information on characterization technique or applied field (if any) was given so it is unclear if this $T_c$ represents the true critical temperature [16]. As far as we know from searching through literature, AuBe is the only superconductor with the FeSi-type *B20* structure.

Our motivation for the further characterization of AuBe stemmed from the dramatic influence that the *B20* structure has on the magnetic structure in other *B20* compounds. In a

handful of *B20* structures (MnSi [18], $Fe_{1-x}Co_xSi$ [19], FeGe [20], MnGe [21], $Cu_2OSeO_3$ [22] etc.), a static magnetic vortex state termed the skyrmion state exists as an intermediate state between the helimagnetic state and ferromagnetic state. Figure 1.9 displays a Lorentz TEM image of skyrmions in FeGe from the work of Yu, et. al [20]. The role of structure in this phenomena is made clear by the fact that the bulk skyrmion effect only occurs in *B20* and related structures, and this group of *B20* materials contain both itinerant magnets and an insulator. Since the *B20* structure plays such a crucial role in the formation of a magnetic topological structure, we pursued characterization of the superconducting state in AuBe in search of a signature for unconventional superconductivity.

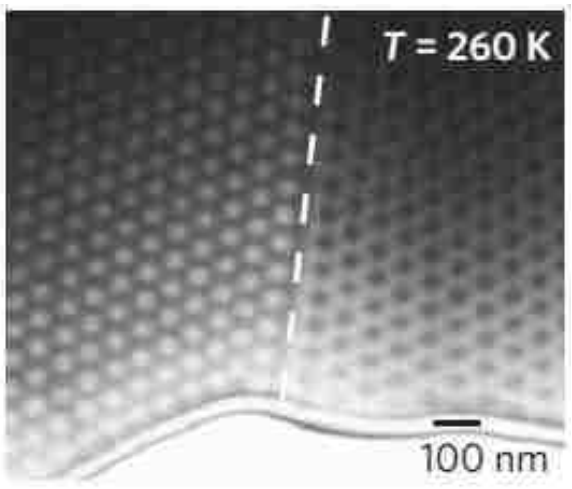

Figure 1.9: Two magnetic skyrmion domains in a thinned FeGe cross section [20].

The original question of whether novel superconductivity exists in AuBe can now be qualified. The study presented earlier on $Li(Pt/Pd)_3B$ experimentally determined that heavy elements which are known to have large spin-orbit interaction are excellent candidates for unconventional superconductivity in weakly-coupled NCS. AuBe has one heavy element, Au, and is not only noncentrosymmetric but also chiral meaning that it lacks mirror symmetries. This presents a unique opportunity to characterize a chiral NCS superconductor independent of known mechanisms for unconventional superconductivity amongst strong and weakly correlated NCS.

# Chapter 2: Methods

## 2.1 Introduction

Experiments were designed to answer the questions concerning AuBe that were addressed in Chapter 1. This chapter describes the synthesis, sample preparation, and characterization techniques utilized for our analysis of the superconducting properties of AuBe. Section 2.2 describes the processes for polycrystalline and single crystal synthesis of AuBe. Section 2.3 describes the elemental and structural analyses used to confirm the identity of AuBe. Section 2.4 relates the techniques for magnetization characterization of the superconducting state using both dc and ac applied magnetic fields. Section 2.5 outlines electron transport measurements which include resistivity and the Hall effect. Resistivity measurements were used to characterize the transition into the superconducting state while the Hall effect was used to determine charge carrier type and density. Section 2.6 reports the technique utilized for heat capacity characterization of the superconducting state and transition at the critical temperature. Section 2.7 concludes the chapter with a description of the techniques involved with the characterization of the AuBe Fermi surface by de Haas-van Alphen oscillations in high applied magnetic fields.

## 2.2 Synthesis

The synthesis of polycrystalline AuBe was accomplished by two different techniques in collaboration with Professor David Young at LSU. This section begins with discussion of these techniques followed by a description of our attempts at AuBe single crystal growth. The first synthesis method was performed by Dr. David Young and employed a HÜTTINGER Elektronik TIG

Figure 2.1: RF furnace.

20/100 radio frequency (RF) furnace for the melting of gold shot and beryllium chunks massed in stoichiometric ratio for AuBe. The furnace is pictured in Figure 2.1. The setup involved placing the elements in a ceramic alumina crucible with a tantalum flux susceptor (inductive heating element). The chamber was evacuated and filled with argon gas three times after which the chamber was filled with argon near or just above room pressure. The RF furnace operates at 120 kHz with a maximum power of 20 kW. For this AuBe synthesis, the power was gradually increased till the elements melted in the crucible as seen from visual inspection through a window at the top of the chamber (~50% power). The power was then terminated, and the product in the crucible was allowed to cool.

The second synthesis was performed by me with the assistance of Dr. Tapas Samanta, a postdoctoral researcher in the lab of Professor Shane Stadler. This method employed an arc-melting apparatus which consists of a Miller Gold Star 400SS welding machine connected to a water-cooled chamber that includes a copper hearth, quartz viewing window, and prong electrode tipped with tantalum. This apparatus is pictured in Figure 2.2. Gold shot and beryllium chunks were massed in stoichiometric ratio for AuBe and placed on the copper hearth. After sealing, the chamber was evacuated and purged with argon gas three times after which the argon was kept flowing at a small positive pressure. Care was taken in this process not to blow around

the elements in the copper hearth. The tantalum tip was brought near the edge of the copper hearth, and the welder power turned on. The tip was briefly allowed to touch the copper crucible to strike the arc. The tip with arc was then swept around the outside of the crucible and spiraled inward toward the elements. During the spiraling, the elements melted together forming a large symmetric droplet in the center of the hearth. The tip was rotated in a tight circle above this droplet for approximately a minute or less. Care had to be taken not to overheat and crack the quartz viewing glass or melt the tantalum tip. After cutting the power, the sample cooled quickly against the copper hearth and was kept under argon atmosphere for ten minutes or longer. Samples were typically arc melted four times sequentially without removal from the argon atmosphere.

Figure 2.2: Arc melter.

Attempts were made to grow AuBe with a single crystalline domain. Two difficult hurdles for this process had to be overcome. First, our typical method of placing reactants in a quartz tube did not work because beryllium reacted with the quartz at high temperature. Second, beryllium possesses a high vapor pressure making reaction in a sealed quartz tube or any evacuated vessel impossible. These hurdles were problematic for the earlier attempts at polycrystalline synthesis with the RF furnace. An attempt at synthesis in an optical floating zone furnace was made using powdered AuBe from one of the arc-melt reactions. This particular technique was performed in collaboration with Dr. Rongying Jin and graduate student Zhenyu

Diao. The precursor was sealed in a quartz tube by necessity due to the toxic nature of beryllium. The temperature of the precursor was gently raised till melting was achieved by visual inspection. After completion, elemental beryllium was observed to have separated along the sides of the quartz tube.

A specialized approach needed to be developed for the hurdles mentioned in the last paragraph. After researching past approaches for beryllium crystal synthesis and availability of nearby equipment, a modified Bridgman technique was devised in collaboration with Dr. David Young. The Bridgman technique requires that a sample be pulled through a temperature gradient maintained between the heating elements of a furnace and the outer environment. Given the high vapor pressure of beryllium and its toxicity, a furnace with argon gas flow sealed from the ambient lab environment was an additional requirement. The only available furnace with such options was the RF furnace with a sealable quartz tube liner and gas lines for argon atmosphere. Graphite was chosen as the susceptor sleeve for the growth crucible. In order to judge the nature of the temperature gradient for a graphite susceptor inside the coil of the RF furnace, a cylindrical piece of graphite was machined and hung inside the coil. Specifically, we wanted to see by visual observation of the susceptor's glow if the heating inside the coil was uniform or if a heat gradient tapered off from the center of the coil. After sealing and purging the chamber, the RF generator power was ramped until the graphite glowed. Visual inspection of the glowing graphite seen in Figure 2.3a revealed a heat gradient tapering off from the middle. Since a well-defined temperature gradient was desired, we experimented further with a conical

a

b

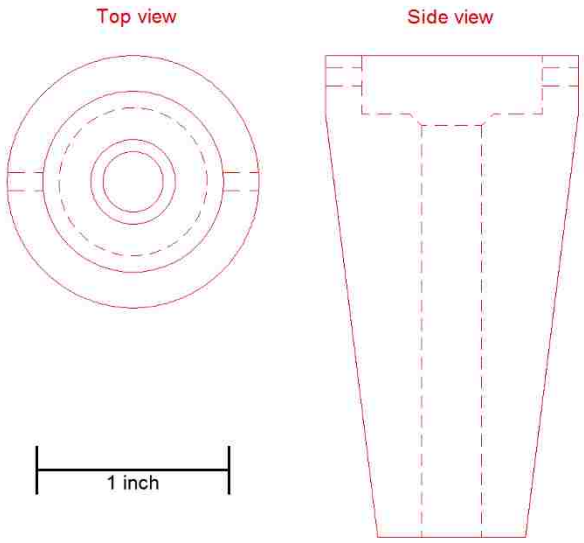


c

Figure 2.3: a) Cylindrical graphite susceptor. b) Conical graphite susceptor. c) Graphite susceptor design for AuBe synthesis.

piece of graphite. Induction heating of the susceptor is dependent upon cross section, and we wanted to see if the heating gradient inherent to the tapered inductor would overcome the heat gradient seen in the cylindrical piece of graphite. The result is pictured in Figure 2.3b and shows a well-defined heat gradient along the length of the cone. With this information in mind, a conical graphite susceptor sleeve displayed in Figure 2.3c was designed for the AuBe growth crucible. For the growth crucible, an examination of past research on beryllium revealed BeO to be a good candidate for a growth crucible [23,24]. A layout for a BeO crucible was designed by myself with

the assistance of Dr. David Young that included a narrow seed growth channel opening to a larger cylindrical chamber for single crystal boule growth. A drawing of this design can be seen in Appendix A. Contacts were established at two American companies for the fabrication of this design, but neither could manufacture this growth crucible in the time frame we needed. In the end a long thin tapered BeO crucible was ordered from United Mineral & Chemical Corporation (U.S. distributor for the manufacturer DR. EBERL MBE-KOMPONENTEN GMBH) with the dimensions given in Figure 2.4. The graphite susceptor seen in Figure 2.3c was designed for this BeO crucible. With all the necessary components assembled, we next focused on the synthesis process.

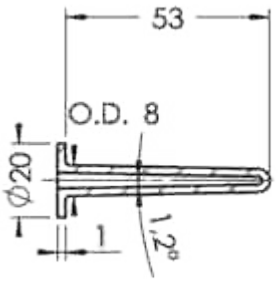

Figure 2.4: BeO crucible sketch with dimensions in mm [25].

Stoichiometric amounts of Au and Be were measured and melted together in an alumina crucible placed inside the RF furnace with argon atmosphere. A tantalum foil wrapped around the crucible served as the susceptor. The Au-Be button was then crushed and placed inside the BeO crucible, and this crucible with the graphite susceptor described in the last paragraph was suspended in the RF coil. The RF furnace chamber was then sealed, evacuated, and purged with argon gas. Argon gas was then allowed to flow through the chamber (venting into a fume hood), and the RF power was slowly increased till melting of the Au-Be precursor was visibly observed. The RF power was then left constant (~40% power) and the susceptor assembly was slowly dropped through the coil at a rate of 2mm/hr. After two days, the assembly had dropped below the coil at which point the RF power was turned off.

The AuBe boule would not drop out of the BeO crucible so the crucible had to be carefully cracked open to extract the product. Visible examination of the boule clearly revealed a polycrystalline product. Upon close examination two crystals were observed in a pocket of the boule which are pictured in Figure 2.5. The small size of the crystals prevented our normal procedures for cutting which include electric discharge machining (EDM) and diamond saw cutting. A more precise cut was needed so a FEI Quanta 3D DualBeam FEG FIB-SEM system was utilized to excise one of the crystals with a focused beam of gallium ions. Figures 2.6a,b show SEM images of the crystal after the final side cut. Given that the crystal lay in a pocket, undercutting with the FIB proved impossible. Cuts on the long sides of the crystal were angled as far as possible underneath the crystal, and once the AuBe sample was taken out of the chamber, a razor blade was used to break off the crystal from its base. It should be noted that this crystal contains trace amounts of gallium (another superconductor) on the surface due to the FIB cutting. The AuBe crystal was ready for characterization after cleaning with acetone.

Figure 2.5: AuBe single crystals in boule pocket.

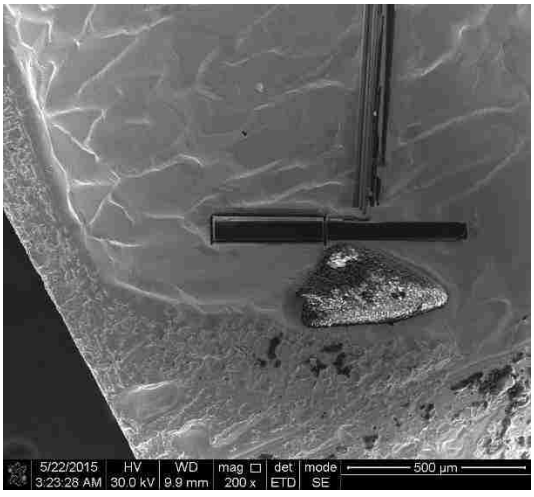


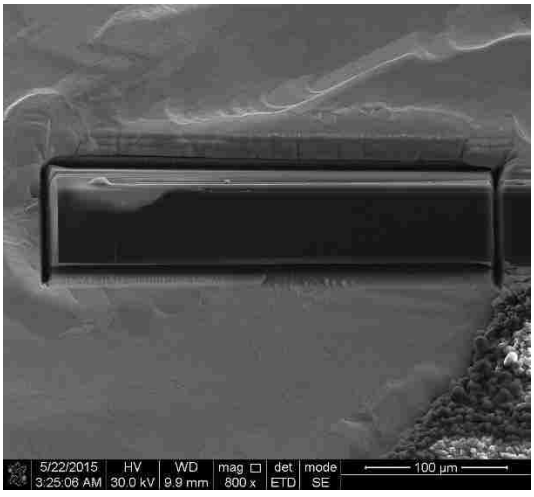


Figure 2.6: a) SEM image of AuBe single crystal after final cut. b) Magnified SEM image of cut AuBe single crystal.

## 2.3 Elemental and Structural Characterization

Primary analysis of the stoichiometry and crystal structure of AuBe was accomplished through powder x-ray diffraction performed by Professor Julia Chan at the University of Texas in Dallas. Elemental makeup of AuBe was impossible to determine with our typical technique for elemental analysis, energy-dispersive x-ray spectroscopy (EDS), due to beryllium spectral lines lying well below what is discernible with this technique. The possibility exists for elemental analysis with x-ray photoelectron spectroscopy (XPS) which is more sensitive of the lighter elements. Discussion of this analysis is left for the section on Future Work in Chapter 4. Thus, our knowledge of the elemental makeup of AuBe is inferred from known crystal structure identity and known superconducting critical temperature. No other known alloy of Au and Be possesses the $P2_13$ space group symmetry for its unit cell. Analysis of the crystal structure for AuBe and related alloys was performed Dr. Julia Chan using a Bruker D8 Advance Powder Diffractometer equipped with a LYNXEYE detector.

## 2.4 Magnetization and ac Susceptibility

Magnetization (M) and ac magnetic susceptibility ($\chi_{ac}$) were measured in two cryogenic systems in our lab. The first system was a Quantum Design Magnetic Property Measurement System (MPMS XL7) with Reciprocating Sample Option (RSO) and AC option. This system was limited to measurements down to 1.8 K so a small cryogenic system consisting of a Janis He-3 insert and Cryomagnetics He-4 dewar was used to pursue $\chi_{ac}$ down to ~0.4 K. All samples of AuBe for these measurements were shaped as long slender bars positioned with their long axis

parallel to the applied magnetic field. The following paragraphs describes measurement in the MPMS after which a description is given of measurement in the small cryogenic system.

The Quantum Design MPMS measures M and $\chi_{ac}$ in a temperature range of 1.8-400 K and applied magnetic field range of ±7 T. Magnetization measurement is achieved by moving a sample through a second-order superconducting gradiometer (Figure 2.7) which functions as a closed flux transformer. The gradiometer is coupled to an RF SQUID with accompanying proprietary electronics which act as a magnetic flux-to-voltage transducer. The sensitivity achieved with the RF SQUID is given as $\sim 5 \cdot 10^{-9}$ emu. The measurement process involves moving the sample through the gradiometer, picking up the voltage waveform, and deriving the sample magnetic moment from the waveform. This process is entirely controlled by the Quantum Design system leaving only certain details of the procedure up to the user such as quality of sample alignment in the coils, measurement averaging, etc. The RSO mentioned in the previous section is simply an optional measurement procedure and equipment for the MPMS that oscillates the sample through the coils as opposed to the typical process of pulling the sample stepwise through the coils (DC option on the MPMS menu). Oscillation of the sample in the coils allows for signal averaging and better quality of the measurement. All magnetization measurements of AuBe were made with the RSO [26,27].

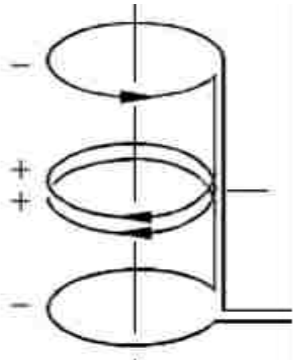

Figure 2.7: MPMS second-order superconducting gradiometer [26].

$\chi_{ac}$ measurement was performed with the RSO head and AC option. In addition to the previously mentioned gradiometer, the AC option includes a copper coil which lies between the gradiometer and the superconducting solenoid for the static applied magnetic field. This copper

coil provides the driving oscillatory magnetic field for the susceptibility measurement. After the amplitude and frequency of the driving field are set, a measurement cycle begins with the sample positioned in the bottom loop seen in Figure 2.7 and the SQUID circuitry nulled. The sample is then moved to the center of the gradiometer where the magnetic response is measured with the SQUID circuitry and a lockin amplifier allowing for the determination of both real and imaginary components of $\chi_{ac}$ [26,27].

Before examining the results of $\chi_{ac}$ measurements on AuBe in the next chapter, consideration of the interpretation of this measurement technique must be given. By definition the magnetic susceptibility is the derivative of the magnetization curve with respect to applied magnetic field ($\chi'_{ac}$ = dM/dH). Further information can be derived from the imaginary component of $\chi_{ac}$ such as weak phase transitions and dissipative phenomena. From a qualitative standpoint, $\chi_{ac}$ and the derivative of magnetization with respect to applied magnetic field should match when $\chi_{ac}$ is characterized at small driving oscillatory fields and low frequencies [27].

The above considerations for $\chi_{ac}$ also apply to susceptibility measurements made with our He-3 cryogenic system. A home-built susceptibility coil set previously fabricated by students in the DiTusa lab was used for the susceptibility measurement. A rough schematic drawn from examination of the coil set can be seen in Figure 2.8. A sample was attached with varnish to an epoxy post mount which was inserted into one of the pickup coils and attached with rubber cement. The pickup coil assembly consisted of a single epoxy shell with two copper coils

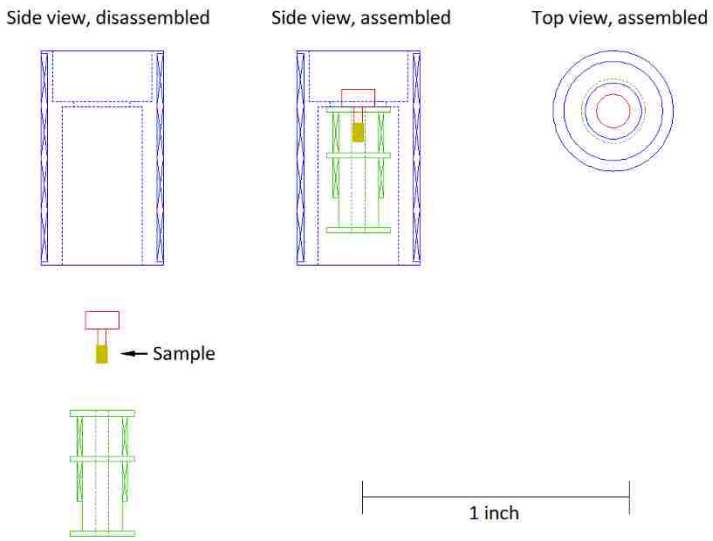


Figure 2.8: Sketch of susceptibility coil set used in the small cryostat system.

connected in series. The pickup coil assembly with sample was then inserted into the drive coil shell which consisted of epoxy and a single copper coil. The coil set was then attached to the cryostat end with rubber cement. Paired manganin wires in the cryostat column were selected for this measurement.

Susceptibility measurement was accomplished with a Signal Recovery 7265 digital lockin amplifier. As with most lockin amplifiers, the 7265 is equipped with an internal voltage oscillator which was used in all characterizations with this lockin amplifier. The lockin amplifier reports a measurement as a voltage phasor which can be given as a voltage magnitude and phase angle or real and imaginary components. For susceptibility measurements, the lockin amplifier's voltage source was wired in series with a 1k$\Omega$ resistor and the outer drive coil of the susceptibility coil set. The two measurement input channels (A,B) of the lockin amplifier were connected across the pickup coil assembly, and the lockin amplifier was set to measure the difference

($\Delta V = V_A - V_B = V_L$). While most of the data from this technique was normalized with data from the MPMS, comparison of $\chi_{ac}$ for different drive fields was accomplished using the following relation:

$$\chi_{ac} = \frac{V_L}{\tilde{V}}.$$

$V_L$ is the complex rms voltage measurement across the pickup coils and $\tilde{V}$ is the rms value of the voltage source driving the primary coil. It should be noted that while the same samples of AuBe were used in the susceptibility studies between the small cryostat and MPMS, different cuts of the same sample were used due to the confined dimensions of the home-built susceptibility coil set.

### 2.5 Electron Transport

Resistivity was characterized with a four probe AC lockin amplifier technique in the previously mentioned Quantum Design MPMS and small He-3 cryostat. The Hall effect was characterized with an AC lockin amplifier technique solely in the MPMS. Discussion will first focus on the resistivity measurement technique followed by a description of the Hall effect measurement technique.

Samples for resistivity measurement were cut to the shape of a narrow bar and further thinned to ~100 microns. The four probes of the measurement consisted of thin platinum wires attached to the sample surface with two-part silver epoxy. A sketch of sample and probe geometry is given in Figure 2.9. All resistivity measurements were taken with the long axis of the sample (current

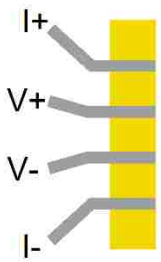

Figure 2.9: Four probe resistance measurement.

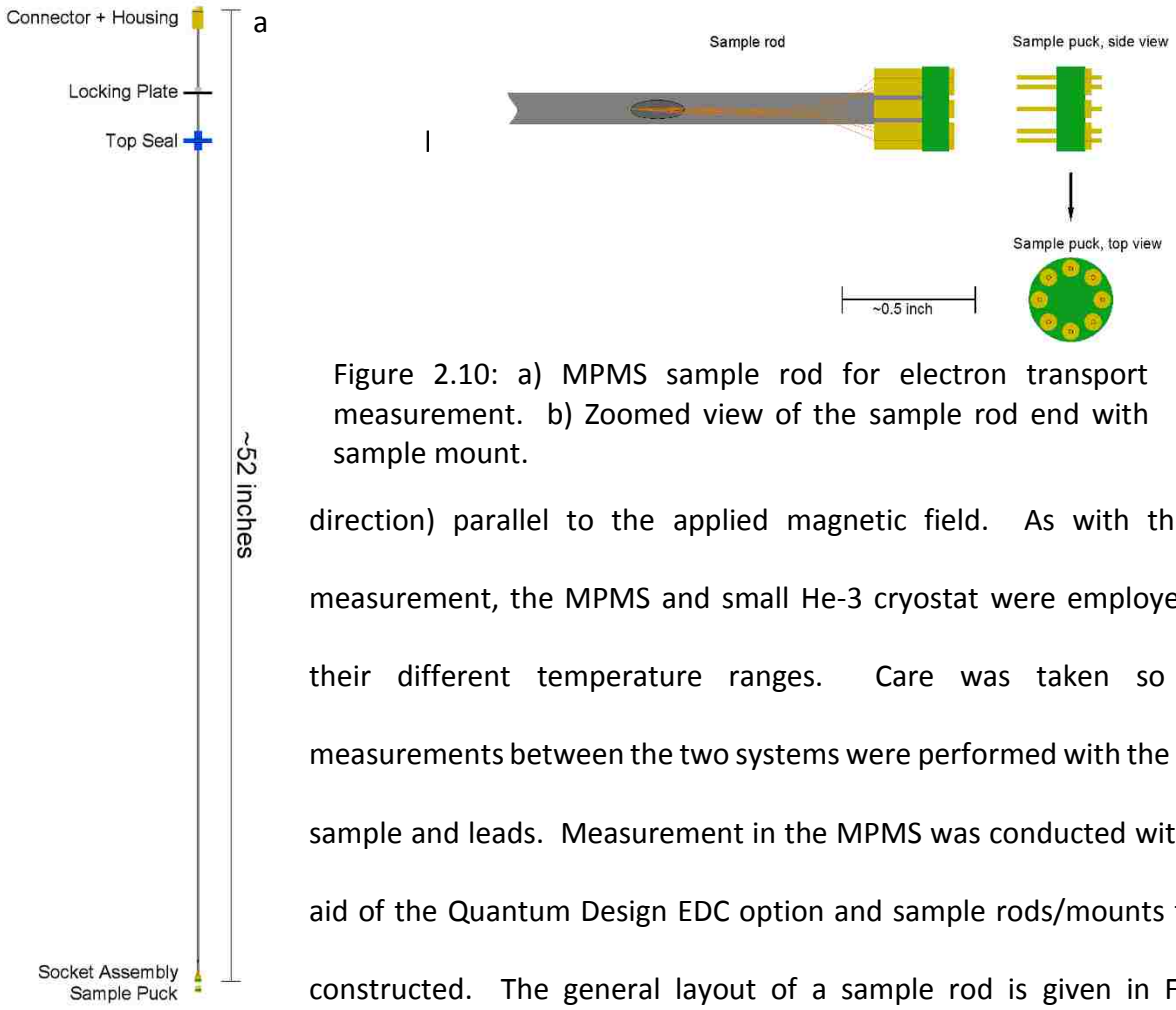


Figure 2.10: a) MPMS sample rod for electron transport measurement. b) Zoomed view of the sample rod end with sample mount.

direction) parallel to the applied magnetic field. As with the $\chi_{ac}$ measurement, the MPMS and small He-3 cryostat were employed for their different temperature ranges. Care was taken so that measurements between the two systems were performed with the same sample and leads. Measurement in the MPMS was conducted with the aid of the Quantum Design EDC option and sample rods/mounts that I constructed. The general layout of a sample rod is given in Figure 2.10a,b. Sample rods were constructed with a non-magnetic stainless steel tube and 38 awg polyimide clad copper magnet wire for the electrical connections. The top connector was soldered with Wood's metal to a machined brass can which was silver soldered to the steel tube. The assembly at the end of the rod consisted of a machined epoxy holder for sockets soldered to the copper wires. Sample pucks consisted of machined epoxy disks holding pins which mated to the sockets of the sample rod. A AuBe sample with leads attached was varnished to a small epoxy puck which was varnished upright in the center of the sample puck. The platinum sample leads

were silver pasted to the pins of the sample puck which completes the circuit of connector, coppers wires, sockets, pins, platinum wires, and sample.

Resistivity measurements were continued to lower temperatures by use of the He-3 cryostat. First, the before-mentioned small green epoxy disk with a AuBe sample and platinum leads was carefully removed from its MPMS sample puck. Next, the epoxy disk was varnished upright on the copper sample mount for the He-3 cryostat, and the leads were silver pasted to the pins of the sample mount.

Resistivity measurement both in the MPMS and He-3 cryostat followed a four probe AC lockin amplifier technique. A four probe resistance technique was employed to eliminate contact resistance from the measurement allowing for the best sensitivity. Given the low resistivity of AuBe as will be seen in the next chapter, this measurement technique was a necessity. The lockin amplifier for the MPMS measurement was a Signal Recovery 7260 Digital Lockin Amplifier, and the lockin amplifier for the He-3 cryostat measurement was a Signal Recovery 7265 Digital Lockin Amplifier. Both the 7260 and 7265 were equipped with internal voltage oscillators set at 19 Hz which were used exclusively in this project.

The combination of four probe resistance measurement and AC lockin amplifier technique is laid out in Figure 2.11. The internal voltage oscillator was wired in series with a large resistor (1 kΩ) to function as the current source for the four probe measurement and also the frequency reference. The voltage leads for the four probe measurement were wired to the A and B inputs of the lockin

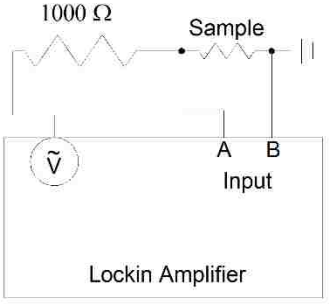

Figure 2.11: AC lockin amplifier four probe resistance schematic.

amplifier, and the lockin amplifier was set to report the voltage difference between the two inputs ($\Delta V=V_A-V_B=V_L$). Given that the large series resistor acted as the current limiter, the value of the current could be approximated from the voltage source and resistor using Ohm's Law ($V_{source} = I_{source}R$). Using this current value and $V_L$ from the lockin amplifier, resistance could be calculated using $V_L=I_{source}R_{sample}$. Labview programming with the He-3 cryostat used the following exact relation to calculate and report sample resistance:

$$R_{sample} = \frac{R_{resistor}}{\left(\frac{V_{source}}{V_L} - 1\right)}.$$

Since the lockin amplifier reports a voltage phasor, the real component of $V_L$ is chosen for resistance calculation. The imaginary component of the phasor gave information on the reactive elements of the circuit and was useful for determining quality of the leads and contact pads. Generally, phase angles of a couple degrees or less were considered acceptable.

To wrap up this section, a brief description will be given on characterization of the Hall effect in AuBe. The Hall effect was only measured in the MPMS, and processing of the sample followed the before-mentioned procedure for resistivity measurement except for lead placement. Sample geometry with leads displayed in Figure 2.12 was arranged to measure a positive voltage difference $\Delta V=V^+-V^-$ for a negative charge carrier. As previously described, this measurement also employed an AC lockin amplifier technique with $V_L$ ($\Delta V=V^+_A-V^-_B=V_L$) sensing the voltage transverse to the current direction. The formula describing the Hall effect is given as follows (SI units):

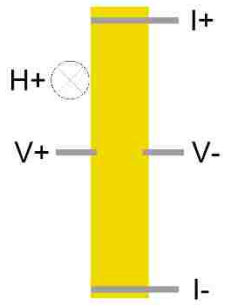

Figure 2.12: Hall effect measurement.

$$V_H = \frac{IB}{d} R_H.$$

$V_H$ is $V_L$ measured by the lockin amplifier, *I* is the current defined by the lockin amplifier voltage oscillator and series resistor, B is the applied magnetic field ($\mu_o H$), d is the thickness of the sample, and $R_H$ is the Hall coefficient defined by $R_H = 1/ne$ where e is the magnitude of electron charge and n is the charge carrier density to be determined along with the carrier type. Since the charge carrier type is determined by the sign slope of $V_H$ vs. H, the applied field direction in the MPMS was checked with a compass and determined to point up for positive field directions. This correlated to an applied field pointing into the surface of the sample as given in Figure 2.12. Given uncertainty associated with transverse lead placement, Hall voltage was measured for ±H and averaged using the relation $V_H=(V_{H+}-V_{H-})/2$ for the purpose of excluding longitudinal voltage pickup on the leads.

**2.6 Heat Capacity**

The heat capacity of AuBe was measured in collaboration with Dr. Phil Adams and performed by Dr. Joseph Prestigiacomo. Instrumentation used for the measurement was a Quantum Design Physical Properties Measurement System (PPMS) with Heat Capacity option and He-3 insert. Figure 2.13 displays a schematic from the Quantum Design manual showing the experimental apparatus. This setup for heat capacity measurement consists of a pre-fabricated puck with sample stage which includes a platform with heater and thermometer underneath. The sample stage is supported by fine wires which provide circuitry to the heater and thermometer along with connection to the thermal bath which is the frame of the puck [28].

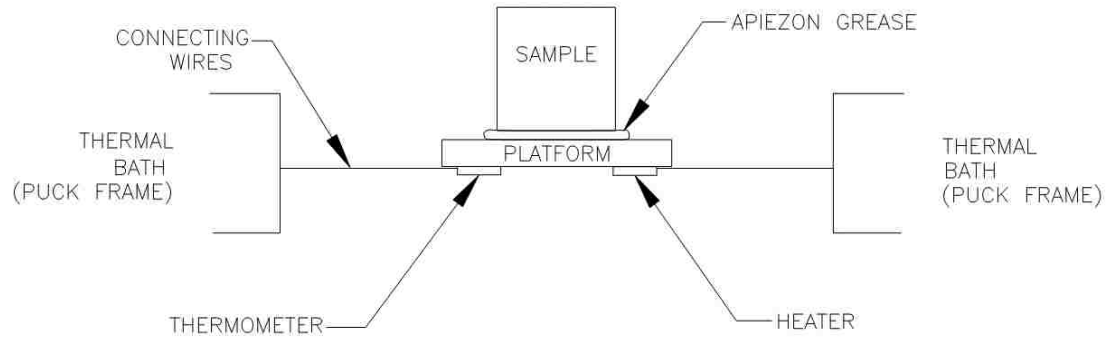


Figure 2.13: Quantum Design schematic for heat capacity measurement apparatus [28].

The system measures heat capacity at constant pressure ($C_P=(dQ/dT)_P$) which is accomplished in a two-step interval where a predetermined quantity of heat is applied for a set amount of time followed by cooling for the same amount of time. Exponential functions are fit to the heating/cooling regions of time-dependent temperature data, and a time constant is extracted equal to total heat capacity divided by the thermal conductance of the link to the thermal bath. The heat capacity measurement is first performed with no sample and only a small dab of grease which later serves as the glue to fasten the sample to the sample stage. Next, heat capacity measurement is performed with a bar-shaped sample fastened to the sample stage with the previously mentioned grease. The system calculates the total heat capacities for the blank stage (the addenda) and stage/sample combinations and subtracts these values in order to obtain the sample heat capacity [28].

## 2.7 de Haas-van Alphen Characterization

The de Haas-van Alphen (dHvA) effect was characterized with our Quantum Design MPMS XL at LSU and with a susceptometer in the 65 T multi-shot pulse magnet at the National High Magnetic Field Laboratory (NHMFL) located at the Los Alamos National Laboratory complex in New Mexico. Measurements in the MPMS were simply the (RSO) magnetization measurement

previously described but at much higher field. The dHvA effect was also observed in high field $\chi_{ac}$ measurements, but our research efforts concentrated on dc magnetization measurements. In the paragraphs to follow, dHvA characterization with a pulse magnet will be summarized followed by a short description of data processing and refinement.

Measurement of the dHvA effect at NHMFL, Los Alamos was performed in collaboration with Dr. John Singleton. The 65 T multi-shot pulse magnet is simply a resistive magnet coil that is connected to a large bank of capacitors. Inside the coil lies a dewar for liquid helium with a sealed inner chamber for the sample rod and He-3. Figure 2.14 displays the profile for a full 65 T pulse which last approximately 25 ms. Lower field pulses could also be selected which had the useful effect of changing the resolution of the field sampling as a function of time. The sample temperature range runs from 300 K to 450 mK if liquid He-3 is pumped upon in the inner sample space. The custom-built sample rod used for this measurement contained a coil for measurement of the applied field pulse, a resistive thermometer, and a susceptometer in which a AuBe sample was placed. Measurement with the pulse magnet consisted of the following process. First the capacitor bank was charged to the level corresponding to a selected pulse field maximum. Next the system would simultaneously trigger data sampling along with capacitor bank dump to the magnet coil. Determination of H was accomplished by integration of dH/dt and if needed, calibration with signal pickup from copper Fermi surface orbits inherent to the susceptometer pickup coils [29].

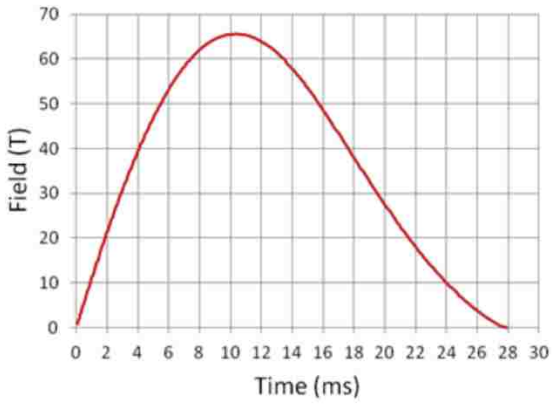

Figure 2.14: Pulse profile for the 65 T multi-shot pulse magnet [29].

Data analysis from the LSU MPMS and NHMFL pulse magnet followed the same process. Both magnetization and susceptibility data had Fermi surface quantum oscillations superimposed over a signal that could be fit to a third or fourth order polynomial. Thus, the first step in data analysis involved fitting the overall data curve to an appropriate polynomial function followed by subtraction of this fit from the data. Since dHvA oscillations are periodic in inverse field, the data was plotted as M (or $\chi$) vs. 1/H, resampled for evenly-spaced data in 1/H, and processed with a Fast Fourier Transform (FFT) program. The result was the frequency analysis of the data given in units of applied magnetic field. These frequencies could then be input into the following formula for the dHvA effect for the determination of extremal orbits:

$$\Delta\left(\frac{1}{\mathrm{H}}\right) = \frac{2\pi \mathrm{e}}{\hbar \mathrm{c}} \frac{1}{\mathrm{A_e}}.$$

It should be noted that the above formula is given in cgs units where the oscillation period Δ(1/H) is given in $Oe^{-1}$, e is the electric charge in esu, $\hbar$ is Planck's constant in erg·sec, c is the speed of light in cm/sec, and $A_e$ is the area of the extremal orbit in *k*-space with units of $cm^{-2}$. Assuming a spherical Fermi surface and free electrons, the following formula for Fermi surface energy from the Sommerfeld model could be used to generate plots of dHvA frequency components as a function of Fermi surface energy:

$$\mathrm{E_F} = \frac{\hbar^2 \mathrm{k_F^2}}{2\mathrm{m}}.$$

The Fermi wave vector was determined from the spherical surface assumption ($A_e=\pi k_F^2$).

With the research objective from chapter 1 in mind, the next chapter displays the results obtained from the experimental techniques discussed in this chapter.

# Chapter 3: Results

## 3.1 Introduction

Data pursuant to the questions addressed of AuBe in chapter 1 was obtained utilizing the methods described in chapter 2. This chapter presents this data including discussion of refinement and analysis. Section 3.2 begins with the confirmation of the research samples as AuBe with the *B20* crystal structure through XRD characterization. Section 3.3 presents data and analysis of the Meissner effect observed in magnetization and the superconducting phase transition observed in heat capacity. Section 3.4 discusses the characterization of the superconducting transition in the surface shielding currents of AuBe as probed by ac susceptibility. Section 3.5 completes the analysis of the superconducting state in AuBe with data from resistivity measurement. Section 3.6 follows up with the data and analysis of other electron transport measurements including the Hall effect and high field magnetoresistance. Section 3.7 concludes the chapter with the data and examination of the de Haas-van Alphen effect from magnetization and susceptibility measurements.

## 3.2 XRD Characterization

Powder XRD characterization was performed on Au-Be alloy samples in collaboration with Dr. Julia Chan at UT Dallas in order to identify structure and infer stoichiometry. Figure 3.1a displays the experimental peak positions for AuBe ($a_o$ = 4.659 Å [15]) with the theoretical peaks calculated by PowderCell [30]. The additional peaks were identified as minor impurity phases likely consisting of $Au_2Be$ and BeO. Figure 3.1b displays the normalized data (by largest peak in each set) for three different Au-Be alloys including AuBe that I synthesized for comparison

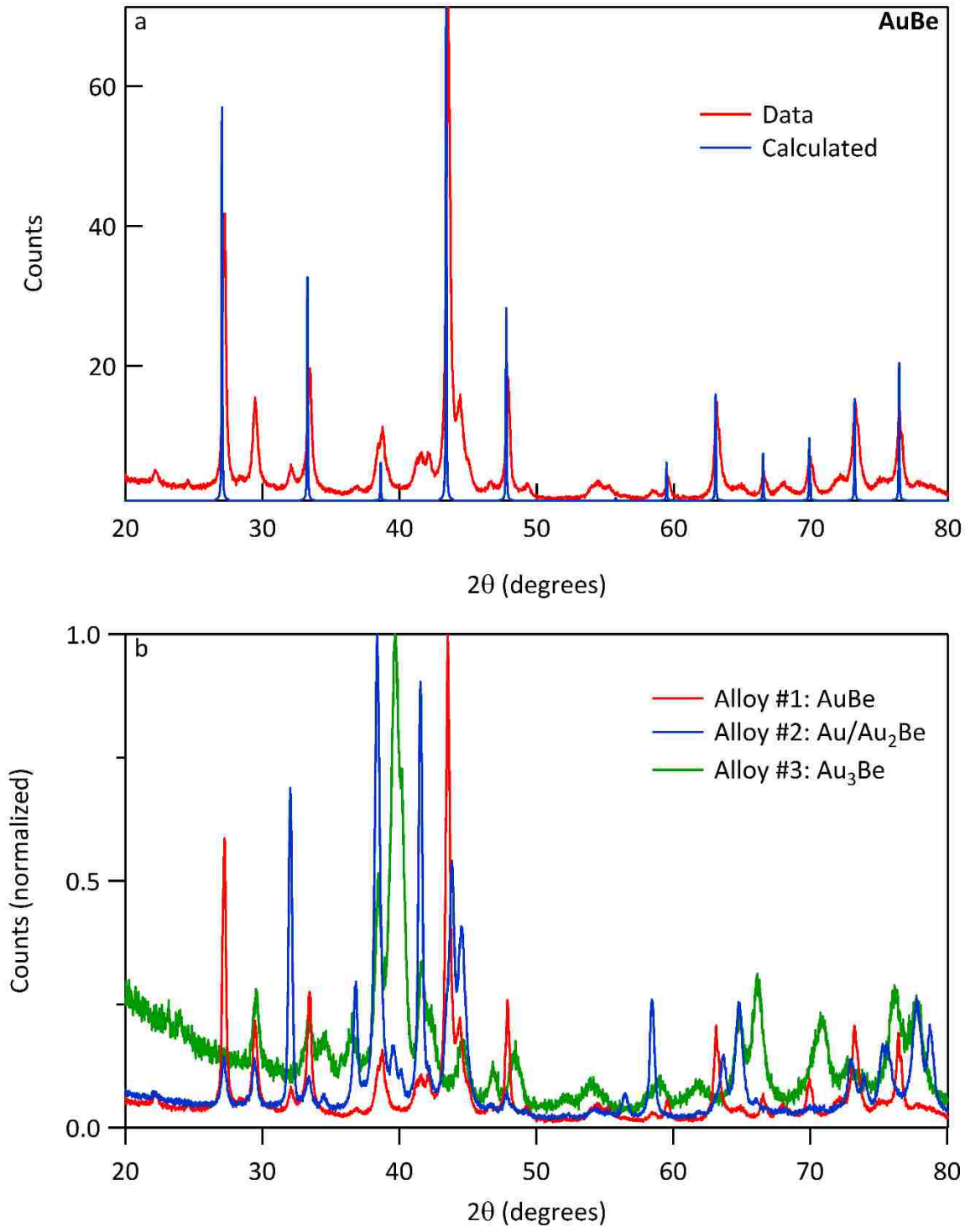


Figure 3.1: (a) AuBe powder XRD data with calculated peak positions. (b) Powder XRD data for three Au-Be alloys.

purposes. Of additional interest in the Au-Be set was alloy #2 which was originally intended to be $Au_4Be_3$ but ended up consisting of predominately $Au_2Be$ and Au with AuBe also possible from

the reaction [31]. As will be seen later in this chapter, alloy #2 displayed a diamagnetic signal characteristic of a superconducting transition.

The synthesis of what appeared to be a single crystal of AuBe (as discussed in chapter 2) posed some difficulty in identification of structure and stoichiometry given the size of the sample. The small size precluded our normal technique of cutting off a small piece to be powdered and analyzed with XRD diffraction. At Los Alamos National Laboratory, staff scientist Brian Scott performed single crystal x-ray diffraction analysis of this AuBe sample for the purpose of orienting the crystal. His analysis indexed the crystal to a cubic cell of approximately 4.6 Å and found that the cubic axes fell roughly along the sample faces. A large density of twinning boundaries in the crystal prevented further refinement of the axes. Additional analysis of sample identity came from magnetization measurements of the superconducting transition in isothermal applied field sweeps. This data to be presented in the next section showed close correspondence with the phase diagram obtained from polycrystalline AuBe samples. Thus, the single crystal XRD analysis and magnetization data provided conclusive evidence that the sample was AuBe and single crystal though highly twinned.

### 3.3 Magnetization and Heat Capacity

After the structural confirmation of AuBe, the next step in characterization was to explore the superconducting state in the AuBe sample volume. This was accomplished by characterization of the Meissner effect in magnetization (dc) and the superconducting phase transition in the specific heat. Figure 3.2 displays a complete field cycle of magnetization vs. applied magnetic field at 1.8 K revealing sharp superconducting transitions and the low-field

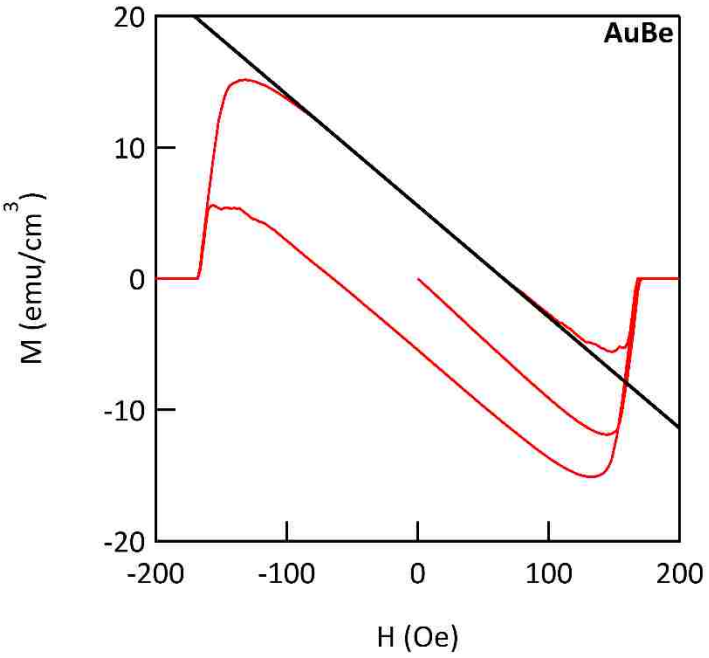


Figure 3.2: M vs. H at 1.8 K. The linear fit yielded a slope of $4\pi(dM/dH) = -1.1$.

slope, $\chi = 4\pi(dM/dH) = -1.1$. The following relationship [32] was used to extract the demagnetization factor (D) from the susceptibility ($\chi$):

$$\chi_{measured} = \frac{\chi_{internal}}{1 + D\chi_{internal}}.$$

Assuming a value of $\chi_{internal} = -1$ for a complete Meissner effect described by dimensionless mks units and zero for the imaginary component, the demagnetization factor was found to be approximately 0.09. This value in turn was compared to the demagnetization value for a sphere (0.33) and a cylinder (0.14) with the ratio (length/diameter) = 4 [32]. If the AuBe samples were approximated to be cylinders, the aspect ratio would be greater than 4 which would give a demagnetization factor less than 0.14. Since the value for D derived from an assumed full Meissner effect is an order less than 0.14, we infer that $\chi = -1.1$ is consistent with a full Meissner effect in the bulk of the sample. The sharp transitions were the first indication that AuBe is a Type

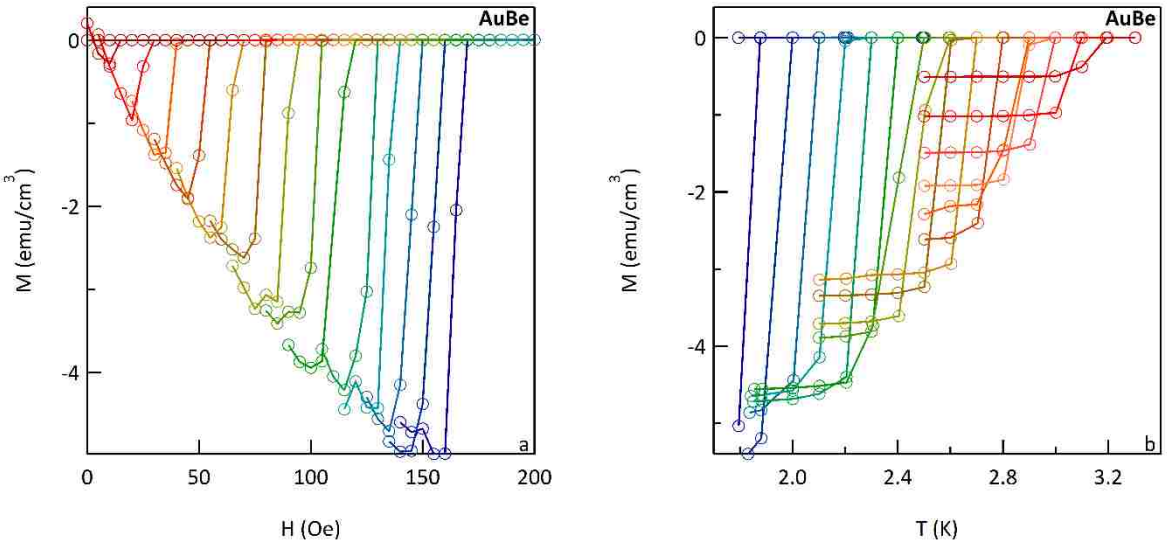


Figure 3.3: (a) M vs. H sweeps in 0.1 K increments starting with 1.8 K (blue) from right to left. (b) M vs. T sweeps in 10 Oe increments starting with 10 Oe (red) from right to left.

I superconductor. A small offset in the superconducting transition field between magnetic flux inclusion and expulsion indicated supercooling which further provided evidence of Type I superconductivity in AuBe. Figure 3.3a displays magnetization measurements in a series of applied magnetic field sweeps at constant temperature, and Figure 3.3b displays magnetization measurements in a series of temperature sweeps at constant field. The critical fields and temperatures for the AuBe superconducting phase diagram were extracted from these sweeps. For all field and temperature sweeps, the transition point chosen for a particular superconducting transition was taken as the onset of the transition from the normal-to-superconducting side.

Heat capacity measurement (specific heat) also confirmed a phase transition consistent with the onset of the Meissner effect in the volume of AuBe. Figure 3.4a displays the specific heat of AuBe at 0 Oe, 500 Oe, and 3,000 Oe and reveals the critical field to lie below 500 Oe for all temperatures measured. The critical temperature ($T_c$) from the 0 Oe data is approximately

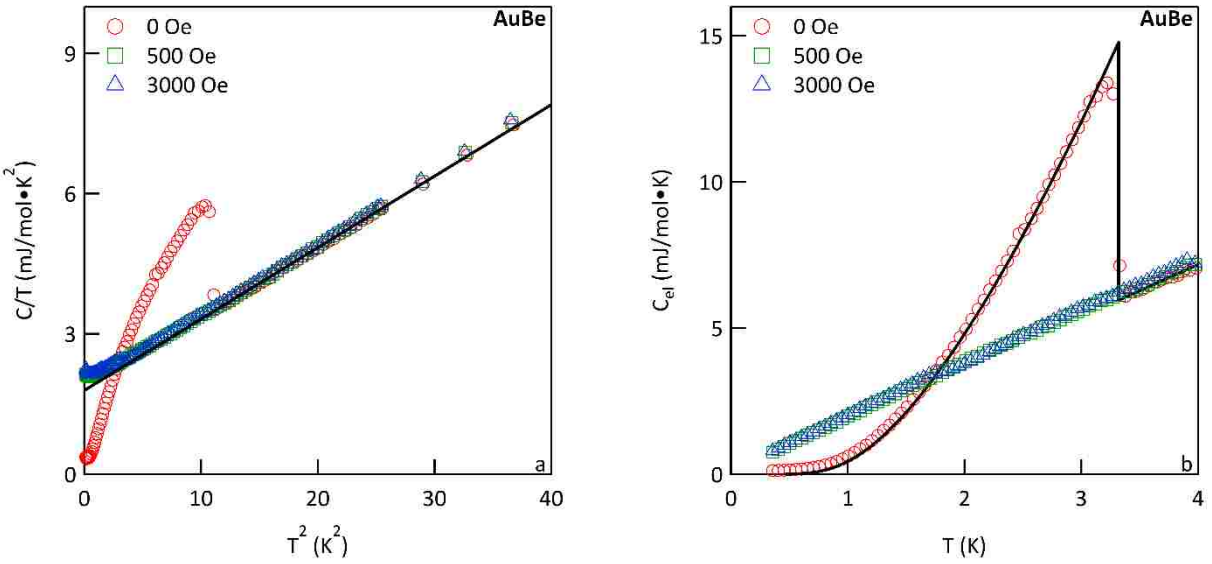


Figure 3.4: (a) Specific heat plotted as C/T vs. $T^2$. (b) Electronic specific heat with BCS fit.

3.32 K giving an energy gap of $\Delta(T = 0\ K) = 1.764k_B(3.32\ K) = 0.505$ meV [2]. The following linear form was fit to the data in the normal state above the critical temperature:

$$C/T = \gamma + \beta T^2.$$

$\beta$ is the coefficient to the phonon contribution of the specific heat, while $\gamma$ is the coefficient for the electron contribution (Sommerfeld parameter). For AuBe, these values were $\gamma$ = 1.79 mJ/mol·$K^2$ and $\beta$ = 0.153 mJ/mol·$K^4$. The phonon contribution to the specific heat ($\beta T^3$) was subtracted from the data, and the plot of the resulting electronic specific heat is given in Figure 3.4b. The ratio of the jump in specific heat to the normal state specific heat ($\Delta C/C_{en}$) was determined to be 1.48 which is comparable to the BCS value of 1.43 [2]. The trend line in Figure 3.4b was generated from the numerical analysis of specific heat in BCS theory from Mühlschlegel and reveals the bulk superconducting state in AuBe to follow the BCS exponential form [33].

Additional information such as the effective electron mass and the Debye temperature for AuBe were calculated from the specific heat data. The determination of these quantities

requires the electron density, *n*, which was determined from Hall effect data to be presented in Section 3.5. For now, the result of $n = 8.36 \cdot 10^{21}$ $cm^{-3}$ will simply be stated and used in the following calculations. Next, consideration is first given to the effective electron mass of which the coefficient of electron heat capacity, $\gamma$, is a measure. An expression for electronic specific heat from the Sommerfeld model is the following:

$$c = \gamma T = \frac{\pi^2}{3} k_B^2 T g(E_F).$$

$g(E_F)$ represents the density of states at the Fermi level and is further defined from the Sommerfeld model as the following:

$$g(E_F) = \frac{m^*}{\hbar^2 \pi^2} (3\pi^2 n)^{\frac{1}{3}}.$$

The sample volume and moles for the data in Figure 3.4a,b were $4.229 \cdot 10^{-9}$ $m^3$ and $2.782 \cdot 10^{-4}$ moles, respectively. The value for m* thus comes to $3.60 \cdot m_o$ where $m_o$ is the free electron mass. This light electron mass places AuBe in the weakly-correlated class of noncentrosymmetric superconductors as expected from chapter 1. The estimated electron density and the coefficient for phonon heat capacity, $\beta$, are next utilized to calculate the Debye temperature from the following expression for phonon heat capacity:

$$c = \beta T^3 = 234 \left(\frac{T}{\theta_D}\right)^3 n k_B.$$

The Debye temperature, $\theta_D$, comes to 139 K.

The superconducting critical values were plotted with a fit of the following BCS form for the superconducting phase boundary:

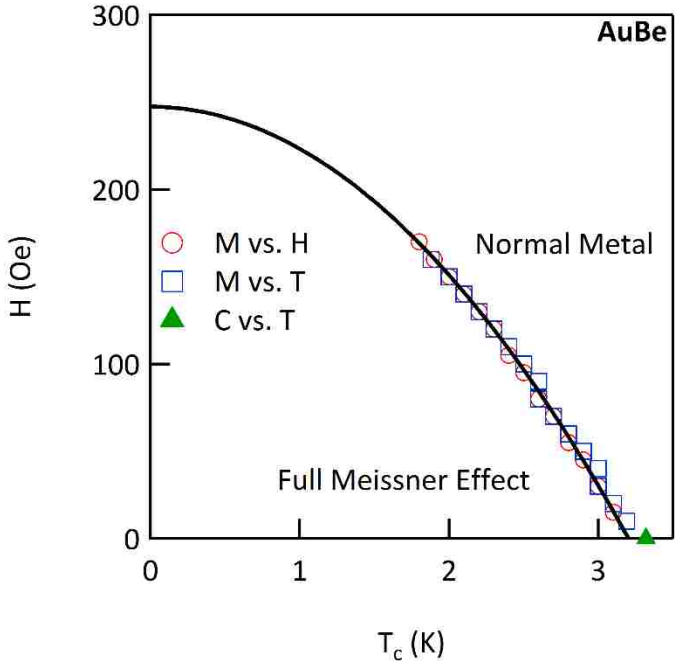


Figure 3.5: Initial AuBe superconducting phase diagram from magnetization and specific heat data.

$$H_c \approx H_c(0)\left(1-\left(\frac{T}{T_c}\right)^2\right).$$

The transitions from magnetization and specific heat previously described in this section are displayed in Figure 3.5 along with a fit of the BCS form to the data. The derived critical values were $T_c$ = 3.20 K and $H_c$ = 247 Oe while $T_c$ = 3.32 K was the critical temperature from specific heat. This difference in $T_c$ is likely due to the use of different samples (one for specific heat, another for magnetization) and could simply be the result of differing internal stress brought about by handling, cutting, and polishing.

The determination of $T_c$ allows for estimation of the energy gap at the Fermi surface, the coherence length, and quantitative assessment of the type of superconductivity present in AuBe. As stated previously, the energy gap in BCS theory is given as $E_g(0) = 2\Delta(0)$ where $\Delta(0) = 1.764k_BT_c$.

Thus, the energy gap comes to $E_g(0)$ = 0.973 meV with $\Delta(0)$ = 0.486 meV ($T_c$ = 3.20 K). Next, the formula for coherence length at T = 0 K is given as the following:

$$\xi_o = \frac{\hbar v_F}{\pi\Delta(0)} = \frac{\hbar^2}{\pi\Delta(0)m^*}(3\pi^2 n)^{\frac{1}{3}}.$$

$v_F$ is the Fermi velocity defined in terms of the Sommerfeld model. With values of m* and n previously described in this section, the value of $\xi_o$ comes to $8.69\cdot10^{-8}$ m. For a quantitative assessment of the superconductivity type, the GL parameter, $\kappa$, defined in chapter 1 as the ratio of the penetration depth to the coherence length requires one further calculation which is an approximation of the penetration depth at T = 0 K from the London equations. This formula (in cgs units) is given as follows:

$$\lambda_L(0) = \sqrt{\frac{m^* c^2}{4\pi n e^2}}.$$

The electron density, n, in this formula represents the superconducting electron density, but as an approximation the electron density from the Hall effect will be used. The value of $\lambda_L$ comes to $1.10\cdot10^{-7}$ m which in turn gives $\kappa = \lambda_L/\xi_o = 1.27$. This value for $\kappa$ falls outside the range for Type I superconductors where $1/\sqrt{2}$ is the upper limit. Thus, the behavior of Type I superconductivity from the sharp superconducting transitions and supercooling in magnetization measurements and a $\kappa$ just above $1/\sqrt{2}$ give indication of a crossover from Type I to Type II superconductivity at lower temperatures.

To conclude this section, plots of magnetization data mentioned in the previous section are presented. A plot of $\chi$ vs. T is given in Figure 3.6 for the Au-Be alloy #2. The superconducting

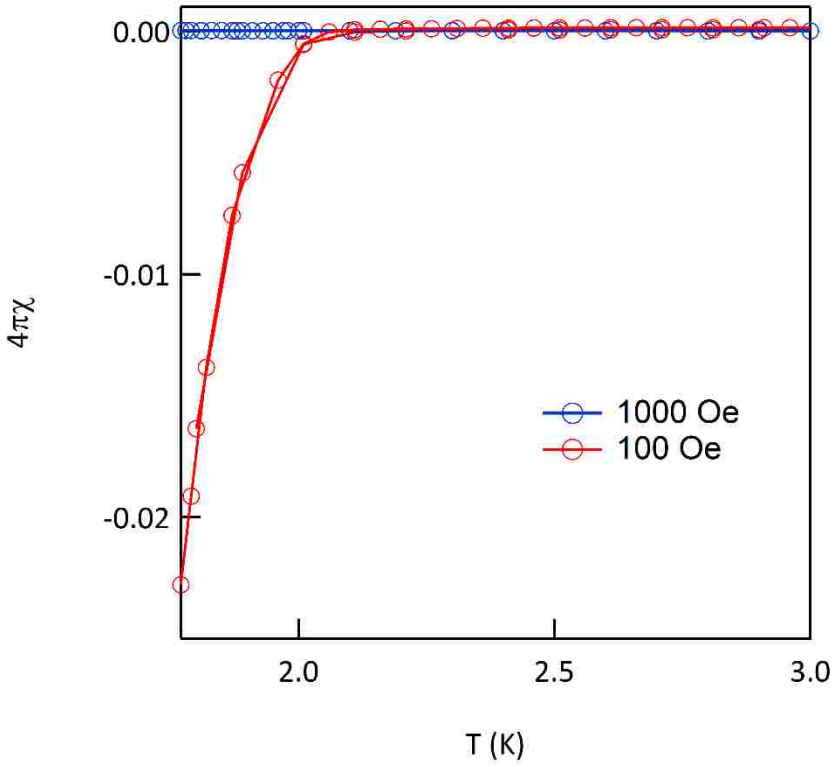


Figure 3.6: $4\pi\chi$ vs. T for Au-Be alloy #2 from dc magnetization data. A full Meissner effect would be $4\pi\chi = -1$.

transition begins just above 2 K at 100 Oe. The source of superconductivity in this sample is not known but is probably due to trace AuBe (or an unknown trace Au-Be alloy). No record of $Au_2Be$ as a superconductor could be found, and Au is well known as a non-superconducting element. Since AuBe was found to harbor trace $Au_2Be$ and the status of $Au_2Be$ as being a normal metal at all temperatures is uncertain, careful consideration was given as to what effect this might have in various measurements. For specific heat, no change in character occurred near 2 K which would indicate a separate small volume of the sample undergoing a superconducting transition. For magnetization measurements, no anomalous jumps occurred in applied field or temperature sweeps which would indicate the presence of a small, separate superconducting volume in the AuBe samples. From these characterization techniques that depend on volume, we came to a

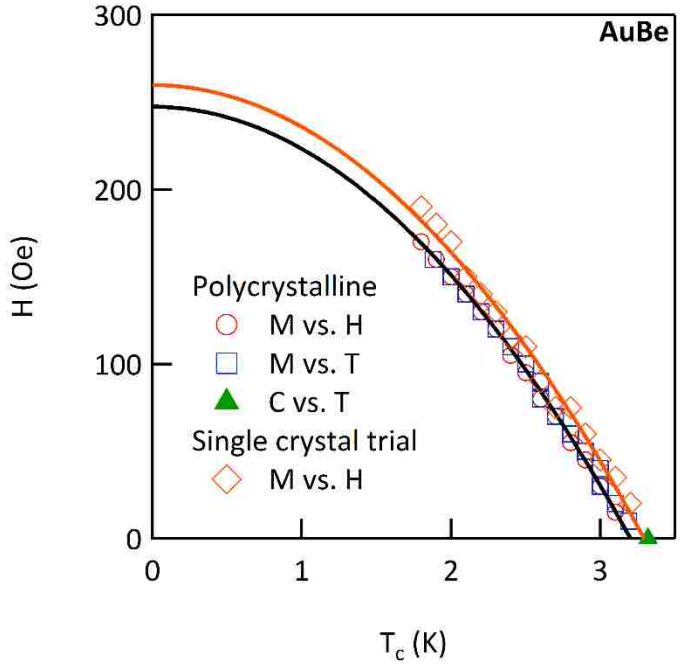


Figure 3.7: Superconducting phase diagram for AuBe single crystal trial.

preliminary conclusion that $Au_2Be$ either was not superconducting or was in such small amount as to be insignificant for investigation of superconductivity in AuBe. Further consideration and analysis of the possible effect of $Au_2Be$ as an impurity are given in the sections to follow.

Figure 3.7 presents the superconducting phase diagram from magnetization data for a polycrystalline AuBe sample identified through powder XRD characterization and the single-crystal AuBe sample. Given the close agreement of the phase boundaries and the unlikelihood of a different Au-Be alloy having the same superconducting phase diagram as AuBe, the single-crystal phase diagram provided supporting evidence that the main phase was AuBe. The single-crystal, cubic character and unit cell dimension were determined from XRD as discussed previously.

### 3.4 ac Susceptibility

The ac susceptibility was employed to further magnetization measurement down to lower temperatures and additionally to serve as a sensitive measure of phase transitions. The first task was to observe how ac susceptibility correlated with the bulk dc magnetization measurement. All of the following data until otherwise stated was obtained with the Quantum Design MPMS described in the previous chapter. Figure 3.8a displays a complete applied field cycle of $\chi'_{AC}$ and M at 1.8 K, and Figure 3.8b displays the same applied field cycle with $\chi'_{AC}$ and $\chi''_{AC}$. The frequency of the $\chi_{AC}$ measurement was 19 Hz and the amplitude was 1 Oe. The real component of ac susceptibility shows a single sharp peak which correlates with the sharp transition in dc magnetization. This peak is commonly referenced in literature as the differential paramagnetic effect (DPE) and is associated with many Type I and soft Type II superconductors. It should be noted that one sample of AuBe showed a DPE peak when magnetic flux entered a sample with applied field cycling but did not show a DPE peak when re-entering the superconducting state. This is attributed to difficulty with flux expulsion associated with supercooling. The imaginary

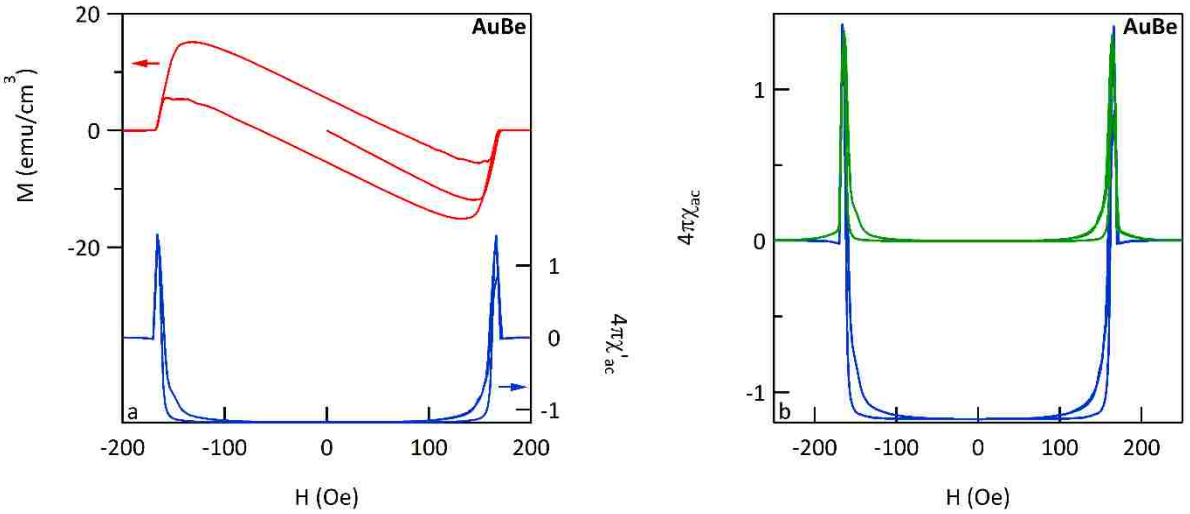


Figure 3.8: AuBe dc magnetization and ac susceptibility. (a) M (red), $4\pi\chi'$ (blue) vs. H. (b) $4\pi\chi'$ (blue), $4\pi\chi''$ (green) vs. H.

component of ac susceptibility in Figure 3.8b displays a single peak which correlates with the superconducting transition in $\chi'_{AC}$ and M. The single peak suggests a single superconducting phase consistent with the Meissner effect in the bulk in agreement with dc magnetization and specific heat measurements.

The effects of frequency and drive amplitude on AuBe ac susceptibility measurements were characterized to determine the sensitivity of the response to these measurement parameters. Figure 3.9a,b displays the real and imaginary components of $\chi_{ac}(\tilde{H}_{ac})$ vs. H at 1.8 K. A frequency of 100 Hz was kept fixed for three measurements with amplitudes $\tilde{H}_{ac}$ = 0.01 Oe, 0.1 Oe, and 1 Oe. Starting at the highest amplitude, a large DPE peak is observed in $\chi'_{ac}$ at the superconducting transition which diminishes to a smoother transition with possibly two inflection points. A large sharp peak is also observed in $\chi''_{ac}$ at the highest amplitude which diminishes with decreasing drive amplitude. However, at the lowest drive amplitude $\chi''_{ac}$ appears to reveal a second broad peak just below 200 Oe in addition to the diminished peak at the critical field. The DPE and first inflection point at lowest amplitude in $\chi'_{ac}$ correlate with the sharp peak

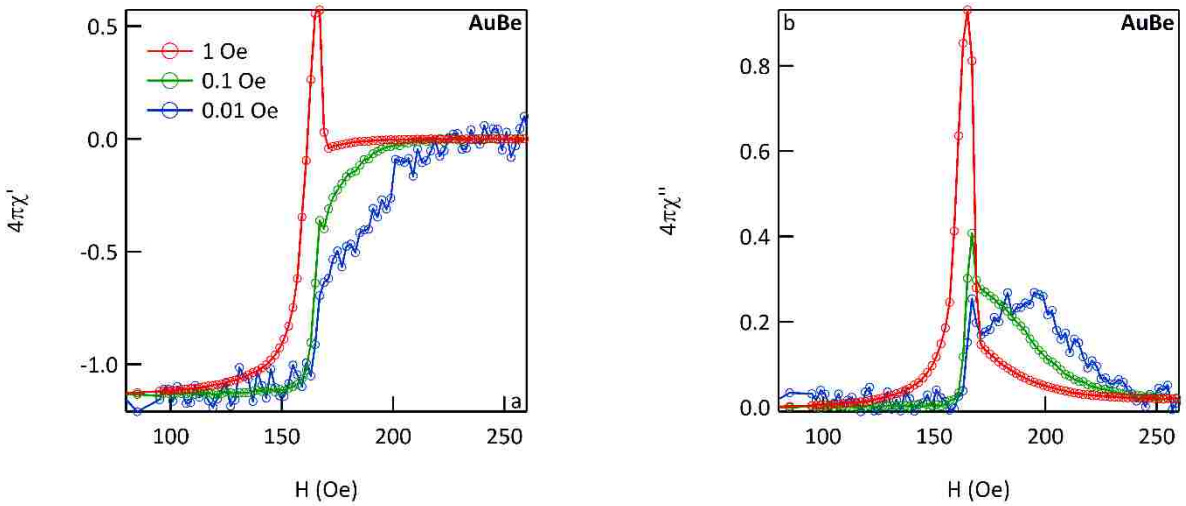


Figure 3.9: AuBe ac susceptibility vs. H as a function of drive amplitude. (a) $4\pi\chi'$ vs. H. (b) $4\pi\chi''$ vs. H.

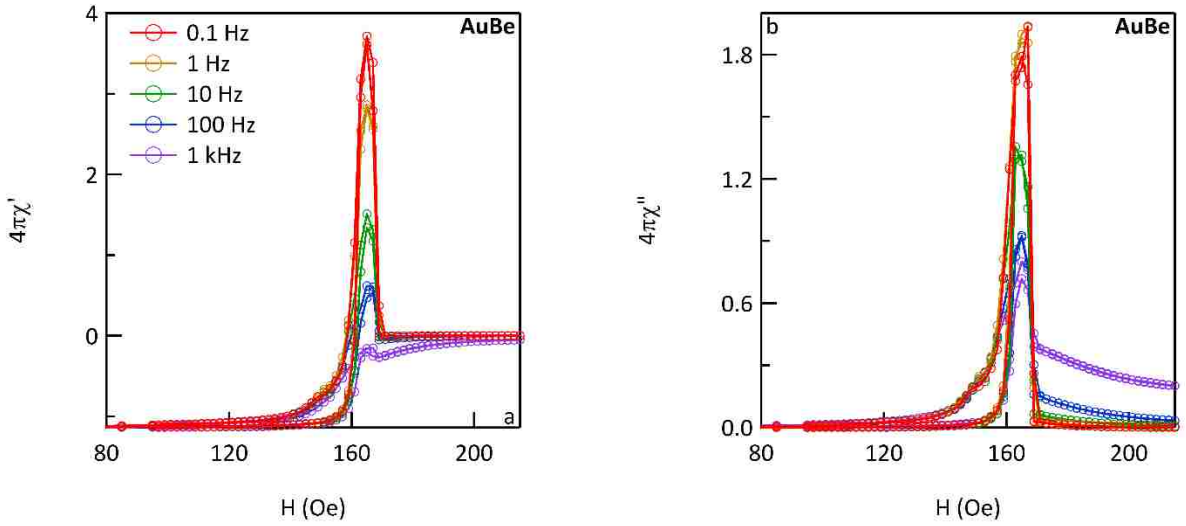


Figure 3.10: AuBe ac susceptibility vs. H as a function of frequency. (a) $4\pi\chi'$ vs. H. (b) $4\pi\chi''$ vs. H.

in $\chi''_{ac}$ while the second inflection point in $\chi'_{ac}$ correlates with the second broad peak in $\chi''_{ac}$. This dependence on amplitude is a curious phenomenon since a DPE peak is indicative of the softness of a material with regard to the expulsion of flux. While the mechanism for this dependence is unknown, perhaps surface pinning associated with supercooling in the intermediate state might account for the behavior.

Next, $\chi_{ac}(f)$ vs. H was analyzed at 1.8 K and the results are displayed in Figure 3.10a,b for the real and imaginary components, respectively. The driving amplitude, $\tilde{H}_{ac}$, of 1 Oe was kept fixed for four measurements with $f$ of 0.1 Hz, 1 Hz, 10 Hz, 100 Hz, and 1 kHz. In $\chi'_{ac}$ a single sharp peak which increases in amplitude as the frequency is decreased is seen at the superconducting transition which is the aforementioned DPE. In $\chi''_{ac}$ a similar behavior is observed with the exception that the peak height saturates below 1 Hz. For the choice of 1 Oe drive amplitude, neither a broadening of the transition in $\chi'_{ac}$ nor a second peak in $\chi''_{ac}$ was observed for the wide range of frequencies measured. Thus, the choice of frequency in the measurement of ac

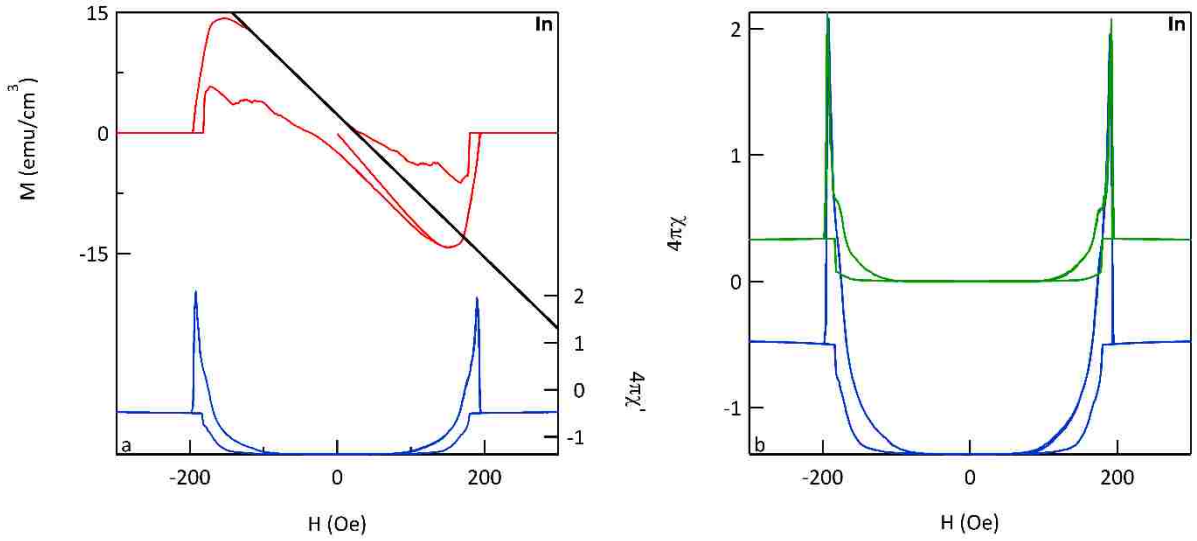


Figure 3.11: Indium dc magnetization and ac susceptibility. (a) M (red), $4\pi\chi'$ (blue) vs. H. Linear fit yields $4\pi(dM/dH) = -1.1$. (b) $4\pi\chi'$ (blue), $4\pi\chi''$ (green) vs. H.

susceptibility appeared only to affect the transition peak magnitude in the real and imaginary components while the shape of the transition in field was observed to be sensitive to the choice of drive amplitude.

A measurement of a typical Type I superconductor was performed to rule out experimental artifacts and provide a standard by which AuBe could be compared. Indium was chosen for comparable critical values to AuBe with an $H_c = 282$ Oe and $T_c = 3.41$ K [17] and was cut in similar fashion and shape to the AuBe samples (elongated bar). Figure 3.11a displays a complete applied field cycle of $\chi'_{AC}$ and M at 1.8 K, and Figure 3.11b displays the same applied field cycle with $\chi'_{AC}$ and $\chi''_{AC}$. Similarity with AuBe is seen in magnetization in that hysteresis is observed with sharp transitions at the critical field. One small difference was that supercooling in the indium sample was more pronounced. $\chi'_{AC}$ exhibited a DPE peak for magnetic flux inclusion, but no DPE peak for magnetic flux expulsion upon re-entry to the superconducting state. The offset superconducting transitions in $\chi'_{AC}$ manifested by the DPE peak and peakless

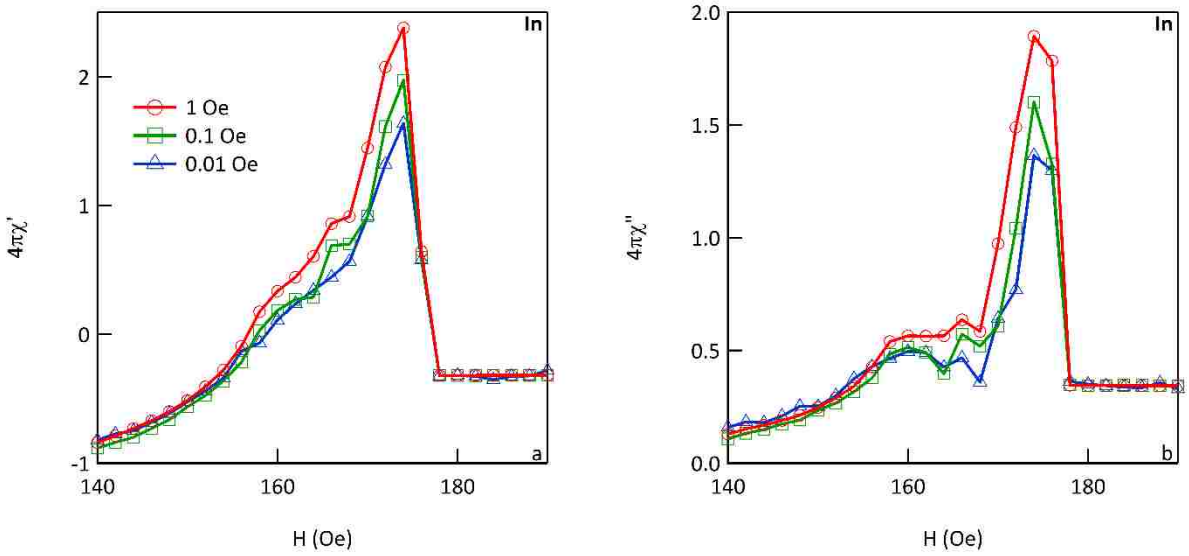


Figure 3.12: Indium ac susceptibility vs. H as a function of drive amplitude. (a) $4\pi\chi'$ vs. H. (b) $4\pi\chi''$ vs. H.

transition correlate with the corresponding superconducting transitions in $\chi''_{AC}$ and dc magnetization.

Further characterization of In was performed in ac susceptibility by varying drive amplitude, $\tilde{H}_{ac}$, and frequency, *f*, of applied field sweeps as was done for AuBe. Figure 3.12a,b displays the real and imaginary components of $\chi_{ac}(\tilde{H}_{ac})$ vs. H at 2 K and 10 Hz. In $\chi'_{AC}$ a DPE peak is observed for all amplitudes, $\tilde{H}_{ac}$, with marginal peak decrease for smaller amplitudes. In $\chi''_{AC}$ a large peak is observed at the superconducting transition plus an additional low lying broad peak at lower field. This small broad peak correlates with a broadening of the DPE peak in $\chi'_{AC}$ and most likely exists as a granular effect. Figure 3.13a,b displays the real and imaginary components of $\chi_{ac}(f)$ vs. H at 2 K and 1 Oe. In $\chi'_{AC}$ a DPE peak is observed for all frequencies and diminishes with increasing frequency. The broad lower-field bump attributed to a granular effect also diminishes with increasing frequency. In $\chi''_{AC}$ a large peak is observed at the superconducting

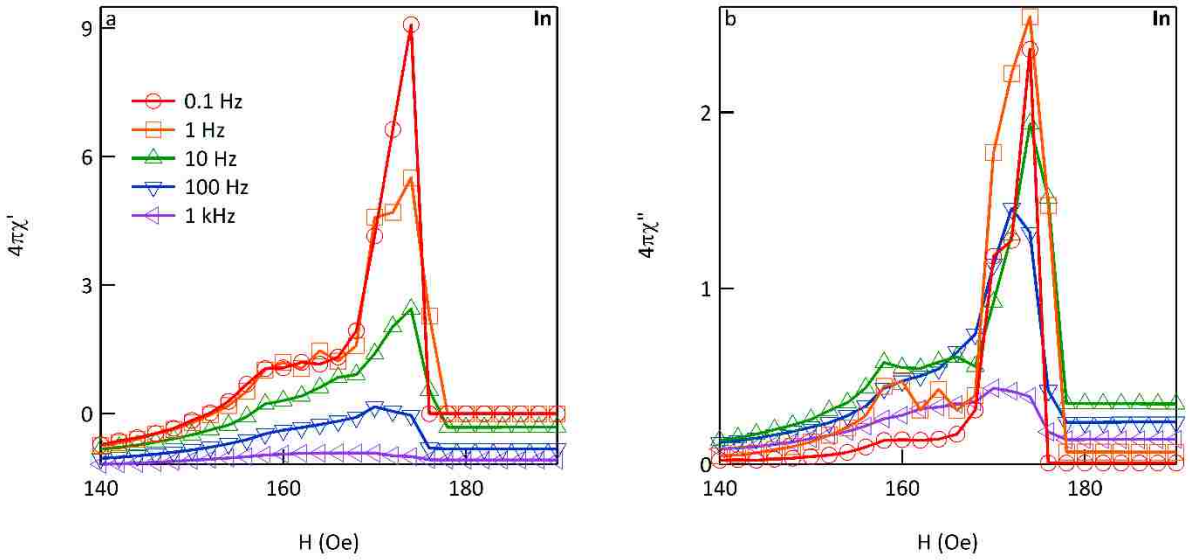


Figure 3.13: Indium ac susceptibility vs. H as a function of frequency. (a) $4\pi\chi'$ vs. H. (b) $4\pi\chi''$ vs. H.

transition, and as before a small broad peak at lower field is observed. Both peaks decrease in magnitude with increasing frequency with possible saturation of the peaks below 0.1 Hz.

Comparison of the AuBe and In data revealed that most features of the AuBe magnetization and ac susceptibility data are reproduced in the simple, well-characterized elemental Type I superconductor In. Hysteresis in an applied field cycle and a DPE peak in $\chi'_{AC}$ appear as classic features of Type I superconductivity. Indium and one of the AuBe samples showed a clipping of the DPE peak upon magnetic flux expulsion within the applied field cycle most likely associated with greater supercooling. One difference between these materials was the disappearance of the DPE peak in AuBe $\chi'_{AC}$ with decreasing drive amplitude while In maintained the DPE peak for all drive amplitudes. However, the trend of the $\chi'_{AC}$ DPE peak in In was to decrease with decreasing drive amplitude which gives us some confidence that the same effect exists for both compounds but is more pronounced in AuBe. Since the response to higher drive amplitude in ac susceptibility best mirrored the sharp superconducting transitions seen in

AuBe dc magnetization and was observed to not produce abnormalities in the In characterization, further ac susceptibility measurements on AuBe were performed at the higher drive amplitude (1 Oe, 19 Hz).

The ac susceptibility was further characterized in isothermal field sweeps at increments of 0.1 K for the purpose of obtaining field and temperature data for the phase diagram. The temperature range of the isothermal field sweeps was extended by use of the He-3 cryostat described in the previous chapter. As the bore of the susceptometer in the He-3 cryostat was significantly smaller than the MPMS sample chamber, a smaller piece of AuBe was cut from the original sample run in the MPMS which introduced a somewhat different demagnetization factor and different stresses in the bulk. Thus we expected some minor differences between measurements in the two systems but still enough information for the phase diagram and qualitative analysis. Both sets of data were taken at 19 Hz. While the MPMS was set on the calibrated amplitude of 1 Oe, the susceptometer for the He-3 cryostat was uncalibrated, and the primary coil amplitude, $\widetilde{H}_{ac}$, was set so as to produce the recognizable DPE peak in $\chi'_{ac}$. The He-3 cryostat data was then normalized to the MPMS data in the superconducting state. A difference in magnitudes between the two sets of data remained due to the unmatched drive fields. With these qualifications in mind, Figure 3.14a,b displays $\chi'_{ac}$, $\chi''_{ac}$ vs. H which includes both the MPMS data and He-3 cryostat data. The high temperature range representing the data from the MPMS appears the same in character as the previous ac susceptibility data for AuBe presented in this section. However, the low temperature range representing the data from the He-3 cryostat reveals a crossover in behavior at approximately 1.2 K where the DPE peak in $\chi'_{ac}$ disappears and the superconducting transition broadens. In $\chi''_{ac}$ the transition peaks also appear

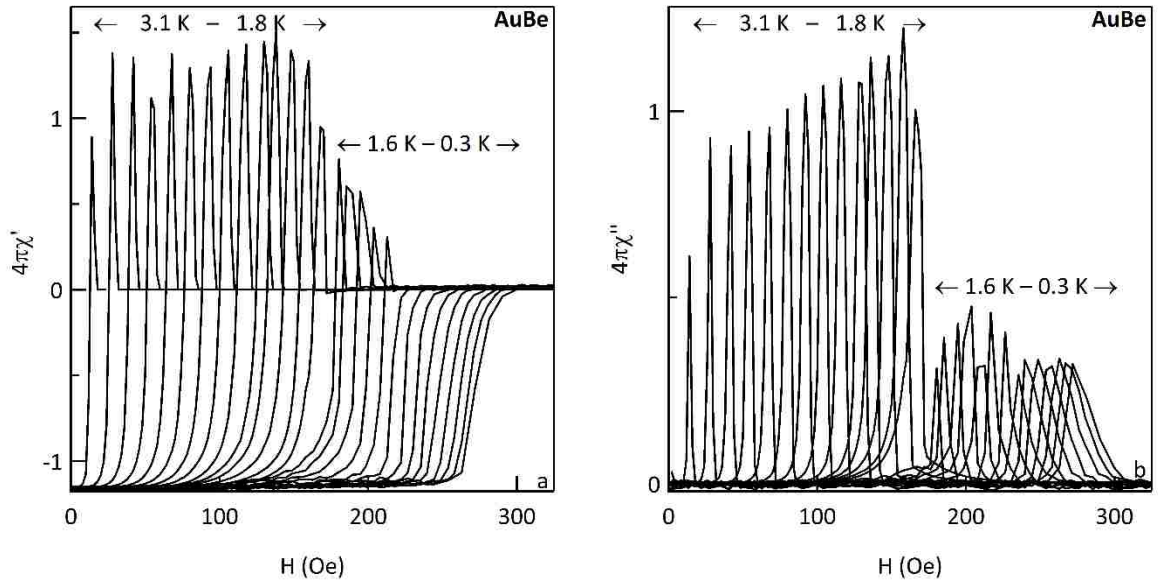


Figure 3.14: AuBe ac susceptibility vs. H. (a) Real component, $4\pi\chi'$ vs. H. (b) Imaginary component, $4\pi\chi''$ vs. H.

broader past this transition compared to the peaks at higher temperature. To confirm this crossover, the measurements at 1.1 K and 1.2 K were repeated as a function of drive amplitude.

Previous characterization of amplitude and frequency settings in ac susceptibility with the MPMS revealed anomalous behavior as a function of drive amplitude. Additionally, the anomalous change in character of the superconducting transition was evident between two orders of magnitude of the drive amplitude. Despite not being calibrated, a change in the order magnitude of the drive amplitude was possible through control of its power source (constant voltage source). Thus, qualitative analysis and comparison with MPMS amplitude data was possible. Figure 3.15a,b displays the real and imaginary components of $\chi_{ac}$ vs. H at 1.1 K for drive amplitude as a function of voltage source ranging from 0.01 V to 0.1 V. No DPE peak in $\chi'_{ac}$ was observed for any of the drive amplitudes from these voltages. A single peak in $\chi''_{ac}$ was observed for all amplitudes indicating no additional contributions to the superconducting transition. Figure

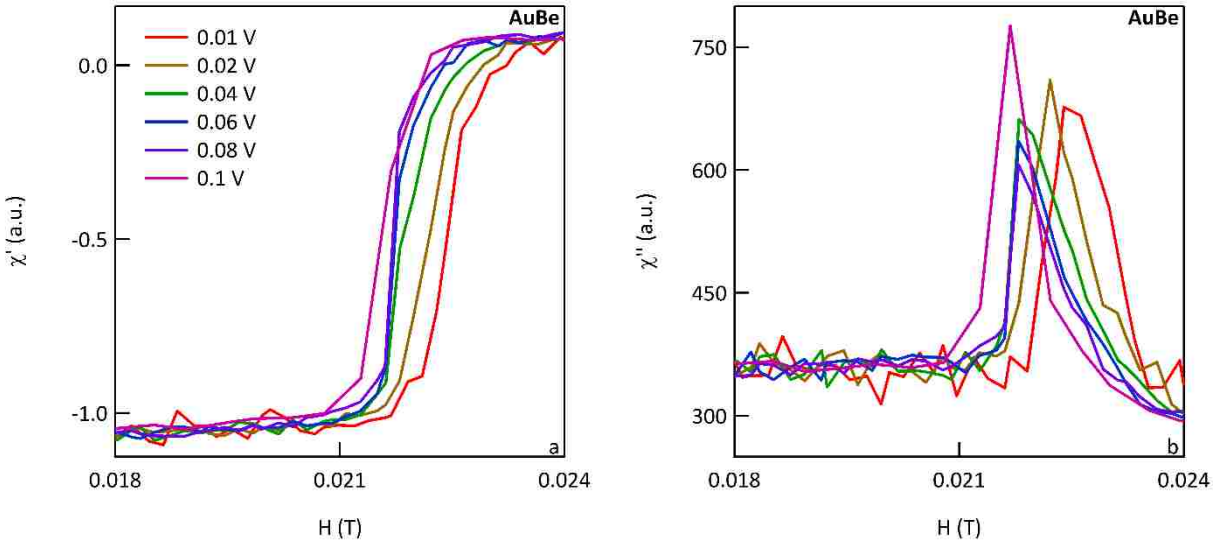


Figure 3.15: AuBe ac susceptibility vs. H at 1.1 K. (a) Real component, $\chi'$ vs. H. (b) Imaginary component, $\chi''$ vs. H.

3.16a,b displays the real and imaginary components of $\chi_{ac}$ vs. H at 1.2 K for drive amplitude as a function of voltage source ranging from 0.01 V to 0.1 V. The lowest voltages corresponding to lowest drive amplitudes show broad transitions in $\chi'_{ac}$ which at the highest field transforms to a DPE peak. As with the previous temperature, a single peak in $\chi''_{ac}$ was observed for all amplitudes indicating no additional contributions to the superconducting transition. As evident from Figures

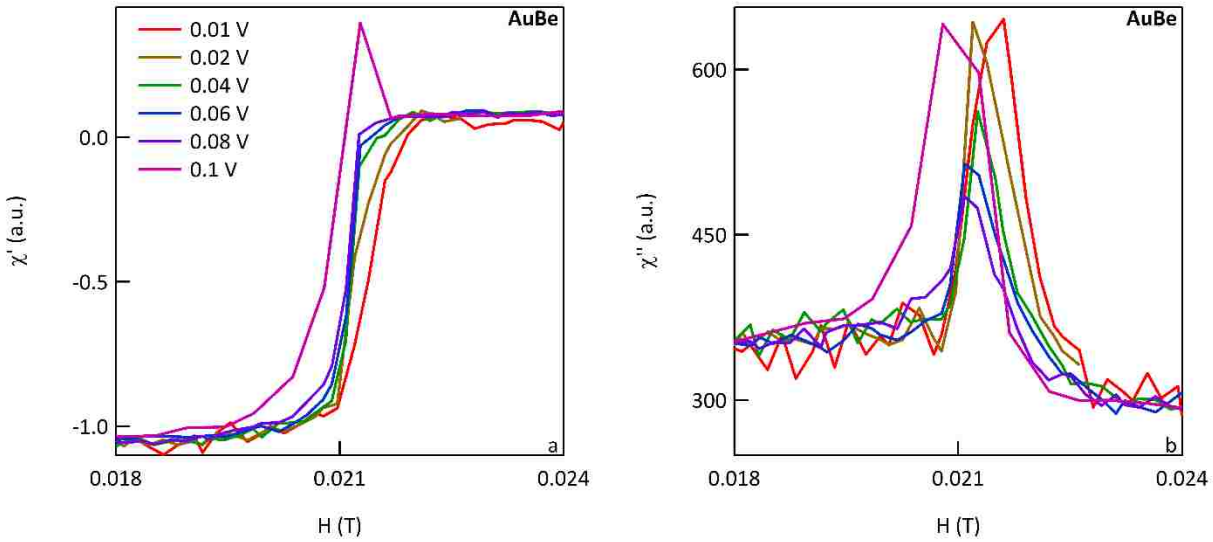


Figure 3.16: AuBe ac susceptibility vs. H at 1.2 K. (a) Real component, $\chi'$ vs. H. (b) Imaginary component, $\chi''$ vs. H.

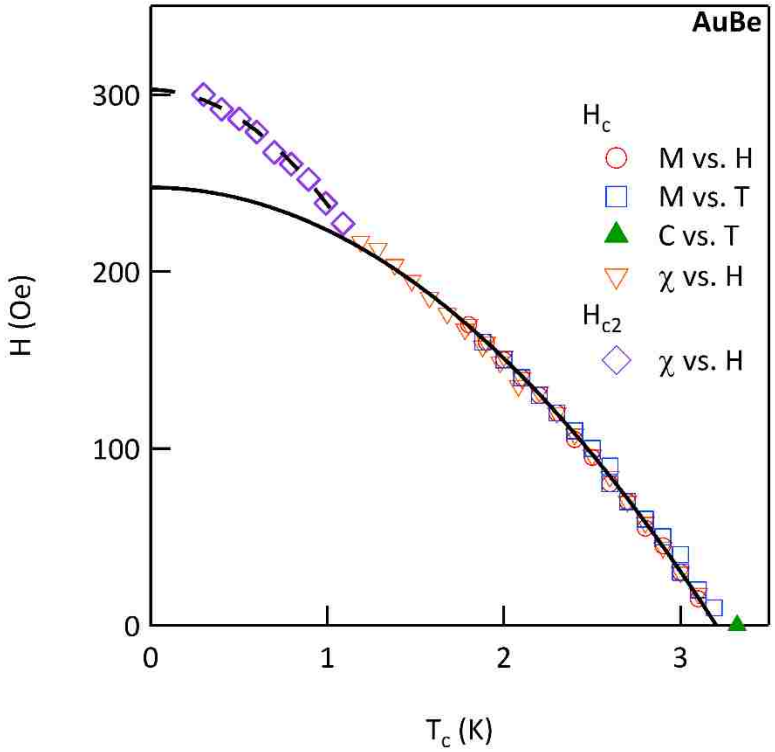


Figure 3.17: AuBe superconducting phase diagram updated with ac susceptibility transition points.

3.15a and 3.16a, the crossover from DPE peaks to broad transitions exists independent of the amplitude setting although the exact crossover position in temperature bears some dependence on the amplitude setting. While the previously observed broadening of the superconducting transition was questionable, broadening of the transition independent of amplitude setting strongly implies the formation and movement of magnetic flux within the superconducting volume. Thus, a picture emerges of AuBe undergoing a crossover in superconductivity from Type I to Type II as temperature is lowered through 1.2 K.

The set of superconducting transitions from ac susceptibility was added to the phase diagram for AuBe. The superconducting transition was defined as the field at the base of the DPE peak on the normal state side. For the non-peaked transitions, the superconducting transition was judged at the turning point in field for the onset of superconductivity. Figure 3.17 displays

the superconducting phase diagram for AuBe updated with the transition points from ac susceptibility. The change in character of the superconductivity in AuBe is further highlighted by the divergence of the phase boundary from the BCS form which closely fits the section of the phase diagram pertaining to Type I superconductivity. A separate fit of the BCS form was applied to the divergent section of the phase boundary which yielded the critical field, $H_{c2}$ = 303 Oe. The following equation was then applied to obtain $\kappa$:

$$H_{c2} = \sqrt{2}\kappa H_c.$$

Inserting the previous experimental-fit value of 247 Oe for $H_c$, the value for $\kappa$ came to 0.867 which is lower than the $\kappa$ derived in the last section ($\kappa$ = 1.27) but still slightly higher than $1/\sqrt{2}$.

This section concludes the characterization for magnetic properties of the superconducting state in AuBe. The magnetic measurements in dc magnetization and ac susceptibility revealed AuBe to exhibit typical Type I superconducting behavior at temperatures near $T_c$, but as the temperature range was extended to lower temperatures in ac susceptibility, a crossover point was observed both in the type of response in ac susceptibility and in the superconducting phase boundary defined by the onset of superconductivity. In the next section, resistivity data on the superconducting transition in AuBe is presented giving a different but complementary probe of superconductivity at the surface of the material.

**3.5 Resistivity**

The rare phenomenon of a crossover point in the type of superconductivity observed in ac susceptibility data presents an intriguing question as to what to expect for electron transport behavior at the crossover. As discussed in chapter 1, typical behavior for a Type I superconductor

is a sharp transition at $H_c$ while for a Type II superconductor, the superconducting transition has width due to the nature of the intermediate state. Superconductivity in a surface sheath is possible with both types of superconductivity and is described by the following limiting formula from Ginzburg-Landau theory:

$$H_{c3} = 1.695H_{c2} = 1.695\sqrt{2}\kappa H_c.$$

The effect of the surface sheath superconductivity on measurement is different between Type I and Type II superconductivity. Type I superconductors display hysteresis in the superconducting transition with $H_{c3}$ as a limit on the transition shift from $H_c$. Type II superconductors do not display hysteresis in the superconducting transition, and $H_{c3}$ can be measured at a superconductor's surface by electron transport techniques. With these characteristic behaviors of Type I and Type II superconductors as reference, we investigated the superconducting transition of AuBe using resistivity as a sensitive probe of superconducting currents.

Isothermal measurement of resistivity in applied field sweeps is displayed in Figure 3.18a,b. Resistivity in the plot was normalized by the resistivity in the normal state above the superconducting transition with the 0.4 K to 2.5 K range measured in the He-3 cryostat and 2.8 K to 3.2 K measured in the MPMS. The data for the displayed superconducting transitions in Figure 3.18a was produced by sweeping applied field from the superconducting state to normal state at the transition. Figure 3.18b was produced by sweeping the applied field low-high-low across the superconducting transition. The nature of the transition widths follow expectation in that the temperature range described as Type I from the previous section reveals transitions with a distinct sharpness. This sharp character gives way to broader transitions as the crossover at ~1.2

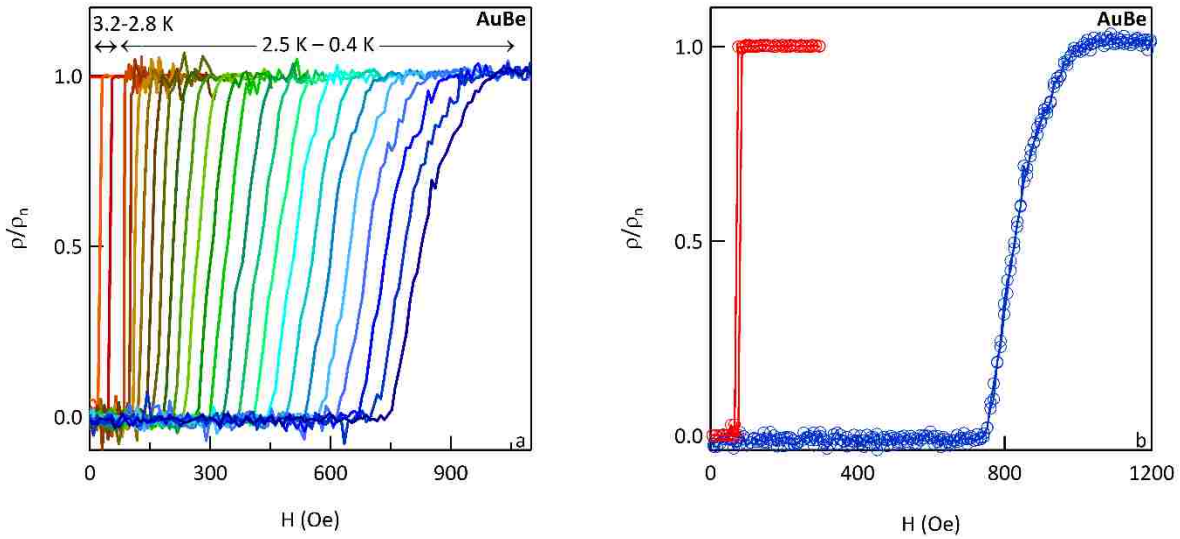


Figure 3.18: AuBe resistivity normalized to the normal state above the superconducting transition. (a) Isothermal resistivity sweeps revealing the robust nature of the transition at low temperature and broadening of the transition. (b) Cycling of the field at 2.6 K (red) reveals a small supercooling effect while at 0.4 K (blue) no supercooling is observed.

K is approached and traversed. Figure 3.18b provides evidence of Type I superconductivity in the high temperature range since the field sweep in resistivity produced hysteresis (supercooling). The field sweep at low temperature produced no discernable hysteresis consistent with behavior for Type II superconductivity. While the width of the transitions and hysteretic nature followed expectations for the respective types of superconductivity, the field positions of the surface superconducting transitions at low temperature far exceeded expectations from Ginzburg-Landau theory and ($H_c$, $H_{c2}$) determined from magnetization and ac susceptibility data in the last section.

Figure 3.19 displays the AuBe superconducting phase diagram updated with the critical field transition points from resistivity characterization. The surface transition points track with the phase boundary at higher temperatures in the region characteristic of Type I

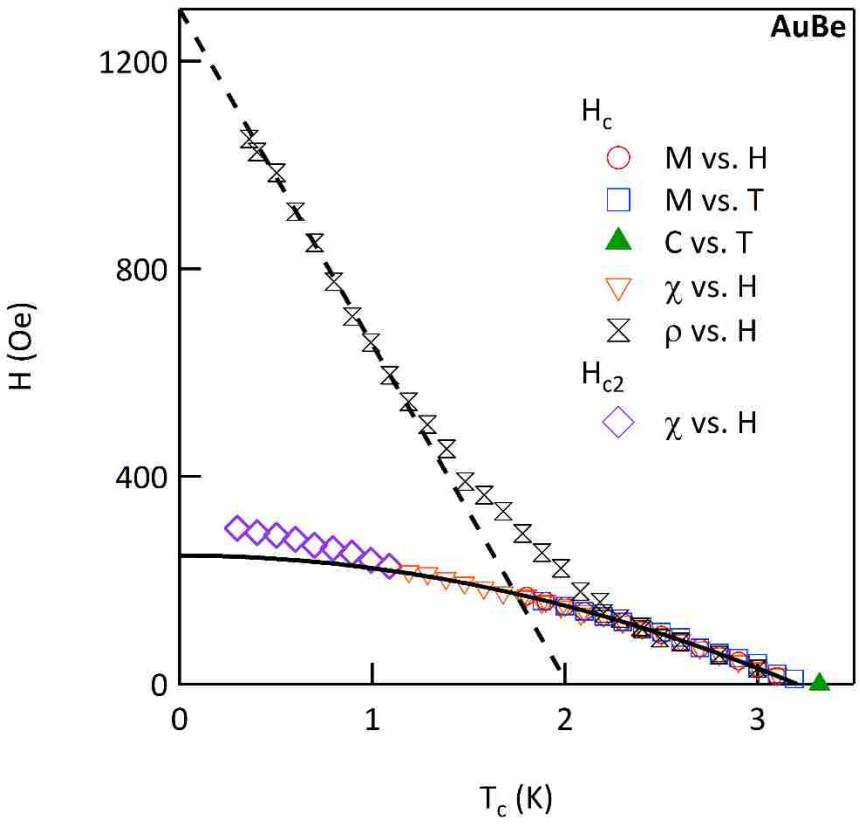


Figure 3.19: AuBe superconducting phase diagram updated with transitions from resistivity measurement.

superconductivity. However, as temperature is reduced towards the Type II region, the surface transition points diverge from the previously established phase boundary and establish an uncharacteristic upward trend that appears linear (dashed line in Figure 3.19). As the divergence of the surface transition occurs far from $T_c$, correlation between the divergence of the surface transitions and the crossover to Type II superconductivity is inferred.

While a microscopic probe of the surface superconductivity was beyond the capabilities of this dissertation project, a well-established technique for destroying the surface superconductivity was accessible. A magnetic metal deposited on the surface of a superconductor acts as a pair-breaking mechanism which effectively inhibits surface

superconductivity. We picked Cr to deposit on AuBe since as an antiferromagnetic non-superconducting metal, it should provide a very effective pair-breaking mechanism. Additionally, Cr is easy to thermally evaporate which was the deposition system at our disposal. The AuBe sample was in the shape of an elongated slab, and Cr was deposited on every side with approximately 30 nm on the top and approximately 10 nm on the other surfaces. Isothermal field sweeps of resistivity measurement similar to what was performed for Figure 3.18 were performed on the sample. No diminishing of the surface superconducting transition was observed. In order to verify this extraordinary result, the experiment was repeated in collaboration with Dr. Philip Adams and performed by Dr. Abhishek Pandey. For this second trial, a different piece of AuBe was coated with Cr by electron beam deposition to a thickness of approximately 5 nm on all four long sides of the AuBe bar shape. One difference between this trial and the first trial was that in the first trial lead attachment was performed after Cr deposition and in the second trial lead attachment was performed before Cr deposition. The results are displayed in Figure 3.20 and confirm the robust nature of the resistivity superconducting transition in AuBe. The implications of the survival of the superconducting transition measured by resistivity measurement are twofold. Either a robust superconducting state exists on the surface of AuBe at low temperature or a filamentary superconductivity exists in the bulk.

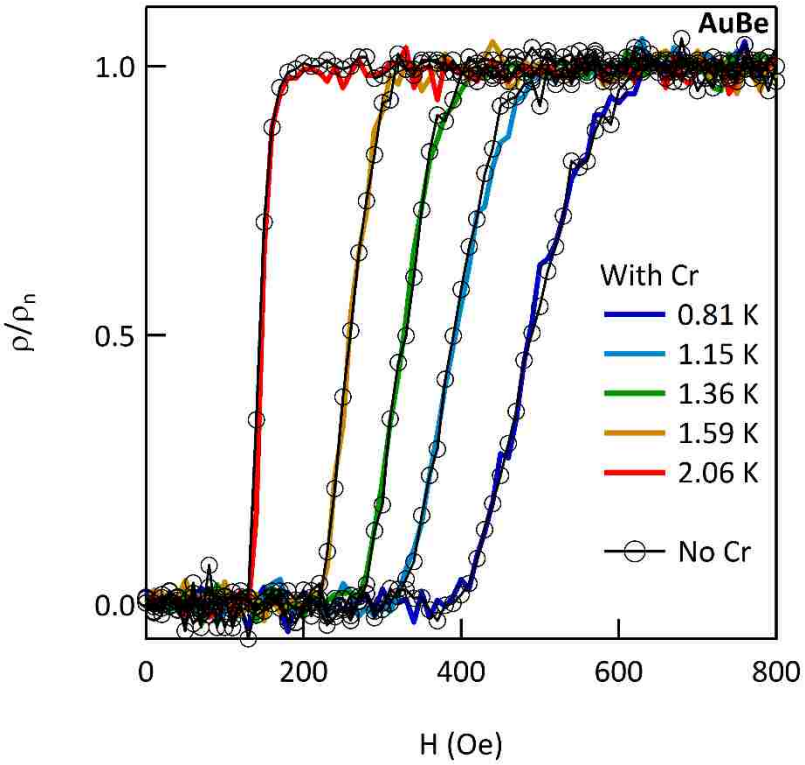


Figure 3.20: AuBe-Cr resistivity (color) normalized to the normal state above $T_c$. Corresponding measurement with Cr removed indicated with overlaid black icons.

### 3.6 Hall Effect and Magnetoresistance

Other electron transport measurements were performed on AuBe which are the topic of this section. Hall effect characterization was performed to determine the charge carrier type and density for approximation of the characteristic lengths for the superconducting properties. In addition, the magnetoresistance was explored. Figure 3.21 displays Hall voltage vs. applied field. The charge carrier type was determined to be electron-like with a density of $8.36 \cdot 10^{21}$ $cm^{-3}$.

The magnetoresistance of AuBe up to 7 T was characterized at 1.8 K and is displayed in Figure 3.22. A large positive magnetoresistance of approximately 60% at 7 T was observed.

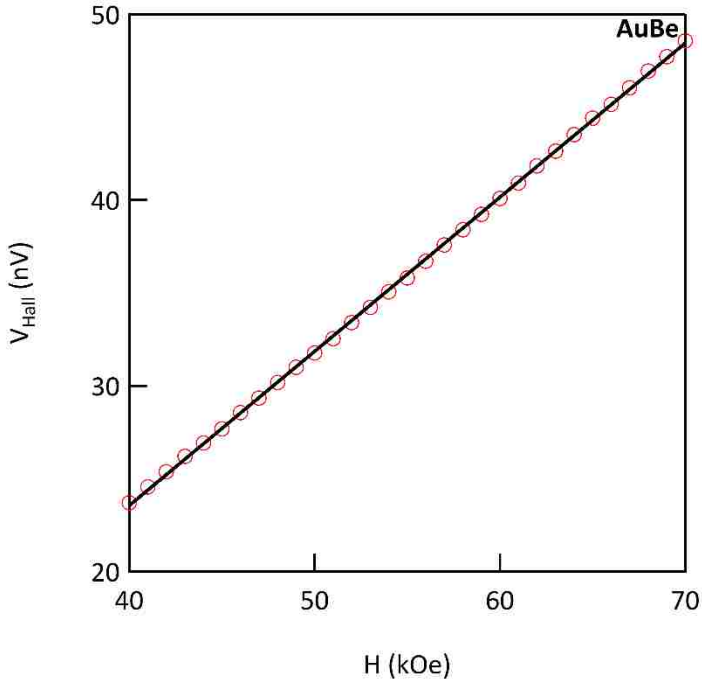


Figure 3.21: Hall voltage vs. applied field (red icons). A linear fit yielded a slope of $8.297 \cdot 10^{-13}$ V/Oe.

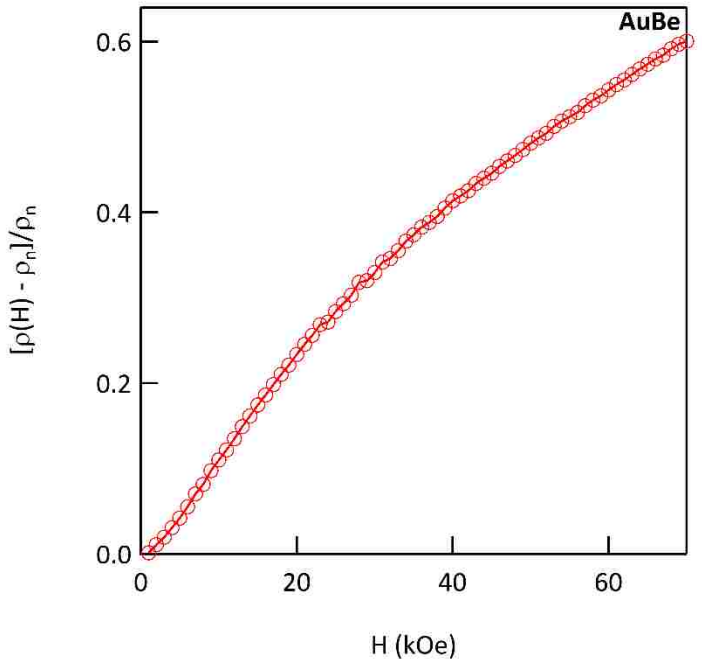


Figure 3.22: Magnetoresistance plotted as percent difference from the resistivity of the normal state above $T_c$.

### 3.7 de Haas-van Alphen Effect

In a rather serendipitous turn of events, what at first appeared as noise in high-field magnetization measurements of polycrystalline AuBe in the MPMS turned out to be de Haas-van Alphen (dHvA) oscillations thus opening an avenue of investigation into the electronic structure of AuBe. The fact that dHvA oscillations were observed at all in polycrystalline samples of AuBe gave indication of a spherical Fermi surface since different crystallite orientations would average out contributions from non-spherical parts of the Fermi surface. Figure 3.23a displays normalized magnetization vs. inverse applied field, and Figure 3.23b displays the fast Fourier transform (FFT). While all AuBe samples showed low frequency oscillations, the data in Figure 3.23a was from the AuBe sample annealed for the longest duration (6 days) which showed unique higher frequencies that were not simply harmonics of the low frequencies. Figure 3.24 displays the FFT from Figure 3.23b with frequencies converted to estimated energies using the Sommerfeld model and

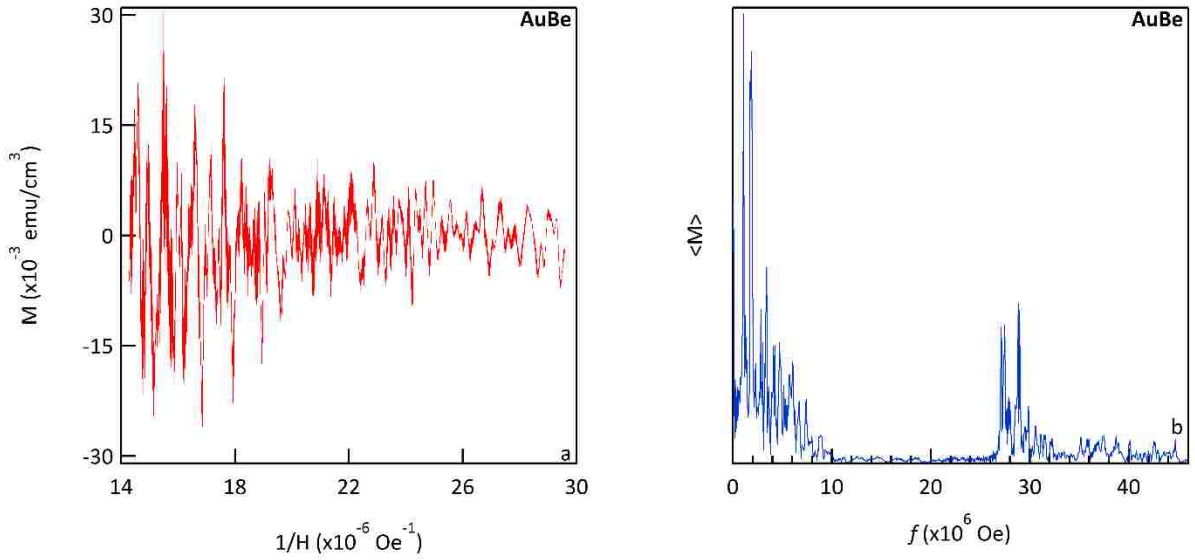


Figure 3.23: Analysis of de Haas-van Alphen oscillations in AuBe. (a) Normalized magnetization plotted as M vs. 1/H. (b) Fast Fourier Transform (FFT) of the normalized magnetization data.

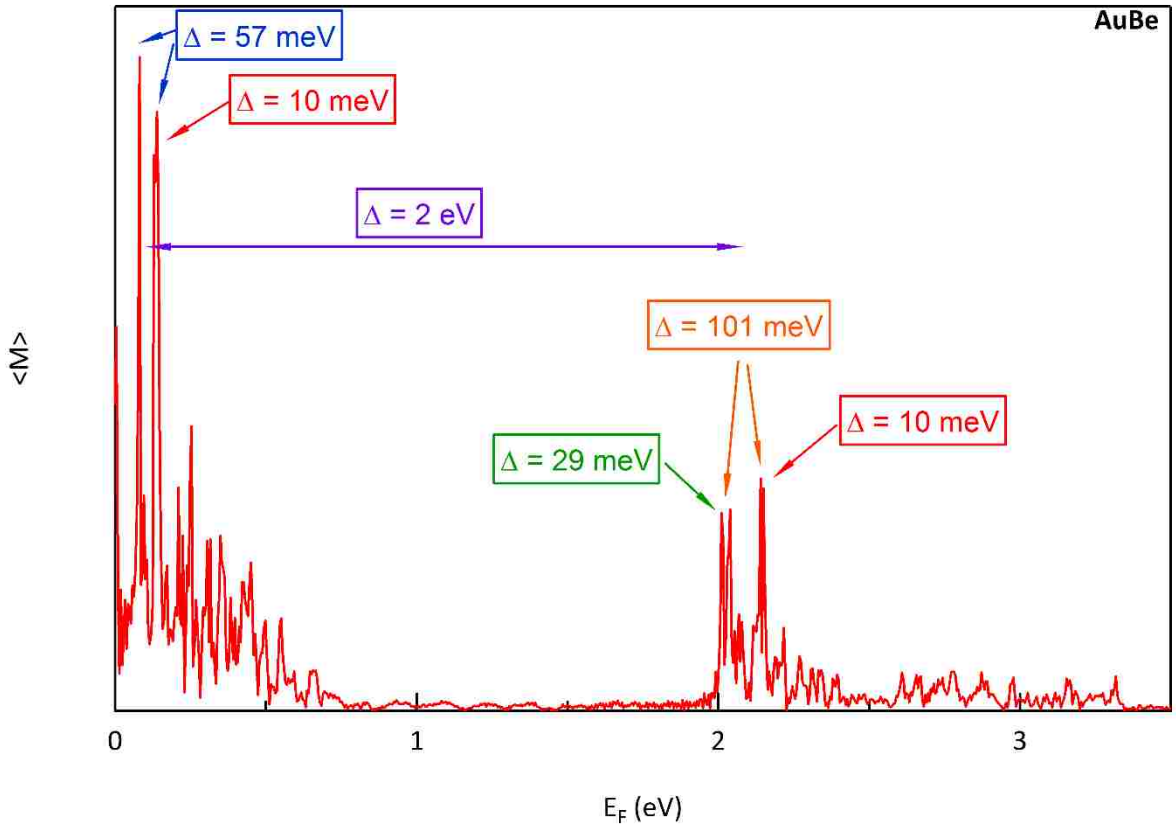


Figure 3.24: FFT components in terms of energy (eV) instead of frequency (Oe).

spherical approximation of the Fermi surface. The labels in the figure display differences in peak energies for comparison between the parts of the Fermi surface.

Further MPMS characterization revealed another extraordinary quality of the dHvA oscillations. The amplitude of the oscillations died out at relatively high temperature (~30 K) which is unusual since high quality single crystals at very low temperatures are typically required for dHvA characterization. This provided opportunity to measure the effective electron mass for the spherical Fermi surface accessible from MPMS measurement. A large low frequency oscillation was selected for measurement, and isothermal field sweeps of magnetization were measured from 2 K to 26 K. The amplitude (A) of each sweep was determined and plotted with

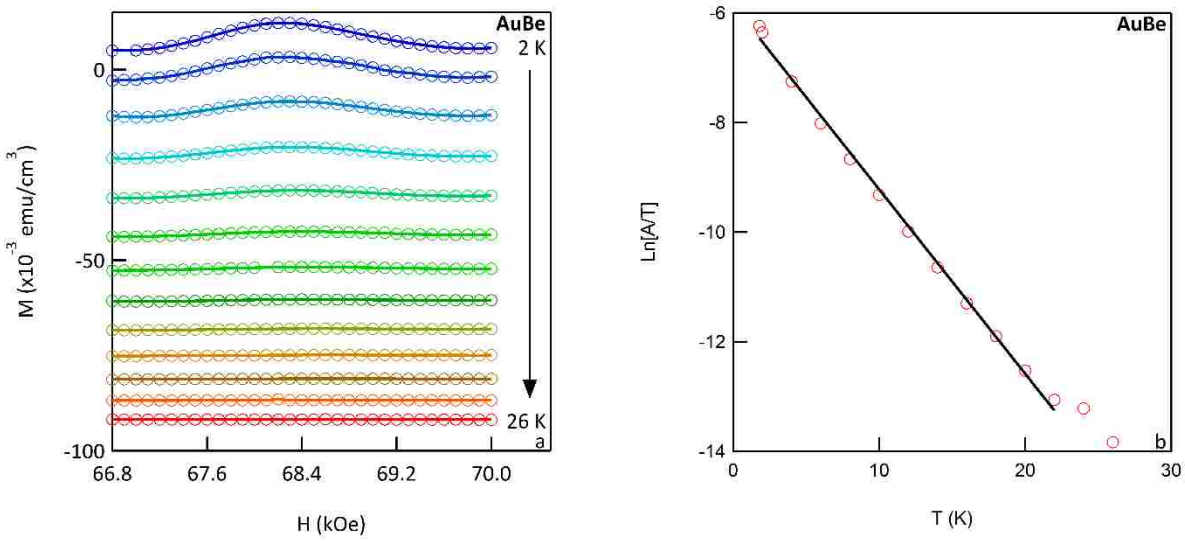


Figure 3.25: (a) Temperature dependence of a single dHvA oscillation in M vs. H. (b) Determination of the effective electron mass from the logarithmic relationship of dHvA amplitude and temperature.

temperature (T) using the relationship, ln(A/T) vs. T, from Shoenberg [34]. The effective mass was determined from the slope which is given by the relationship, $-1.47 \cdot 10^5 (m/m_o)T/H$, where H is applied field (cgs units). Figure 3.25a displays the amplitude dependence in magnetization, and Figure 3.25b displays the fit for effective mass yielding a value of $m = 0.16\ m_o$. This effective electron mass was used for the determination of energies in Figure 3.24. Comparison with the effective electron mass of $m^* = 3.60 \cdot m_o$ from specific heat and Hall effect data shows that while the effective electron mass averaged over all the Fermi surface is light, there exists a small spherical piece of the Fermi surface with an effective electron mass more than an order magnitude smaller.

The dHvA and the Fermi surface of AuBe was further characterized in collaboration with Dr. John Singleton at the National High Magnetic Field Laboratory at Los Alamos National Laboratory. The small single crystal of AuBe proved too small for the attempted techniques so

one of the polycrystalline samples was characterized. The FFT of this data is displayed in Figure 3.26 where $\chi(1/H)$ was sampled in increments of 0.003 $T^{-1}$. Figure 3.26a displays the frequencies for AuBe and shows harmonics in fundamental frequencies of the Fermi surface. Figure 3.26b plots the data with a zoomed-in view of the lower frequencies. The red highlighted data reveal a low frequency peak arising after 40 T and represents a transition in the Fermi surface of AuBe past 40 T. The nature of this change in the Fermi surface is not currently understood.

This section concludes with calculations of the band structure and Fermi surface of AuBe in collaboration with Dr. Dana Browne and his student, Jordan Ball, for comparison to our dHvA data. The WIEN2K all-electron LAPW electronic structure package with the Perdew-Wang GGA

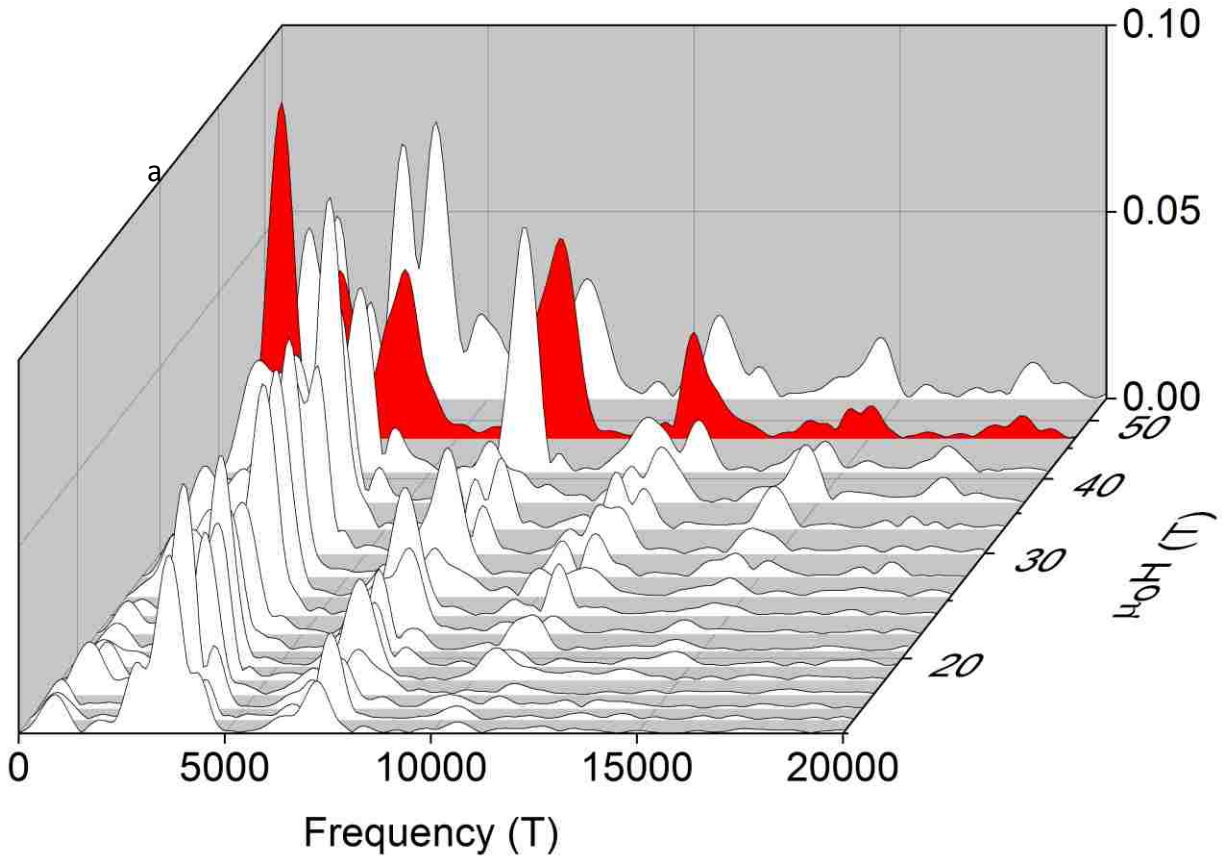


Figure 3.26: AuBe high-field dHvA oscillations with red data highlighting the change in the Fermi surface. (a) Broad frequency range. (b) Zoomed view.

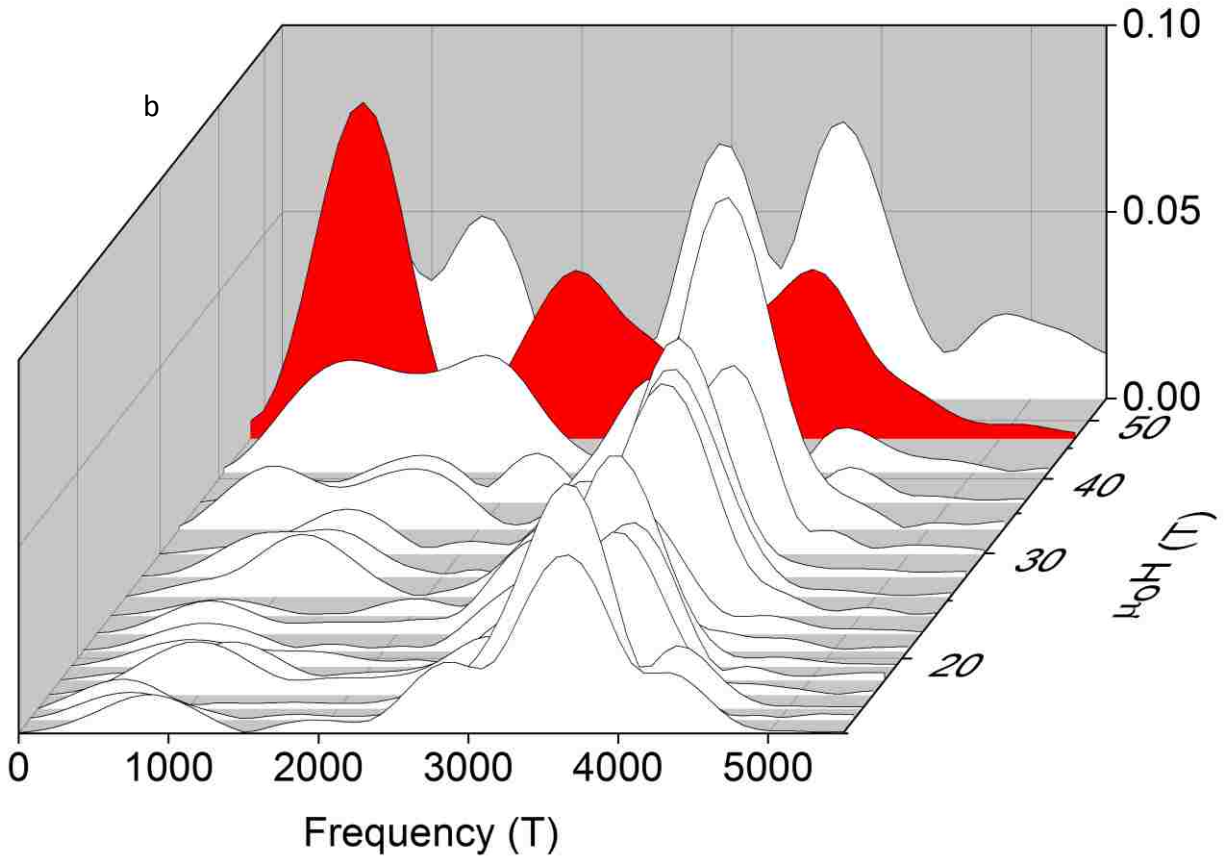


Figure 3.26: AuBe high-field dHvA oscillations with red data highlighting the change in the Fermi surface. (a) Broad frequency range. (b) Zoomed view.

density functional was employed for the calculation with the LAPW cutoff set at R*KMAX=8 and a 23x23x23 grid for Brillouin zone integration. Figure 3.27a,b display the calculated band structure for AuBe with and without spin orbital effects. Multiple crossings at the Fermi level give indication of a complicated Fermi surface. Of particular interest are the band crossings symmetric to the $\Gamma$ point which most likely is the source of the low (or lowest) frequency dHvA oscillations since the small frequencies we measure correspond to a small, mostly spherical Fermi surface. These bands continue till reaching a Dirac point 0.4 eV below the Fermi level as the dispersion is linear for the bands emanating from this point. Figure 3.28a,b,c,d,e displays

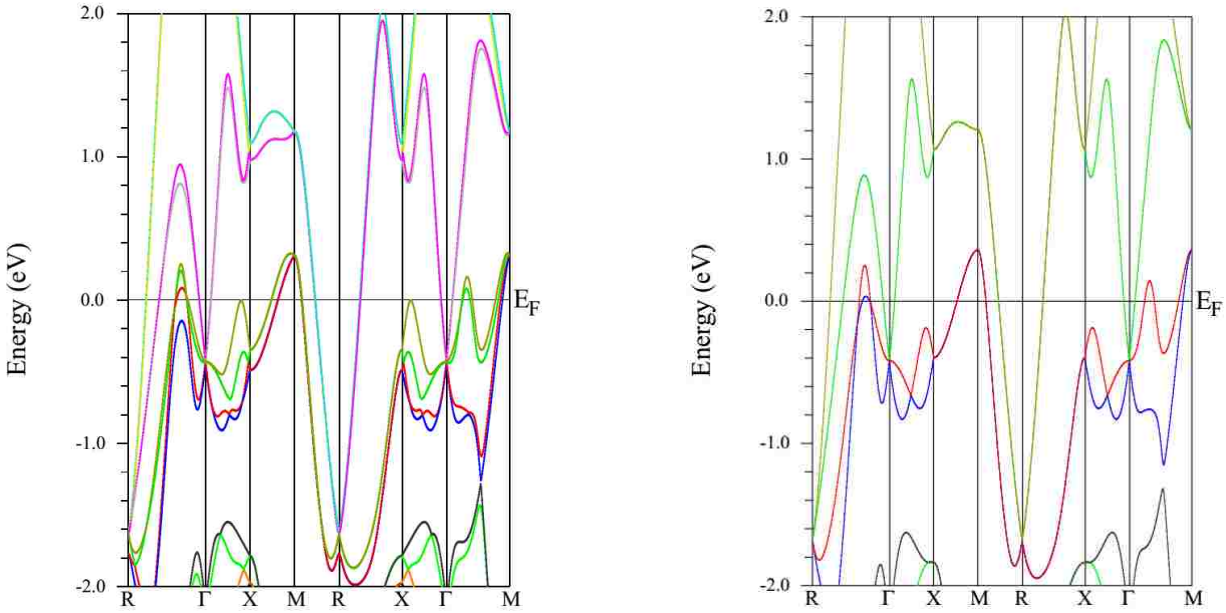


Figure 3.27: AuBe band structure calculation. (a) With spin-orbital effects. (b) Without spin-orbital effects.

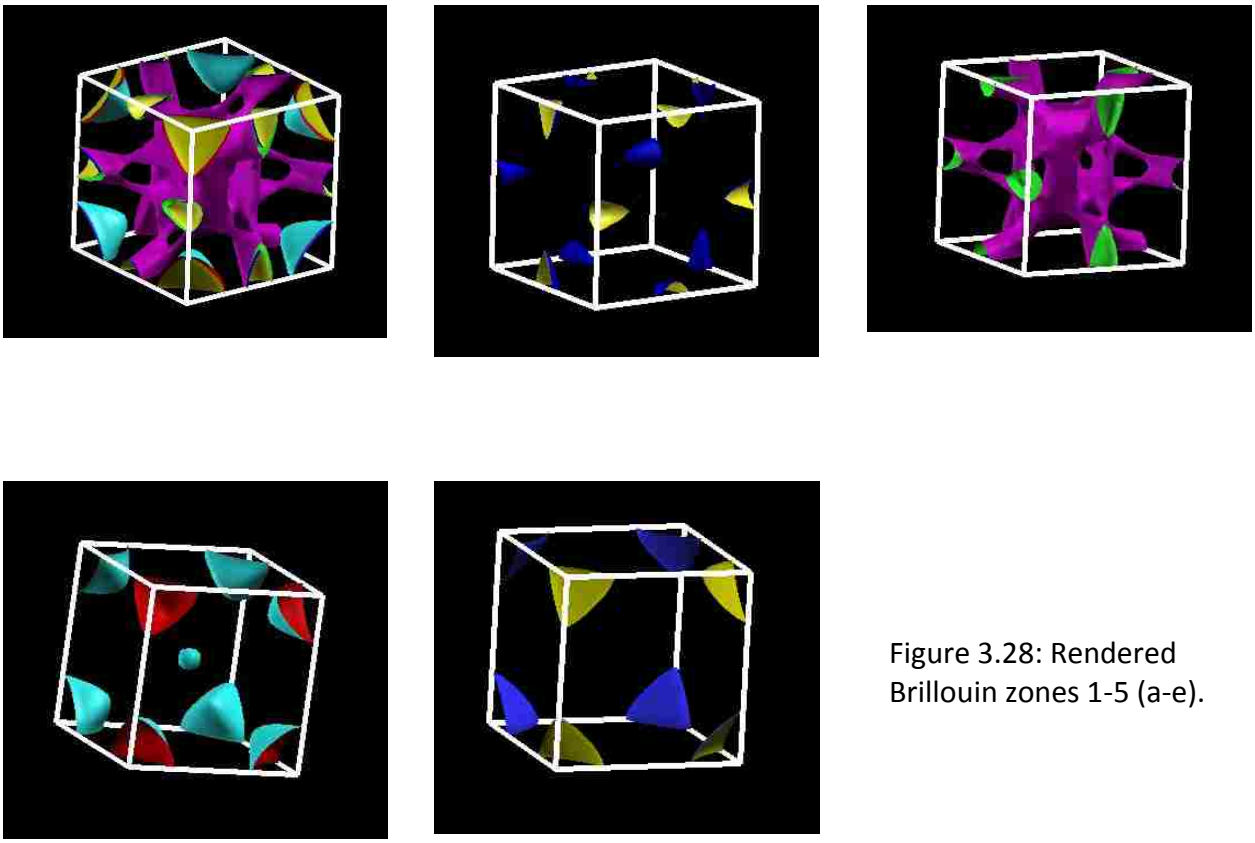

Figure 3.28: Rendered Brillouin zones 1-5 (a-e).

renderings of the Fermi surface from the band structure. As mentioned previously, the low frequency oscillations observed in dHvA analysis most likely originate from the spherical Fermi surface at the $\Gamma$ point which is rendered in Figure 3.28d.

With the data now laid out, the next chapter summarizes what has been learned concerning AuBe, connects this research with related topics in literature, and discusses further questions and future work.

# Chapter 4: Analysis and Conclusions

## 4.1 Introduction

Data presented in the last chapter provided answers to the questions addressed of AuBe in chapter 1 and points toward further avenues of inquiry. This chapter summarizes the key findings from the previous chapter, discusses conclusions and connections with literature, and presents future work necessary for a fuller understanding of the intriguing physics in AuBe. Section 4.2 summarizes the data presented in chapter 3 and presents my conclusions. Section 4.3 discusses the conclusions in context of the background from chapter 1. Section 4.4 discusses the conclusions in context of further literature review. Section 4.5 concludes the chapter with discussion of the question from chapter 1 and proposes further questions and future experiments.

## 4.2 Summary

Superconductivity in AuBe was characterized from a variety of approaches and techniques. Superconductivity in the bulk was established by specific heat and magnetization measurements. The magnitude of the transition in specific heat was characteristic of a weakly-coupled BCS superconductor, and the exponential form of the specific heat in the superconducting state indicated the presence of an isotropic energy gap with *s*-wave spin-singlet pairing at the Fermi level as follows from BCS theory. The energy gap, $\Delta(0)$, was calculated to be 0.486 meV. Magnetization measurement further confirmed the BCS nature of the superconductivity in AuBe by establishment of the superconducting phase diagram which followed closely the parabolic BCS form. The critical values from this fitting came to $T_c = 3.20$ K

and $H_c$ = 247 Oe. Combining these values with effective mass from specific heat and electron density from the Hall effect, the characteristic lengths were calculated to be as follows: correlation length, $\xi_o$ = 86.9 nm, penetration depth, $\lambda_L$ = 110 nm, and G-L parameter, $\kappa$ = 1.27. Linear fitting of the magnetization in the superconducting state indicated approximately a full Meissner effect. The sharp transitions and small hysteresis of the superconducting transition, termed supercooling, gave indication that AuBe is a Type I superconductor near $T_c$. This picture of Type I superconductivity was confirmed in ac susceptibility by observation of the differential paramagnetic effect (DPE), a sharp positive peak in the real component at the superconducting transition. Correspondingly, a single sharp peak in the imaginary component indicated single phase superconductivity with no significant contribution from granular, weak-link, or filamentary superconductivity. The ac susceptibility at low temperature observed a crossover in superconducting behavior at approximately 1.2 K described by the loss of the DPE peak in the real component, broadening of the peak in the imaginary component, and divergence of the phase boundary defined by the onset of superconductivity. This behavior was consistent with the formation of an intermediate vortex state characteristic of Type II superconductors. Fitting the BCS parabolic form to the phase boundary provided a measure of $H_{c2}$ which was used to determine a Ginzburg-Landau parameter, $\kappa$, of 0.867 which is slightly on the Type II side determined by $\kappa > 1/\sqrt{2}$. In a surprise twist, resistivity measurements displayed a superconducting phase boundary which increases dramatically as the sample is cooled into the Type II phase and rising in a nearly linear fashion with decreasing temperature into the Type II section of the phase diagram. The expectation from GL theory is that surface superconductivity should rise till $H_{c3} \approx 1.7 H_{c2}$. Here we observed an apparent $H_{c3}$ that extrapolates to

approximately $4.3 \cdot H_{c2}$ at zero temperature. This result became even more puzzling after the resistivity superconducting transitions maintained their high-field positions after samples were coated with Cr.

Conclusions from these observations are the following. First, AuBe is a weakly-coupled BCS superconductor with a crossover in superconductivity type putting it in a class of superconductors termed Type 1.5. Second, superconductivity with a significantly enhanced critical field is observed by resistivity measurement as the system is cooled into the Type II phase. These conclusions will be elaborated upon in the following sections.

**4.3 Background Context**

The characterization of superconductivity in AuBe was motivated by the possibility of unconventional superconductivity due to the *B20* structure. Unconventional superconductivity from highly correlated electron behavior was not expected. The primary metric available for distinguishing between conventional *s*-wave coupling of superconducting electrons and unconventional superconductivity which has a triplet contribution to the pairing was specific heat measurement since this measurement would capture the nature of the coupling in the temperature dependent form of C(T) below $T_c$. Specific heat measurement in AuBe followed the exponential BCS form as described in chapter 1 indicative of an isotropic fully gapped superconductor. The close proximity of the $\Delta C/C_N$ ratio to the BCS value provided information that the superconductivity was consistent with the BCS weak-coupling limit completing the picture that the pairing mechanism is likely to be the electron-phonon interaction, the electron pairs are almost exclusively in the singlet state, and the symmetry of the pair is predominantly *s*-

wave. Thus these metrics established in chapter 1 for unconventional superconductivity were not met. However, the data from resistivity and magnetic ac susceptibility directed this project in a different direction from the expectations established at the beginning of the project. The robust nature of the superconducting transition in resistivity and the crossover from Type I to Type II superconductivity were unexpected. The next section describes our analysis of these phenomena and attempts to address the conventional or unconventional nature of this superconductivity.

**4.4 New Considerations**

This section presents comparisons to experiments in literature on the systems that display a transition in superconductivity type (I,II) and the robust nature of the resistivity transition. The transition in superconductivity type is a recognized phenomenon and will be addressed first. This is followed by a comparison and analysis of the robust resistivity transition.

In *Introduction to Superconductivity* by Tinkham, superconductors with a GL parameter, $\kappa$, close to $1/\sqrt{2}$ are termed Type 1.5 superconductors. This superconductivity type bears hallmarks of Type I and Type II superconductivity in that the hysteresis of the superconducting transition (supercooling) is missing (as in Type II superconductors) but a first order transition (like Type I) is still observed at the transition [35]. Further consideration must be given of the nature of flux inclusion when materials are in proximity to the crossover point, $\kappa = 1/\sqrt{2}$. The work of Jacobs, et. al discusses the nature of vortices in superconductors as a function of $\kappa$. Their work showed that two vortices in a Type I superconductor would attract each other while two vortices in a Type II superconductor would repel. Additionally, they found that at the crossover point

from Type I to Type II the energy of the two-vortex configuration was constant in terms of distance and thus noninteracting [35]. One of the early experiments on a Type 1.5 superconductor was performed by Krägeloh who doped Pb, a Type I superconductor, with Tl pushing the value for κ past the crossover point of $1/\sqrt{2}$. A nearly precise value $1/\sqrt{2}$ was found for a doping level of 1.8 wt% Tl, and a decoration technique followed by optical and electron microscopy was used to image magnetic flux at the surface. Observation of the surface revealed a mixed state defined as some regions of the sample showing a Meissner effect and other regions hosting magnetic flux tubes. Square and triangular arrangements of flux tubes were observed as they formed a lattice around regions supporting the Meissner effect. The implication from the images was that an attractive long range interaction existed in addition to a repulsive short range interaction [36]. Further research by Auer, et. al provided more experimental details of Type 1.5 superconductors. Their work involved the Type I superconductor, Ta, with nitrogen interstitials incorporated by annealing a Ta wire in a nitrogen atmosphere. Figure 4.1 displays isothermal magnetization sweeps (plotted as –M) for the nitrogen interstitial concentration yielding a κ just under $1/\sqrt{2}$. The highest temperature sweeps show the distinct sharp transitions for Type I superconductivity while the low temperature sweeps show transitions that begin to broaden at the base [37]. Thus, the

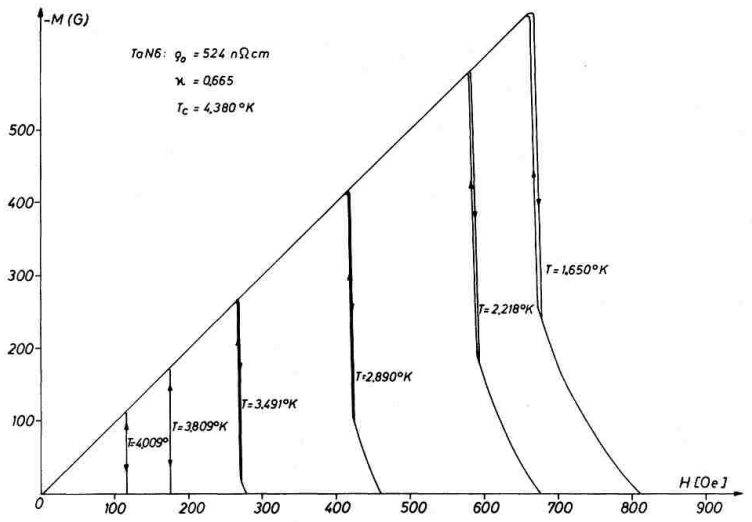


Figure 4.1: Isothermal magnetization curves for N-doped Ta [37].

consistent picture of Type 1.5 superconductors is one of mixed characteristics between Type I and Type II superconductors in addition to competing interactions controlling the formation of magnetic flux structures.

More recent work on $MgB_2$ has opened a new category of Type 1.5 superconductivity. While the previously discussed experiments on Type 1.5 superconductivity involved doped Type I superconductors possessing a single GL parameter, $MgB_2$ was found to host two GL parameters associated with phonon coupling for $\sigma$ and $\pi$ bonds. The GL parameter for the $\sigma$-band was determined to be $\kappa = 3.68$ (Type II) while the GL parameter for the $\pi$-band was determined to be $\kappa = 0.66$ (Type I). Moshchalkov, et. al performed a decoration technique to observe the formation of magnetic flux structures on the surface of $MgB_2$. They found evidence of competing long range attractive and short range repulsive interactions of the magnetic vortices formed on the surface as evidenced by inhomogeneous spacing of vortices and the appearance of grouped vortex stripes [38].

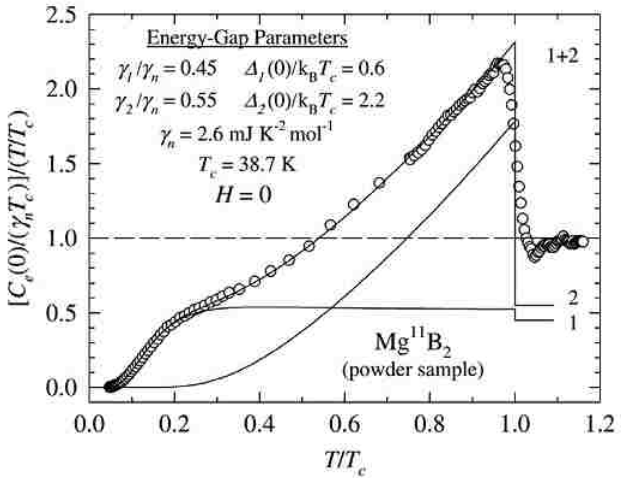

Figure 4.2: Specific heat data and two gap model fit for $MgB_2$ [39].

The question of which category best fits AuBe is clearly answered by examination of the specific heat of $MgB_2$. Figure 4.2 displays a plot of specific heat for $MgB_2$ which includes modeling of the two band gaps [39]. No such anomalies were observed in the specific heat of the superconducting state in AuBe. Thus AuBe falls into the category of single gap (single GL

parameter) Type 1.5 superconductivity with the rare condition that no additional doping or addition of interstitials was needed for the tuning of κ.

A search was made of NCS to see if any other superconductors in this symmetry class hosted Type 1.5 superconductivity. A study by Motoyama, et. al on $LaPt_3Si$ revealed strikingly similar behavior of a superconductivity crossover from Type I to Type II at approximately 0.40 K. Figure 4.3 displays their data for ac susceptibility characterization of the superconducting transition in their polycrystalline sample. In the real component (χ'), a differential paramagnetic effect peak (DPE) is observed at the superconducting transition until the crossover point at approximately 0.40 K where the transition begins to broaden. Correspondingly, the imaginary component (χ") shows a broadening of the superconducting transition peak past the crossover point. The loss of the DPE peak and the broadening of the superconducting transition in the real and imaginary components indicate a crossover from a regime characteristic of the Meissner effect (Type I) to a regime characteristic of the mixed normal/superconducting state (Type II). $LaPt_3Si$ (a weakly-correlated NCS) has attracted interest due to its structure being the same as the aforementioned $CePt_3Si$ (a highly-correlated NCS) [40]. Unfortunately, no superconducting

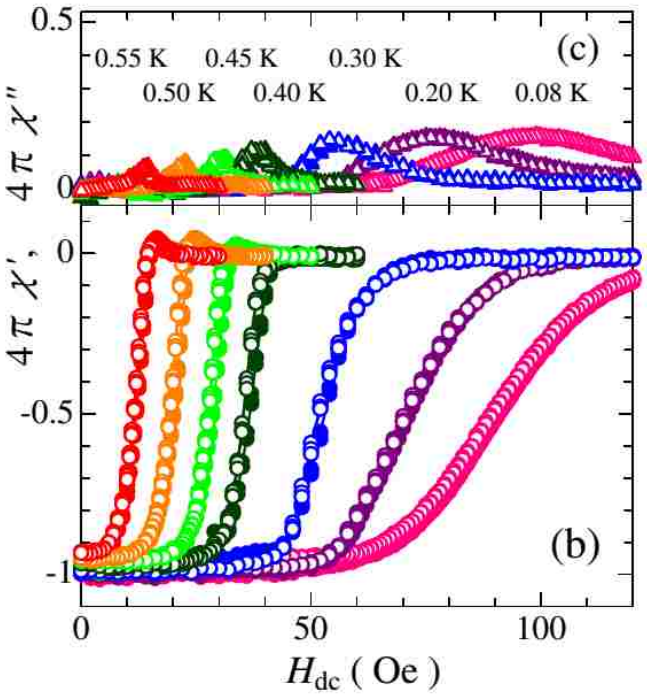


Figure 4.3: Isothermal magnetic ac susceptibility for polycrystalline $LaPt_3Si$. χ' = real component. χ" = imaginary component [40].

phase diagram can be found that includes a phase boundary described by resistivity so no further connection to this particular material can be made at this time.

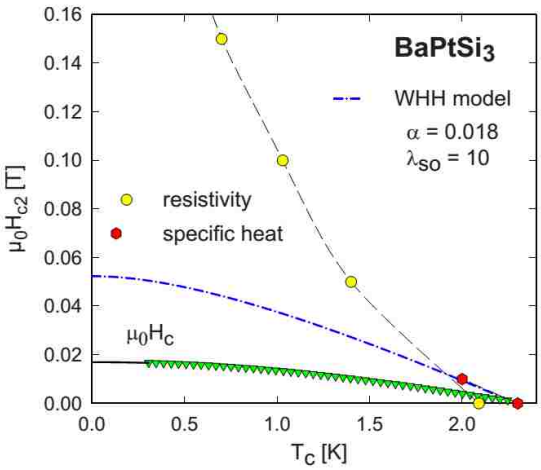


Figure 4.4: Superconducting phase diagram for $BaPtSi_3$ [12].

Consideration is next given to the robust nature of the superconducting transition and its temperature dependence as observed by resistivity. The previously mentioned $LaPt_3Si$ would be an excellent candidate for further characterization of the superconducting boundary in resistivity. A literature search was conducted to see if other NCS might be candidates for comparison. The study on $BaPtSi_3$ described in chapter 1 included data on the superconducting phase boundary established from resistivity. Figure 4.4 displays the superconducting phase diagram from resistivity and specific heat. The phase boundary from resistivity is observed to significantly diverge from the phase boundaries established by specific heat and thermodynamic critical field. The authors attributed this divergence to simply a surface effect [12]. Kimura, et. al published a study on $LaRhSi_3$, a compound isostructural to $BaPtSi_3$ (*I4mm*), where again the superconducting phase boundary in resistivity was observed to rise far above what is expected from the de Gennes estimate for a surface sheath of superconductivity. Figure 4.5a displays the superconducting phase diagram for $LaRhSi_3$ which includes data points from resistivity and magnetization characterizations. The deviation as reported in the paper occurs around 1.9 K.

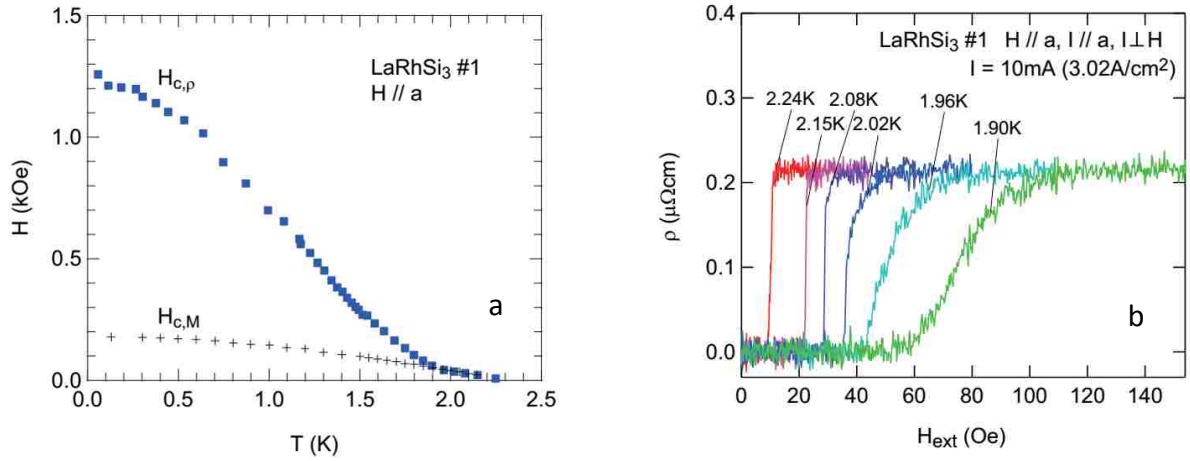


Figure 4.5: (a) Superconducting phase diagram for $LaRhSi_3$. (b) Superconducting transitions measured by resistivity [41].

Figure 4.5b displays the resistivity transitions used to generate the phase boundary above 1.9 K. The authors note that the resistivity transitions broaden as temperature is lowered past 1.9 K and suggest a change in superconductivity [41]. Comparison with the similar effect in AuBe suggests a crossover in superconductivity type near the divergence in the phase diagram. Unfortunately, no magnetic ac susceptibility measurements have been published preventing further comparison.

A study on BiPd by Sun, et. al noted a robust superconducting transition in resistivity when compared with the transition in specific heat. Figure 4.6 displays specific heat with fit to the BCS exponential form and resistivity data at 1.4 K. As can be seen between the two plots, an order magnitude in field separates the two transitions. A microscopic probe of the superconducting state by scanning tunneling microscopy confirmed both the isotropic fully gapped nature of the superconductivity and critical field ($H_{c2}$) as observed by the specific heat measurement. Thus, the superconducting transition in resistivity was confirmed as not reflecting the bulk superconducting state but rather an enhanced superconductivity associated with defects such as

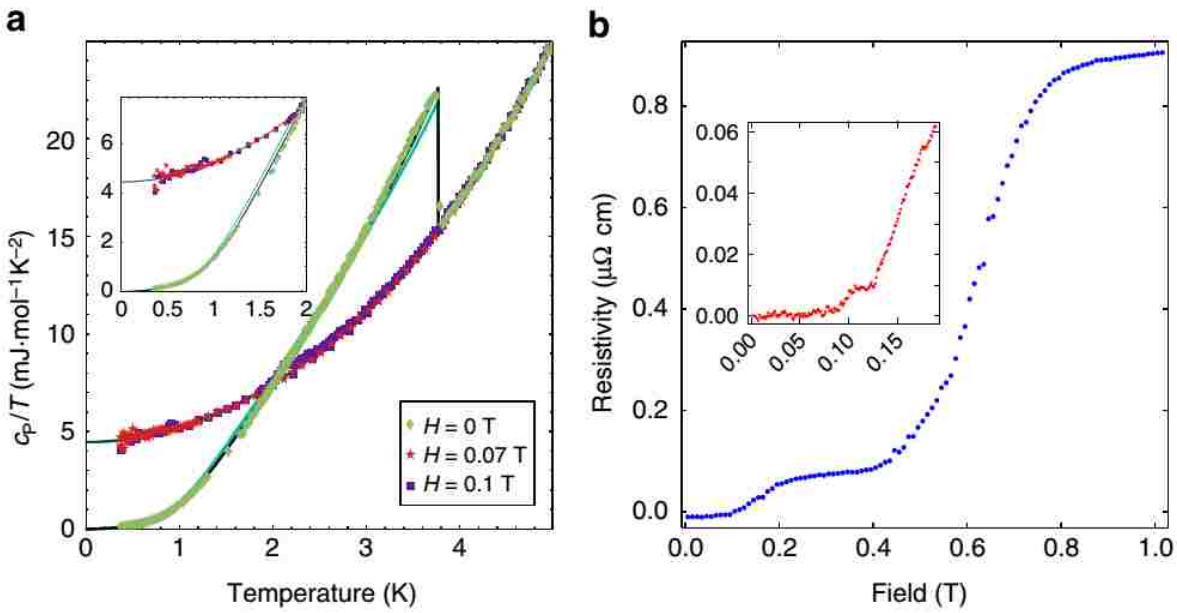


Figure 4.6: (a) Specific heat measurement of the superconducting state in BiPd. (b) Resistivity measurement of the superconducting state at 1.4 K [42].

twin boundaries [42]. A paper from Aoyama, et. al was cited in this conclusion which argues for an enhanced upper critical field ($H_{c2}$) in *s*-wave Type II NCS with the following qualification. The enhancement is predicted to occur at twin boundaries which border crystalline domains with different antisymmetric spin orbit couplings. The authors suggested an experimental technique such as ac susceptibility which would be more sensitive to superconductivity occurring in minute volumes [43].

Comparison to AuBe is made with the work of Sun, et. al [42] and Aoyama, et. al [43]. First, while both BiPd and AuBe exhibit the robust superconducting transition as measured in field from resistivity, the factor difference in the BiPd data far outweighs the difference in AuBe (10x vs. 4x). Second, distinct structure is observed in the resistivity transition for BiPd that is not observed in the transition for AuBe. Third, BiPd does not possess an unconventional surface state which appears to also be the case for AuBe since a Cr film deposited on all sample surfaces did

not serve to diminish the resistivity transition in field. Fourth, antisymmetric spin orbit coupling was determined to play a significant role in BiPd by the formation of a Dirac surface state (no modification to superconductivity) while in AuBe, spin orbit coupling was determined to have less effect from band structure calculation and little or no effect on superconductivity. From these comparisons, the following conclusions can be deduced. First, AuBe like BiPd most likely does not possess unconventional superconductivity on the surface. Second, the possibility exists that the superconducting state seen in the resistivity of AuBe is due to twinning boundaries which must have interesting effects due to the change in chirality inherent to these boundaries.

**4.5 Future Work**

The question posed in chapter 1 concerned the investigation of novel superconductivity in AuBe. While no definitive signatures of unconventional superconductivity were found such as an anisotropic gap, line nodes, unusual pairing mechanism, etc., the enhanced superconducting transition in resistivity represents novel superconductivity by an undetermined mechanism. Comparison with other NCS such as $LaPt_3Si$ and $LaRhSi_3$ show that the field-enhanced resistive transition and crossover in superconductivity are not unique to AuBe but still lack sufficient explanation. These conclusions lead to the following questions.

First, what mechanism is responsible for pushing the resistivity superconducting transition significantly higher than the magnetization transition (and the largest possible $H_{c3}$)? Second, is there a connection between the enhanced $H_{c2}$ and the existence of the crossover from Type I to Type II superconductivity? Third, what is the consequence of a chiral crystal structure

hosting competing long range attractive interaction and short range repulsive interaction of vortices at the crossover point in single-gap Type 1.5 superconductivity?

From these questions, the following future work is suggested in addition to suggested future work from other chapters. First, XPS was suggested from chapter 2 as a means to quantify the stoichiometry of the surface. Second, a follow-up measurement is proposed where AuBe is coated with Cr for magnetic ac susceptibility measurement. Third, a surface microprobe such as scanning tunneling spectroscopy is needed to search for unconventional superconductivity on the surface of AuBe in addition to a direct characterization of the superconducting energy gap. This unconventional superconducting state would have to be robust against the deposition of a Cr film. Fourth, connection between the robust superconducting transition and the crossover in superconductivity type could best be observed in a surface imaging technique such as magnetic force microscopy, surface magneto-optic Kerr effect, Bitter decoration, scanning SQUID microscopy, scanning Hall probe microscopy, etc. This type of characterization would also provide the chance to observe the effect of a chiral structure on dynamics of vortices in a single-gap Type 1.5 superconductor. Fifth, neutron diffraction would provide a measurement of the flux-line symmetry. Sixth, a search for the spin-triplet state in AuBe could be performed with μSR spectroscopy. Seventh, further characterization of the AuBe Fermi surface by de Haas-van Alphen measurement is proposed as follow-up to the exploratory effort presented in chapter 3. The search for novel superconductivity in AuBe discussed in chapter 1 led us to find unexpected phenomena and provided motivation for continued research on this unique *B20* FeSi-type superconductor.

Note from the author: Since the writing of this dissertation but before publication, another superconducting *B20* compound, RhGe, was found to be recently reported. This second *B20* superconductor with a $T_c$ of approximately 4.5 K [44] comes over a half century after the discovery of the first *B20* superconductor, AuBe, in 1959 [16].

Second note from the author: Since the writing of this dissertation but before publication, it has come to the author's attention that reports on three compounds exist in literature that describe a *B20* superconductor. From 1982, Chevalier, et al. reported on LaRhSi with a $T_c$ of 4.35 K and LaIrSi with a $T_c$ of 2.3 K. Only zero field resistance across the superconducting transition was characterized so further analysis is needed to confirm superconductivity in the bulk [45]. From 2011, Takeya, et al. reported on superconductivity in $Li_xRhB_y$ ($0.6 < x < 2$, $1 < y < 2$) but expressed uncertainty whether the structure was better characterized by the $P2_13$ (*B20*) or $P4_232$ space groups. The superconductivity was characterized by specific heat and magnetization measurements but not resistivity measurement [46]. Thus further refinement of the structure and resistivity measurements would be necessary for comparison with AuBe.

## Bibliography


[1] H. Onnes, *Leiden Comm.,* 120b, 122b, 124c, 1911. [cited from [2]]

[2] M. Tinkham, *Introduction to Superconductivity, 2nd ed*., New York: Dover Publications, 2004.

[3] F. London and H. London, *Proc. Roy. Soc. (London),* A149, 71, 1935. [cited from [2]]

[4] C. Gorter and H. Casimir, [*Phys. Z*. 35, 963. 1934] *Physica,* 1, 306, 1934. [cited from [2]]

[5] J. Bardeen, L. Cooper and J. Schrieffer, *Phys. Rev.,* vol. 108, no. 5, 1957.

[6] D. Goodstein, *States of Matter*, Mineola, New York: Dover Publications, 1985.

[7] A. Abrikosov, *Zh. Eksperim. I Teor. Fiz.,* 32, 1442, 1957. [cited from [2]]

[8] D. Saint-James and P. de Gennes, *Phys. Lett.,* 7, 306, 1963. [cited from [2]]

[9] V. Mineev and K. Samokhin, *Introduction to Unconventional Superconductivity*, The Netherlands: Gordon and Breach Science Publishers, 1999.

[10] E. Bauer and M. Sigrist, eds., *Non-centrosymmetric Superconductors*, New York: Springer, 2012.

[11] E. Bauer, H. Kaldarar, A. Prokofiev, E. Royanian, A. Amato, J. Sereni, W. Brämer-Escamilla and I. Bonalde, *J. Phys. Soc. Jpn.,* vol. 76, no. 5, 2007.

[12] E. Bauer, R. Khan, H. Michor, E. Royanian, A. Grytsiv, N. Melnychenko-Koblyuk, P. Rogl, D. Reith, R. Podloucky, E. Scheidt, W. Wolf and M. Marsman, *PRB,* 80, 2009.

[13] H. Takeya, K. Hirata, K. Yamaura, K. Togano, M. El Massalami, R. Rapp, F. Chaves and B. Ouladdiaf, *PRB,* 72, 2005.

[14] H. Yuan, D. Agterberg, N. Hayashi, P. Badica, D. Vandervelde, K. Togano, M. Sigrist and M. Salamon, *PRL,* 97, 2006.

[15] B. Cullity, *Transactions of the American Institute of Mining and Metallurgical Engineers,* 171, 1947.

[16] B. Matthias, *Journal of Physics and Chemistry of Solids,* vol. 10, 4, 1959.

[17] C. Poole, *Handbook of Superconductivity*, New York: Academic Press, 2000.

[18] A. Tonomura, Y. Xiuzhen, K. Yanagisawa, T. Matsuda, Y. Onose, N. Kanazawa, H. Park and Y. Tokura, *Nano Lett.,* 12, 2012.

[19] X. Yu, Y. Onose, N. Kanazawa, J. Park, J. Han, Y. Matsui, N. Nagaosa and Y. Tokura, *Nat. Lett.,* vol. 465, 2010.

[20] X. Yu, N. Kanazawa, Y. Onose, K. Kimoto, W. Zhang, S. Ishiwata, Y. Matsui and Y. Tokura, *Nat. Mat.,* vol. 10, 2011.

[21] N. Kanazawa, J. Kim, D. Inosov, J. White, N. Egetenmeyer, J. Gavilano, S. Ishiwata, Y. Onose, T. Arima, B. Keimer and Y. Tokura, *PRB,* 86, 2012.

[22] S. Seki, X. Yu, S. Ishiwata and Y. Tokura, *Science,* vol. 336, 2012.

[23] W. Mitchell, J. Mullendore and S. Maloof, *Transactions of the Metallurgical Society of AIME,* vol. 221, August 1961.

[24] A. Martin and A. Moore, *Journal of the Less-Common Metals,* vol. 1, 1959.

[25] DR. EBERL MBE-KOMPONENTEN GMBH, [Online]. Available: http://www.mbe-komponenten.de/selection-guide/crucible.php. [Accessed 18 August 2015].

[26] Quantum Design, Magnetic Property Measurement System*, Reciprocating Sample Option User's Manual*, Part Number 1090-100C; *AC Option User's Manual*, Part Number 1017-110A; *MPMS MultiVu Application User's Manual*, Part Number 1014-110C.

[27] J. Clarke and A. Braginski, eds., *The SQUID Handbook*, Weinheim: WILEY-VCH Verlag GmbH & Co., 2004.

[28] Quantum Design, *Physical Property Measurement System, Heat Capacity Option User's Manual*, Part Number 1085-150, J1.

[29] National High Magnetic Field Laboratory, [Online]. Available: https://nationalmaglab.org/user-facilities/pulse-field-facility/instruments-pff/65-tesla-multi-shot-magnet. [Accessed 26 August 2015].

[30] W. Kraus and G. Nolze, Federal Institute for Materials Research and Testing, [Online]. Available: http://www.ccp14.ac.uk/ccp/web-mirrors/powdcell/a_v/v_1/powder/e_cell.html.

[31] P. Villars and L. Calvert, *Pearson's Handbook of Crystallographic Data for Intermetallic Phases, 2nd ed*., ASM International, 1991.

[32] R. Hein, T. Francavilla and D. Liebenberg, eds., *Magnetic Susceptibility of Superconductors and Other Spin Systems*, New York: Plenum Press, 1991.

[33] B. Mühlschlegel, *Zeitschrift Für Physik,* 155, 1959.

[34] D. Shoenberg, *Magnetic Oscillations in Metals*, Cambridge: Cambridge University Press, 1984.

[35] L. Jacobs and C. Rebbi, *PRB,* vol. 19, no. 9, 1979.

[36] U. Krägeloh, *Physics Letters,* 28A, no. 9, 1969.

[37] J. Auer and H. Ullmaier, *PRB,* vol. 7, no. 1, 1973.

[38] V. Moshchalkov, M. Mariela, T. Nishio, Q. Chen, A. Silhanek, V. Dao, L. Chibotaru, N. Zhigadlo and J. Karpinski, *PRL,* 102, 2009.

[39] S. Bud'ko and P. Canfield, *Physica C,* 514, 2015.

[40] G. Motoyama, M. Shiotsuki, Y. Oda, A. Yamaguchi, A. Sumiyama, T. Takeuchi, R. Settai and Y. Onuki, *J. Phys. Soc. Jpn.,* 81, 2012.

[41] N. Kimura, H. Ogi, K. Satoh, G. Ohsaki, K. Saitoh, H. Iida and H. Aoki, *JPS Conf. Proc.,* 3, 2014.

[42] Z. Sun, M. Enayat, A. Maldonado, C. Lithgow, E. Yelland, D. Peets, A. Yaresko, A. Schnyder and P. Wahl, *Nat. Comm.,* 30, 2015.

[43] K. Aoyama, L. Savary and M. Sigrist, *PRB,* 89, 2014.

[44] A. Tsvyashchenko, V. Sidorov, A. Petrova, L. Fomicheva, I. Zibrov and V. Dmitrienko, *arXiv:1509.08249v1. cond-mat.supr-con,* 28 Sep 2015.

[45] B. Chevalier, P. Lejay, A. Cole, M. Vlasse and J. Etourneau, *Solid State Communications,* 41, 11, 1982.

[46] H. Takeya, H. Fujii, M. El Massalami, F. Chaves, S. Ooi, T. Mochiku, Y. Takano, K. Hirata and K. Togano, *arXiv:1102.0623,* 3 February 2011.

# Appendix

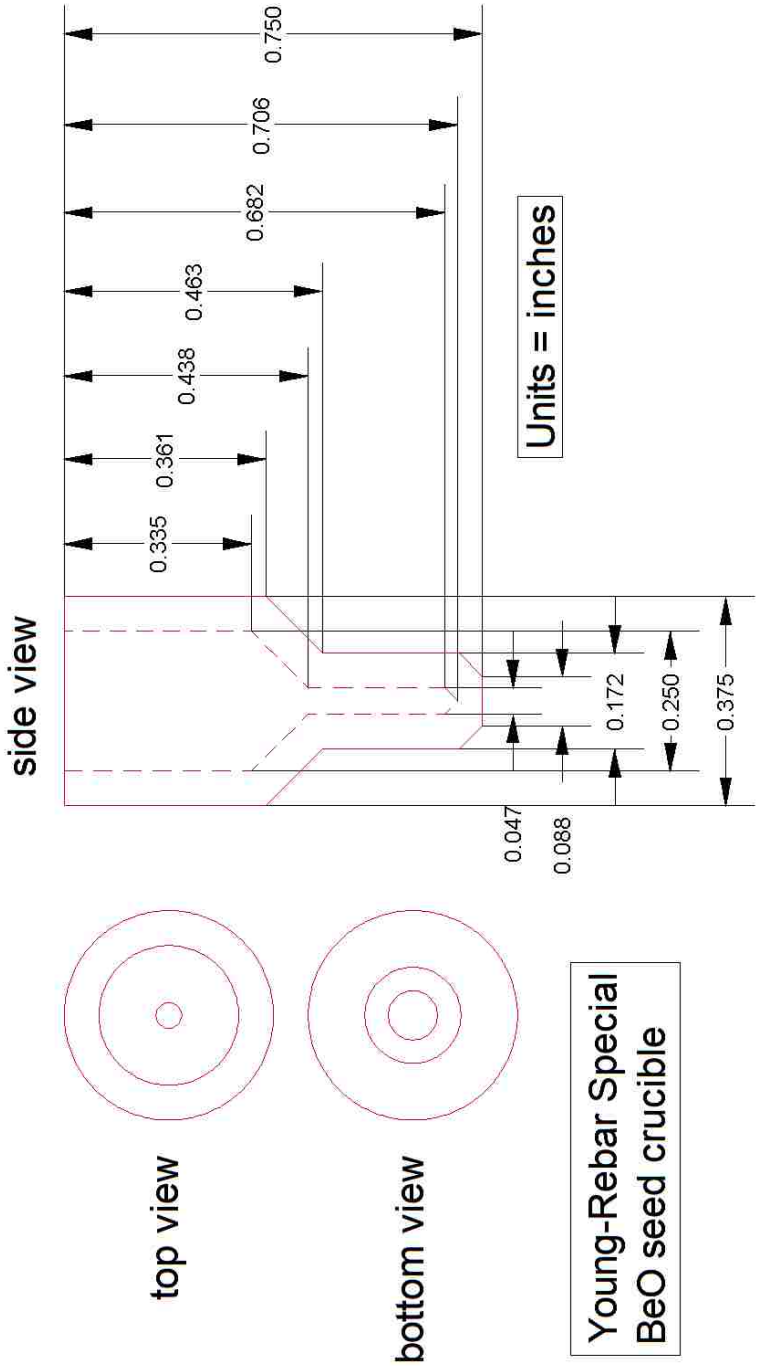
side view
0.335
0.361
0.438
0.463
0.682
0.706
0.750
Units = inches
0.047
0.088
0.172
0.250
0.375
top view
bottom view
Young-Rebar Special
BeO seed crucible

# Vita

Drew Rebar was born in South Carolina to Denver and Deloris Rebar and has also lived in Georgia and Florida. He graduated from Providence Christian School, Riverview, FL in 2000 pursuing higher education at Bob Jones University, Greenville, SC (B.S., Physics, 2004), the University of South Florida, Tampa, FL (M.S., Physics, 2006), and Louisiana State University and Agricultural and Mechanical College, Baton Rouge, LA (Ph.D., Physics, 2015). After graduation at the end of 2015, he plans to continue experimental condensed matter research elsewhere. Drew is the first Ph.D. in his family and in addition to physics enjoys playing his mountain dulcimer, reading/listening to books, attending fine arts performances, fishing, bicycling, and exploring gardens, parks, museums, cities, etc.